UNIVERSITÀ DEGLI STUDI DI NAPOLI
"FEDERICO II"

FACOLTÀ DI INGEGNERIA

Dottorato di Ricerca in "Ingegneria Aerospaziale, Navale e
della Qualità" – XVII Ciclo

Indirizzo: Fluidodinamica Microgravitazionale

Settore Scientifico-Disciplinare ING-IND/05:

Impianti e Sistemi Aerospaziali

Analysis of the Dynamical Environment characterising the USV FTB_1 Vehicle performing the first DTFT Mission

Ing. Michelangelo Russo

Tutor:

Ch.mo Prof. Antonio Moccia

Coordinatore:

Ch.mo Prof. Antonio Moccia

Abstract

The successfully realisation of a microgravity experiment, whatever its objective could be, necessarily requires a dynamical characterisation of the environment in which it takes place as complete and precise as possible. This is due to the strong influence of the levels of acceleration reached on the results of the experiment; without a detailed set of information about the former, it will not be possible a correct interpretation of the latter.

This thesis concerns the analysis of the gravity level that is possible to realise during the first mission of the Unmanned Space Vehicle (USV) developed by the Italian Aerospace Research Centre (CIRA), in the framework of the Italian National Aerospace Research Program (PRORA).

The Flying Test Bed 1 (FTB_1) is a slender, not-propelled winged vehicle, able to perform experiments in areas such as Structure and Aeroelasticity, Autonomous Guidance Navigation and Control and Thermo-Aerodynamics.

The purpose of this thesis is to verify if it could be possible to consider the FTB_1 as exploitable also for microgravity experimentation.

KEYWORDS: Microgravity, Acceleration Level, Unmanned Vehicle

Acknowledgements

There are several persons that have been important for the completion of the this thesis, and that I would like to thank.

First of all, my sincere gratitude goes to all the members of the department of Space Science and Engineering "L. G. Napolitano"; they all have encouraged and followed me during the difficulties encountered. In particular, I really have to thank Professor Antonio Moccia, to have believed in my possibility to complete this Ph.D. course also when I did not.

In the years from the beginning to the end of this experience, I have been so lucky to encounter also other people that have walked with me part of the way: from the colleagues involved in the CIRA USV program, to the guys of the GAFACS course, I owe something to all of them, for all the discussions, advices and suggestions received.

Finally I deeply have to say thank you to my family: to my parents, Francesco and Anna, because without them nothing of this would be there today.

Table of Contents

Chapter II

Chapter III

Nomenclature

CIRA	Italian Aerospace Research Centre
PRORA	Italian National Aerospace Research Program
USV	Unmanned Space Vehicle
FTB	Flying Test Bed
g	Gravity Acceleration
M	Mach Number
Re	Reynolds Number
α	Angle of incidence
β	Angle of sideslip
C_L	Lift Coefficient
C_D	Drag Coefficient
C_Y	Side Force Coefficient
C_l	Rolling Moment Coefficient
C_m	Pitching Moment Coefficient
C_n	Yawing Moment Coefficient
L, D, Y	Lift, Drag and Side Force, respectively
l, m, n	Rolling, pitching and yawing moment, respectively
p, q, r	Roll, pitch and yaw angular velocity, respectively
V	Vehicle velocity, measured with respect to an inertial reference frame
u, v, w	Component of the vehicle velocity along its x-body axis, x-body axis and z-body axis respectively
δ_*	Deflection angle for a generic command surface: (right/left elevon, rudder)
S	Wing surface
b	Wing span
c	Mean aerodynamic chord
ϕ, θ, ψ	Roll, Pitch and Yaw angle, respectively

m		Vehicle mass
ρ		Air density,
μ		Air dynamical viscosity
a		Speed of Sound
q_∞		Dynamic Pressure
ESA		European Space Agency
HOT		Higher Order Term
RCS		Reaction Control System
PWM		Pulse Width Modulation

Introduction

The objective of the study reported in this thesis is the analysis of the first mission that will be performed by the USV FTB_1 vehicle, from a dynamical point of view, i.e. considering the level of accelerations that can be reached during its development. This is done in order to ascertain if a mission of this kind could be considered satisfactory for microgravity applications.

In the first Chapter, a brief overview of the main research areas that benefit from the availability of a low-gravity environment, and of the ones that allow its realisation, is given. Immediately after, it follows a description of the facilities commonly used for this purpose, then a summary of the characteristics of the USV program is provided, focusing on its principal experimental objectives.

Chapter 2 is an extended analysis of the characteristics of the FTB_1 vehicle. This results as necessary in order to completely describe the experimentation environment eventually available.

The Chapter is divided in two part. The first one, consists of a flyiability analysis, i.e. a complete characterisation of the vehicle in terms

of trimmability and stability properties. This analysis is executed also in presence of aerodynamic uncertainties, by means of a properly developed procedure.

The second part of the Chapter extents the analysis in presence of uncertainties, using a classical Monte Carlo approach.

The third and last Chapter focuses the study on the acceleration levels that are proper of the mission. The evaluation is conducted considering both the nominal trajectory and the trajectories resulting from the Monte Carlo analysis of the previous Chapter. Several different strategies useful to enhance the performances of the system are then proposed. Finally, an example of the possible future missions planned in the USV program is examined, in order to provide a more in-depth view of the capabilities of the system.

Chapter I

Microgravity in Aerospace Environment, and its Utilisation

I.1 Introduction

The term *microgravity* began to be used together with the exploitation of the space environment, and for it the literal meaning of "gravity field one million of times smaller than the terrestrial one" was then intended. Today, after a more detailed investigation of the physical conditions that can be realised on space platforms and laboratories, it can be used to generally identify a particular condition in which a system is subject to a gravitational field of limited intensity, always with respect to the terrestrial one.

In these conditions it is possible to investigate and understand various physical, chemical and biological processes which are commonly masked by gravity. For example, phenomena such as convection, sedimentation and hydrostatic pressure are absent under microgravity and interestingly different behaviour in solids, liquids, gases and their interfaces can be observed.

The aim of the following paragraphs is to give a short survey of the more relevant research areas of today, and, subsequently, of the platforms and facilities that consent to realise microgravity conditions.

I.2 Research in Microgravity: Main Topics

The contemporary microgravity research involves mainly the following areas:

- ► Fluid Physics and Combustion;
- ► Materials Science;
- ► Biology and Biotechnology;
- ► Automatic Controls.

Moreover, a considerable effort is devoted to the precise characterisation of the microgravitational environment, and on the influence of residual gravitational disturbances on the conducted experiments.

I.2.a   Fluid Physics and Combustion

The study of thermophysical fluid properties, from both an experimental and theoretical point of view, is currently an important research sector in modern physics.

Microgravity research in fluid physics is focused on a comprehensive study of fluid dynamics and transport phenomenon, where fundamental

behaviour is limited or affected by gravity[1],[2]. These include study of two phase flows, diffusion of liquids and gases, surface tension-induced convection, capillary flow, critical point wetting and how particles and gas bubbles suspended in a fluid interact with and change the properties of the fluid. The universal nature of these phenomena make their study fundamental to other areas of microgravity research by providing new tools for ground-based research in science and engineering.

The research in combustion is centred on improving the understanding of the process of ignition, propagation, spreading and extinction of flames, using microgravity conditions in space. The research includes the study of droplet combustion, transient processes in gaseous flames, combustion-turbulent interactions, soot processes, spray and aerosol combustion[1],[3].

Another interesting field of research, that lies on the edge between combustion and materials science, is the combustion synthesis, in which highly exothermic waves of chemical interaction self-propagate through the reaction medium, yielding final products (powders, materials, alloys) among which there are various that can find direct aerospace application[3],[4].

I.2.b   *Materials Science*

The materials science research is aiming at identifying and understanding the cause and effect relationship between the processing, properties and structure of materials under microgravity environment. The investigations include study of directional solidification, semiconductor and zeolite crystal growth, diffusion in liquid metals, container-less processing of corrosive materials, formation of metal foams, special alloys, composites, special glasses, ceramics and polymers[1].

Zeolites, for example, make up a group of microporous compounds which play an important role in several technological fields, mainly catalysis, ion exchange and molecular sieving. As a consequence, there is a great interest in studying the synthesis process, whose understanding could yield a number of advantages as: (a) optimisation of industrial production of zeolites; (b) development of new production techniques; (c) production of new zeolites, tailored for specific applications[5],[6].

Melting and solidification of materials have been subject of experiments flown on the Space Shuttle[7] and on the International Space Station[2].

I.2.c   Biology and Biotechnology

The biology and biotechnology research is focusing on understanding the fundamental processes controlling protein crystal growth and cell/tissue culture. Research in this area involves growth of large protein crystals under microgravity to study its structure, understanding mammalian and plant cell division and growth, electrophoretic separation and purification of cells, encapsulation of antitumour drugs[1].

Cell biology, for example, can benefit of the possibility to realise cultures in three-dimensional arrays, that is not possible in ground-based experiments[2]. When it is possible to dispose of microgravity conditions for a significant period, then experiments of bioastronautics, in which the effect of the long-duration space flight on the human physiology can be investigated, or of fundamental biology, in which the focus of the experimental activity is on plant and animal models[2] also become realisable.

Important lifesaving drugs and pharmaceuticals could be produced in space. These include beta cells (for diabetes), pituitary cells (for dwarfism), urokinase (for blood clots), interferon (for certain cancers) and protease inhibitors (for AIDS)[1],[2].

I.2.d   Automatic Controls

The researches in automatic controls involves mainly two areas.

The first one concerns the field of Unmanned Aerial Vehicles (UAVs), in which this thesis itself can be partially catalogued. The realisation of flight control systems for unmanned facilities that can perform specific kind of missions (like parabolic flights, that will be further introduced in the following paragraph) will significantly reduce the costs of this kind of experimentation, while enhancing its reliability, and potentially obtaining better performance levels with respect to piloted aircrafts[8],[9],[10],[11],[12]. By the way, in the context of UAV related activities, the University of Naples itself has started in recent years a related program[13],[14].

Another topic of interest regards the isolation systems that prevent the propagation of vibration from the vehicle, or, in general, the facility, to the microgravity experiment. Modern control theories have been applied to the analysis and synthesis of active isolation systems, resulting highly effective[15],[16],[17].

I.2.e   *Characterisation of the Microgravity Environment*

The precise and complete characterisation of the gravitational environment in which a microgravity experiment is taking place is of paramount importance for the right execution of the experiment itself, and for the analysis of its results. The knowledge of the acceleration levels reached during the experiment, in fact, has to be necessarily correlated with the outputs, in order to identify foreseen and unforeseen effects.

To achieve this objective, it is needed a tailored instrumentation; several Shuttle flights have hosted experimental systems, that have flown also on the ISS[18],[2]; research in this field is still active[19],[20].

Once available the measurements, the next step is the identification of the source (for ex. vibrations induced by the motion of the crew of the vehicle[21]) and of the level of the accelerations that can be tolerated[22],[23],[24].

From these considerations, it can be concluded that a complete characterization of the acceleration levels proper of an experimental

mission suitable to carry on a microgravity payload[25] is extremely useful.

I.3 Experimental Platforms, and their Classification

A microgravitational environment can be obtained in any non inertial reference frame in which the D'Alembert forces locally counterbalance the Earth gravity acceleration.

It should be noted that it is not the altitude that determines low local values of the gravity acceleration; in fact, for an altitude of 1500 km (by far greater of the normally orbits of 300-500 km) the gravity acceleration of the Earth is about 65 % of its nominal value.

Let's suppose that the considered system is positioned on board of a vehicle with acceleration a_v; applying the Newton's second law to the system with respect to an inertial reference frame, and expressing the relative terms between system and vehicle, we have:

$$F_{rel} + m(g_l - a_v) = ma_{rel} \qquad \textbf{(I - 1)}$$

where F_{rel} and a_{rel} are, respectively, the force and the acceleration of the system with respect to the vehicle (i.e. F_{rel} are the forces that the vehicle exercises on the system), m is the mass of the system and g_l is the local value of the gravity acceleration. If the acceleration of the vehicle is equal to the gravitational field ($a_v = g_l$), the motion of the system with respect to the vehicle is the same of the one in conditions of absence of gravity.

Microgravity conditions can be obtained on board of platforms that move along curved trajectories (orbiting platforms, sounding rockets, aircrafts performing parabolic flights) balancing the local gravity with the centrifugal force, or in free-falling (drop towers) in which $a_v \approx g_l$, and the balancing effect is realised by means of the inertial forces.

Of course, it is never possible to realise exactly the condition of $a_{rel} = g_l$, because of residual disturbances that are always present: angular accelerations, forces acting on the vehicle like the aerodynamic drag, the distance of the system from the centre of mass of the vehicle, internal perturbations like the motion of the astronauts. The value of the residual acceleration, and the time interval in which it can be sustained, characterise the quality of the experimental platform.

In the following Table I - 1[1],[26], are regrouped the principal facilities available today, and their characteristics in terms of microgravity duration and level.

Platform	Microgravity Condition Duration	Microgravity Level Obtainable
Drop towers	2-9 sec	10^{-6}-10^{-2} g
Vehicles performing Parabolic Flights	25 sec	10^{-3}-10^{-2} g
Balloon-drop	60 sec	10^{-3}-10^{-2} g
Sounding Rockets	6 min	10^{-5}-10^{-4} g
Space Shuttle	> 9-11 days	10^{-5}-10^{-3} g
Space Station / Recoverable Satellite	> months	10^{-6}-10^{-5} g

Table I - 1 – Microgravity Facilities, and their Characteristics

In particular, considering parabolic flights, among the various advantages related with them for the conduction of microgravity experiments there are[26]:

► Short Turnaround time (typically in the order of months) between the proposal of the experiment and its realisation;

► Low costs;

► Flexible approach to the experiment (for example, it is possible to

use common laboratory instrumentation);

► Possibility of direct intervention of the scientist on board of the

vehicle, and between the flights;

► Possibility to modify the experiment set-upbetween the flights.

In the following Fig. I - 1 it is shown the typical mission profile of an
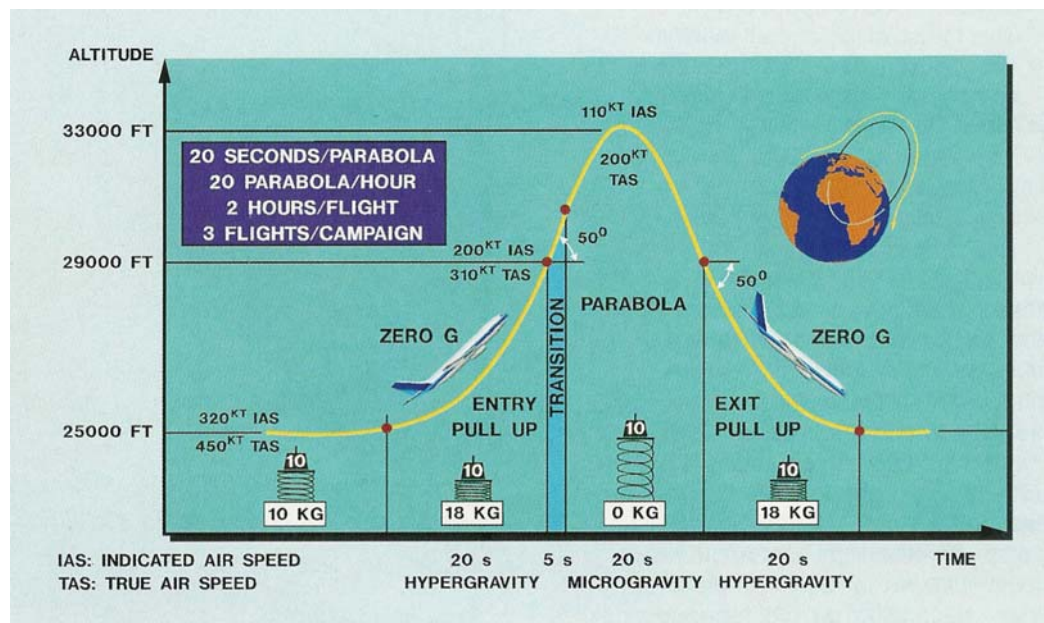
ESA parabolic flight[26].

Fig. I - 1 – The Parabolic Flight Manoeuvre

I.4 The PRORA-USV Program

The PRORA-USV program has a twofold objective[27]:

► To ensure a technological focus on the future reusable space transportation vehicles;

► To provide the scientific community with targeted tools for research activities aimed to identify, develop, and validate a number of necessary key technologies as representative of the needs for future generation reusable space transportation vehicles.

In the frame of the PRORA two types of FTBs are planned to be developed. The short term FTB is to perform multiple dropped flight test missions, both in transonic and supersonic regime. The long term FTB is dubbed to perform a sub-orbital re-entry test mission. The first USV1 mission is a Dropped Transonic Flight Test scheduled for the end of 2005.

The DTFT mission is aimed at experimenting the transonic flight of a re-entry vehicle. The mission will be carried out by the first Flight Test Bed (FTB_1) conceived as a Flying Laboratory, capable of testing technologies for next generation Launch Vehicles in the subsonic, transonic and low supersonic phase of a re-entry trajectory.

USV1 is a project based on a stratospheric balloon. The basic operation consist of three main phases: the ascent phase during which the carrier bring the FTB_1 at the release altitude by means of the balloon; the flight phase in which the FTB_1 leaves the carrier and starts flying accelerating to achieve the required velocity to perform the experiments; the deceleration phase in which the FTB_1 opens the parachute and ends its mission by water splash down.

Fig. I - 2 shows the USV1 flight envelope in the plane Mach-altitude. In particular the releasing altitude can range from 10 km up to 35 km and the maximum Mach number can be about 1.8. It means that the parachute can be opened in this range working properly and efficiently. This allows performing different flight profiles with different mach and altitude in order to fulfil several mission requirements and experiments needs, in accordance with flexibility use of the flying laboratory. The only constraint is imposed by the parachute opening safety area that defines the trajectory segment where it is possible to open the vehicle parachute in a safe way, namely ensuring that the load factors on the parachute will remain below its structural limits, and that, after the opening, the vehicle will perform the splash-down within the safety geographical area (see Fig. I - 3), limited by the ground path associated to the nominal trajectory.
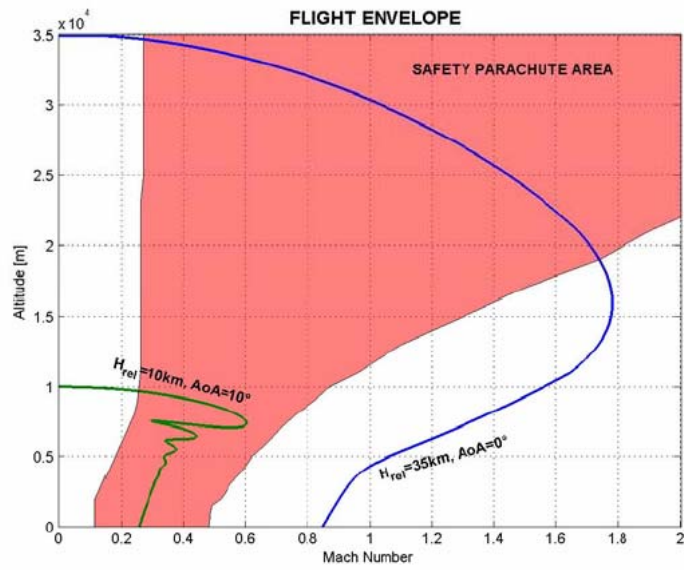
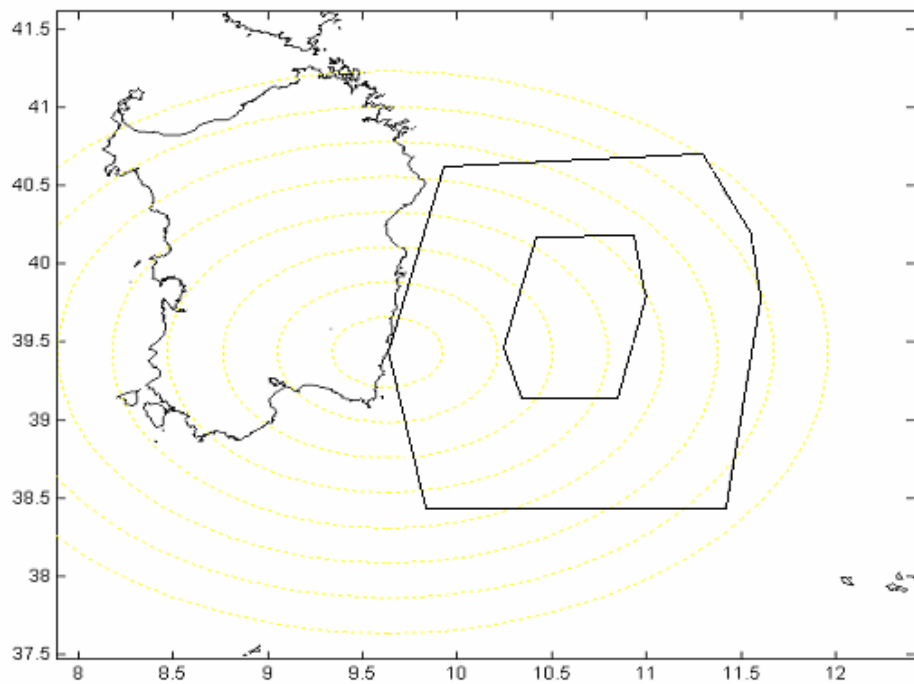**Fig. I - 2 – USV1 Flight Envelope**

Fig. I - 3 – Mission Safety Area

The FTB_1 is a slender, not-propelled, winged vehicle able to perform experiments on Structure and Materials, Autonomous Guidance Navigation and Control, and Thermo-Aerodynamics. The FTB_1 external configuration has been developed assuming the following design drivers:

► aerodynamic efficiency of L/D > 2.5 from transonic to supersonic;

► maximum thickness of wing profile: 8%;

► nominal nose radius : < 50 mm;

► a four-vertical-fin configuration has been introduced in order to reduce interference with wing, with parachute at deployment, and structural constraints; as well as tomatch stability and control requirements.

In the Fig. I - 4 the overall external configuration of the FTB_1 winged vehicle is shown.

Fig. I - 4 – FTB_1 External Configuration

The FTB1 vehicle as Flying Laboratory is able to host experimental payload on-board and provide the needed resources to perform the experiments during the mission accomplishment. Therefore the first FTB vehicle is able to accommodate an experimental payload of 30 Kg inside the Avionic Bay and 20 Kg outside the Avionic Bay, with a volume of 650x377x180 mm^3 inside the Avionic Bay and provide a power of 616 W. The Fig. I - 5 shows the payload dedicated volume and allocation (red boxes) established for FTB1 vehicle.
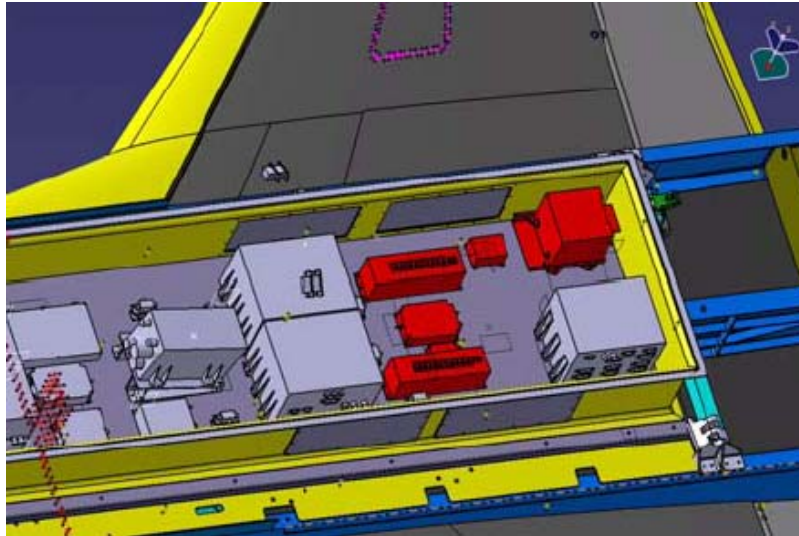
Fig. I - 5 – FTB_1 Payload Accomodation

The experiments that will be carried on during the first flights are the following:

Aerodynamics

The aerodynamic characterization of a space vehicle crossing the transonic portion of a re-entry trajectory is made difficult by the strong variability of the aerodynamic coefficients typical of this regime and mainly due to strong non linearity of the flow field induced by the growing of shock wave over the vehicle surface and to vortex separation. Moreover, the need for peculiar design solutions, as for instance the truncated base, makes harder the accurate determination of the

aerodynamic parameters. In this framework it seems really important to have the way to perform comparison between the aerodynamic performance foreseen by means of a suitable aerodynamic model and flight measurements. Main benefits obtainable by gathering in-flight data may be recognized in the following:

1. Verification of predictive capabilities of Computational Fluid Dynamics (CFD) codes for a complex configuration in flight condition.

2. Verification of the suitability of the Wind-Tunnel Test methodology.

3. Verification and tuning of the methodology for the extrapolation to flight condition of the experimental measurements.

4. Reduction of the uncertainties margin associated with the pre-flight prediction of the aerodynamic coefficient.

The logical path for the comparison between Pre-Flight/In-Flight data will be actuated by means of the acquisition during the USV_1 flight both of the global aerodynamic coefficients (inertial measurements) and local quantities (pressure distribution).

Structural Mechanics

During the first transonic and supersonic mission of USV_1 two experimental tests will be performed in order to identify the external loads and aeroelasticity behaviour of the vehicle. The objectives of these experiments are in accordance with USV – PRORA step by step development approach:

► Technical risk minimisation;

► Improvement of analysis and design capabilities.

External Loads Evaluation

Evaluation of external load acting on the USV_1 vehicle will allow achieving two main objectives: validation of loads extraction methods and verification of structural design methods.

A set of calibrated strain gauges will be installed on the vehicle in order to evaluate the main external loads components due to aerodynamic loads as shear, bending moment and pitching moment or torque. The steps for the in flight evaluations are:

► Selection of strain-gauge measurements;

► Installation of sensors on board;

► Transfer function evaluation by means of ground static calibration;

► In flight acquisition;

► Post flight elaboration.

The external loads evaluation will be correlated with the basic flight parameters (symmetrical and anti-symmetrical ones) in order to identify the acting manoeuvre.

Moreover the evaluation of flight loads will allow the determination of inspection level (partial or total) for the a/c reusability.

Aeroelasticity Evaluations

The objectives of the aeroelasticity evaluations will allow the determination of the dynamic behaviour of the a/c during the flight. The main interest is the validation of numerical aeroelastic model developed during the USV_1 design. In particular this experiment will allow the validation of the aeroelastic model in transonic flight.

The experiment will be dived into two steps.

During the first step a new aeroelastic model will be implemented using the results of Ground Vibration Test (GVT). This test will be performed

using CIRA facilities. The second step will consist in the acquisition, during the flight, of acceleration history in terms of amplitude frequency and damping. The acceleration histories of the wing, fuselage and empennages will be acquired by means of a set of flight accelerometers placed into the USV_1.

Chapter II

Characteristics of the FTB_1 Vehicle

II.1 General Characteristics

In this paragraph there will be described the main characteristics of the FTB_1 vehicle; in particular there will be indicated all its geometrical and inertial properties[28].

The nominal Centre of Mass (hereinafter C.o.M) position considered will be the following, expressed in the Layout Reference Frame (Fig. II - 1, see Appendix 2):

► $X_{C.o.M.} = 5.64$ m

► $Y_{C.o.M} = 0$

► $Z_{C.o.M.} = -0.15$ m

The values of the reference dimensions used to dimensionalise the aerodynamic coefficients are reported in the following table.

S_{ref}	Ref. Surface		m^2	3.6
L_{ref}	Ref. Chord	*Longitudinal Actions*	m	1.05
b_{ref}	Wing Span	*Lateral-directional Actions*	m	3.56

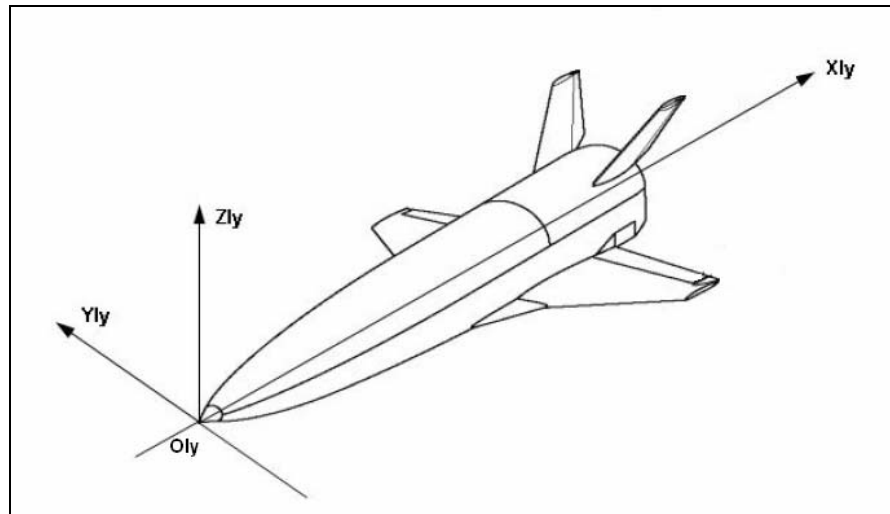**Table II - 1 – Reference Quantites**

Fig. II - 1 – Layout Reference Frame

Finally, the inertial characteristics of the vehicle are reported in the following table:

m	1250	Vehicle Mass	Kg
I_{xx}	2.787E+02	Moment of Inertia along *x*-axis, in a body reference frame	Kg·m²
I_{yy}	4.2482E+03	Moment of Inertia along *y*-axis, in a body reference frame	Kg·m²
I_{zz}	4.3171E+03	Moment of Inertia along *z*-axis, in a body reference frame	Kg·m²
I_{xz}	2.301E+01	Product of Inertia in the *xz*-plane, in a body reference frame	Kg·m²
I_{xy}	4.6E+00	Product of Inertia in the *xy*-plane, in a body reference frame	Kg·m²
I_{zy}	4.360E+00	Product of Inertia in the *zy*-plane, in a body reference frame	Kg·m²

Table II - 2 – Inertial Characteristics of the Vehicle

II.2 Flyability Analysis

II.2.a   Introduction

The scope of this analysis is the investigation of the flyability characteristics of the FTB_1 vehicle, considering both the cases of nominal aerodynamic dataset and of aerodynamic coefficients affected by uncertainties[29],[30].

The analysis is conducted with reference to a properly chosen operative/aerodynamic envelope (for the nominal case) and to suitable trajectories (for the dispersed case); it essentially consists in a complete dynamic characterisation of the vehicle, in terms of trimmability, manoeuvrability and stability properties.

II.2.b Aerodatabase Analysis and Reference Trajectory Definition

II.2.b.1 Flight Envelope

In the following of the analyses, all the aerodynamic force and moment
coefficients:

C_L	Lift Coefficient
C_D	Drag Coefficient
C_Y	Side Force Coefficient
C_l	Rolling Moment Coefficient
C_m	Pitching Moment Coefficient
C_n	Yawing Moment Coefficient

and their derivatives, will be defined as a function of some or all of the
following variables; in Table II - 3, for each of the variables is also
indicated the range considered[1].

Variable			Range
M	Mach Number		$[0.1:1]$
Re	Reynolds Number		$[5 \cdot 10^5 : 9 \cdot 10^6]$
α	Angle of Attack	deg	$[-5:18]$
β	Angle of Sideslip	deg	$[-8:8]$
δ_{e*}	Horizontal Control Surface Deflection (* = Left/Right)	deg	$[-20:20]$
δ_r	Vertical Control Surface Deflection	deg	$[-20:20]$

Table II - 3– Independent Variables defining the Flight Envelope

---

[1] For further details on the aerodynamic coefficients and their functional dependencies,
see also Appendix 1, 2.

Beside the variables introduced in Table II - 3, the coefficients will result also function of the vehicle Centre of Mass location, defined in the Layout Reference Frame (LRF) - Fig. II - 1.

In order to perform the flyability analysis, a preliminary evaluation of the aerodynamic database characterising the vehicle has been executed. Its main characteristics can be summarised as it follows:

► The aerodatabase is directly dependant on [M, α, β, δ_{eRight}, δ_{eLeft}, δ_r, X_{CoM}, Z_{Com}], but not explicitly on the Reynolds number;

► 4 different database have been supplied, correspondent to 4 different representative Reynolds Number (Re = [$5 \cdot 10^5$; $1 \cdot 10^6$; $3 \cdot 10^6$; $9 \cdot 10^6$]). Linear interpolation between databases has been declared as applicable by the databases provider; however, in the present analysis, just data corresponding to exact provided Reynolds number have been used and it has not been performed linear interpolation.

In Fig. II - 2 and Fig. II - 3 are graphically showed the longitudinal and lateral-directional coefficients, as a function of the angle of attack, for different values of the Mach and Reynolds numbers and for different configurations (i.e. different values for δ_e, β, δ_r).

As it can be seen, there is almost no difference between the coefficients, both longitudinal and lateral-directional, calculated for Re = $5 \cdot 10^5$ and Re = $1 \cdot 10^6$, and between the ones corresponding to Re = $3 \cdot 10^6$ and Re = $9 \cdot 10^6$.
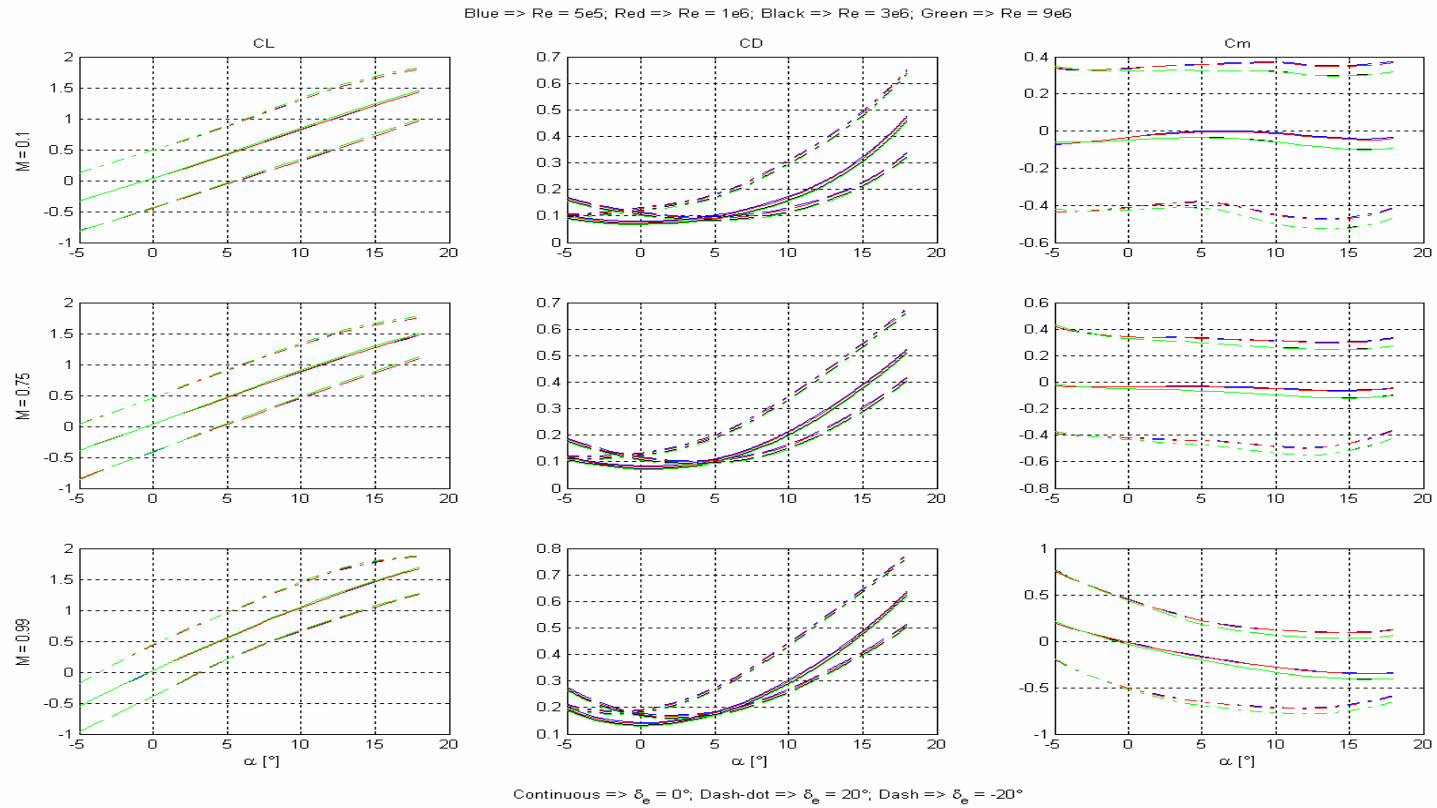
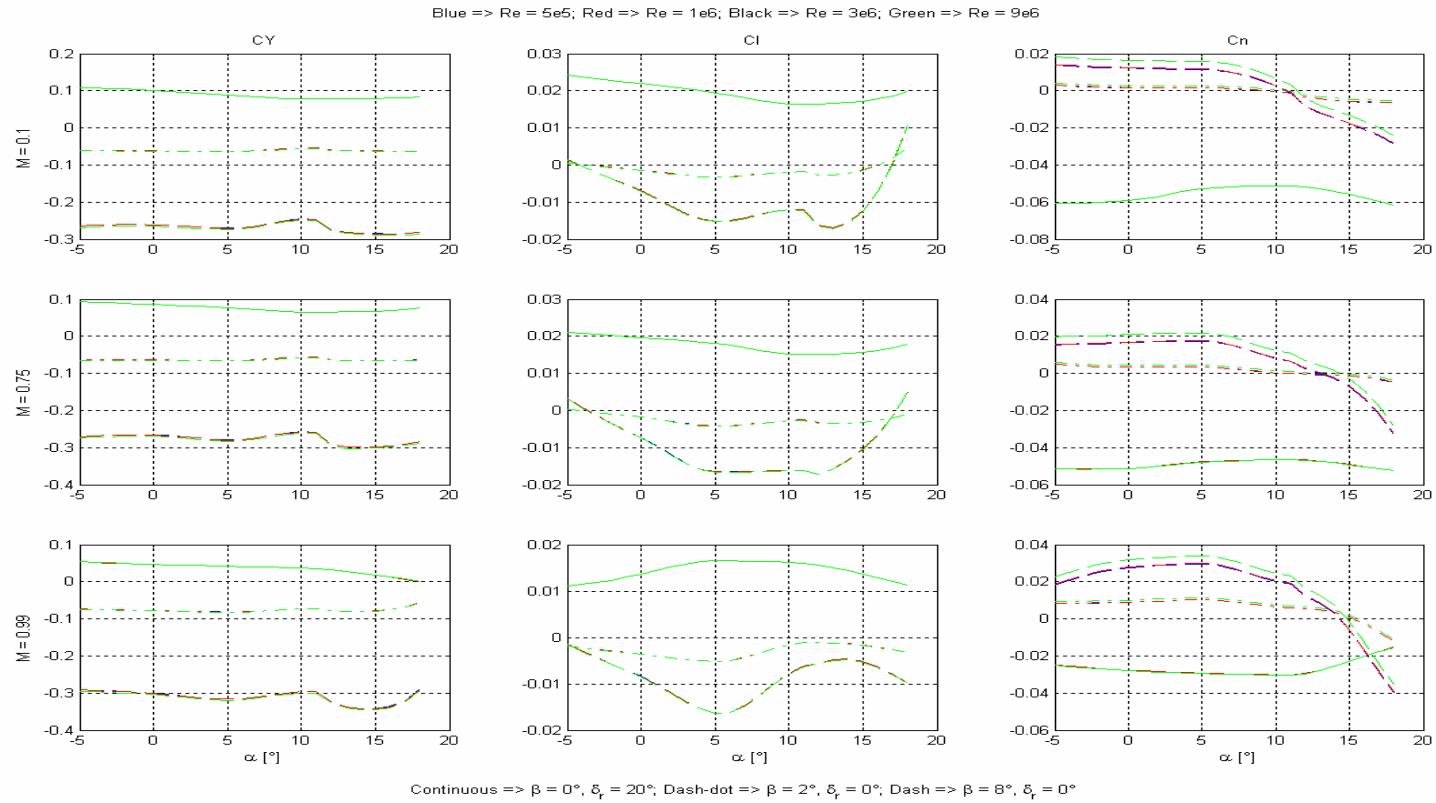**Fig. II - 2 – Longitudinal Static Coefficients – Dataset Comparison**

Fig. II - 3 – Lateral-Directional Static Coefficients – Dataset Comparison

II.2.b.2   Reference Trajectory

In order to define the reference trajectory for the FTB_1 mission, an optimization process has been carried out whose description is not hereafter detailed[31]. The resulting nominal trajectory is characterized by the fulfilment of all the mission requirements and safety constraints with a strictly longitudinal motion and a constant angle of attack in the transonic regime of flight.

The below reported *point-of-mass* model has been used in which the command input is the angle of attack α, *m* is the vehicle mass, *g* the gravity acceleration, *L* and *D* are the aerodynamic actions, computed in trimmed conditions and hence they also take into account the pitching moment aerodynamic coefficient C_m.

$$
\begin{cases}
\dot{h} = -V\sin\gamma \\[2mm]
\dot{V} = -\dfrac{D}{m} - g\sin\gamma \\[2mm]
\dot{\gamma} = \dfrac{L}{mV} - \dfrac{g}{V}\cos\gamma
\end{cases}
\qquad \textbf{(II - 1)}
$$

In this model, h is the altitude, V the inertial velocity modulus, and γ the flight-path angle.

The reference trajectory, in terms of Mach-altitude path, commanded angle of attack and pitch angle is depicted in the following Fig. II - 4 to Fig. II - 6.
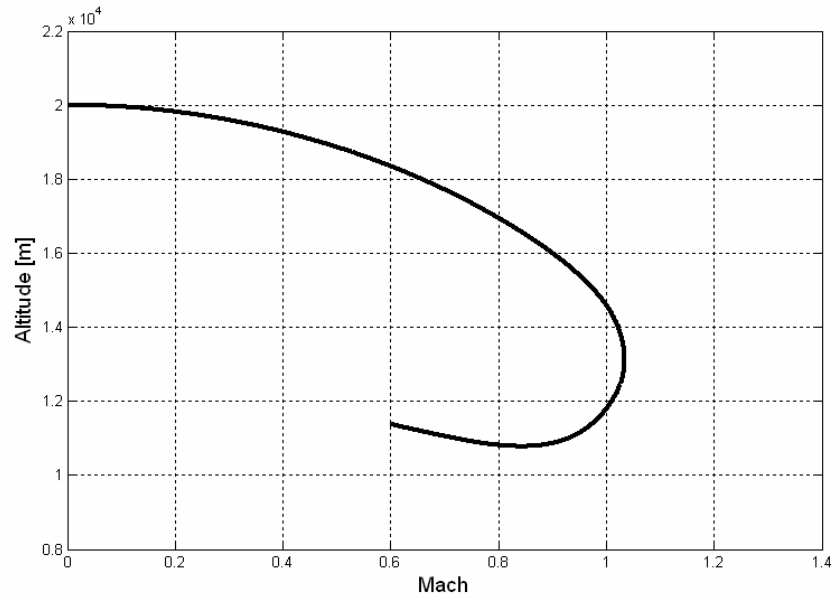

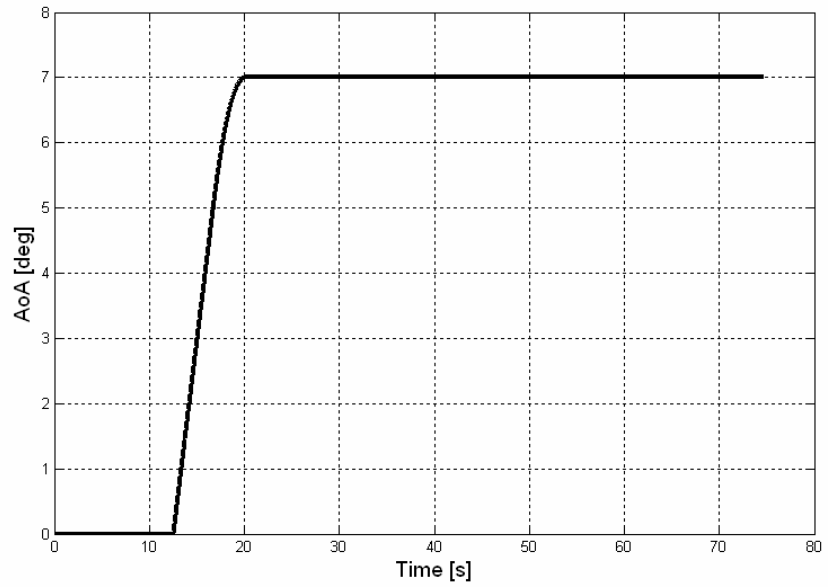**Fig. II - 4 – Reference Trajectory – Mach vs. Altitude**

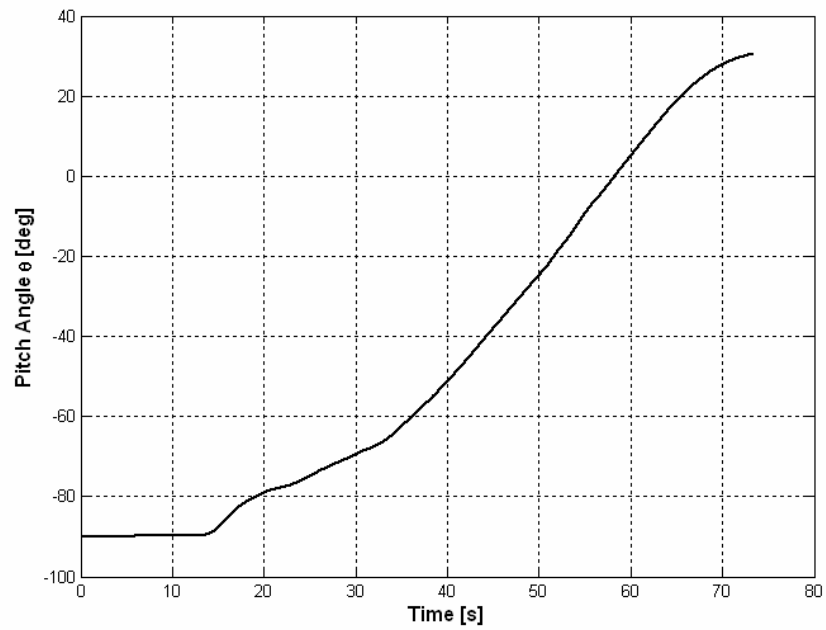**Fig. II - 5 – Reference Trajectory – Commanded Angle of Attack Profile**

Fig. II - 6 – Reference Trajectory – Pitch Angle Profile

II.2.b.3 Conclusions

From an analysis of Fig. II - 2 to Fig. II - 6, the following conclusions can be drawn:

1. Two of the considered database are significantly different, the one at Re=$1 \cdot 10^6$ and that one at Re=$3 \cdot 10^6$. The others (Re=$5 \cdot 10^5$; Re=$9 \cdot 10^6$) are respectively similar to the examined. The following analyses will so be conducted considering only these two databases.

2. Having selected two databases of interest, the calculation of the stability and manoeuvrability parameters will be carried on selecting points in the flight envelope, using a grid characterised by the following defining vectors:

    ► M = [0.1; 0.3; 0.5; 0.7; 0.8; 0.85; 0.9; 0.94; 0.96; 0.99]; this vector has been built up from the test values used in the wind tunnel test campaign;

    ► $\alpha \in$ [-5° : 18°], with a sampling interval of 1°.

3. Standing the characteristic of the reference trajectory to be constrained in a longitudinal plane, the sideslip angle β will be considered identically = 0.

A more complete collection of results is available in [29].

II.2.c   *Methodology and Tools*

II.2.c.1   Trimmability   and   Manoeuvrability
Analysis

The manoeuvrability of the vehicle will be quantified in terms of a Manoeuvrability Margin defined as:

$$
\text{M.M.} = \frac{\delta_{e\_MAX} - \left|\delta_{e\_TRIM}\right|}{\delta_{e\_MAX}}
$$

$$
\Downarrow
$$

$$
\text{M.M.}_{\%} = \text{M.M.} \cdot 100
$$

(II - 2)

In Eq. (II - 2):

► δ_{e_MAX} is the maximum allowable elevon deflection[2],

► δ_{e_TRIM} is the trimming deflection value, i.e. the value for which is verified the condition:

---

[2] In case of sideslip angle β = 0, in fact, the trim condition is achieved by means only of the horizontal control surfaces, actuated symmetrically.

$$C_m(\alpha, M, \delta_e) = 0 \qquad\qquad \textbf{(II - 3)}$$

The angular rates p, q, r are considered =0; for all the manoeuvrability

analysis, a δ_{e_MAX} value of ±20° has been considered.

In the following chapters, there will be reported the trimmability and

manoeuvrability charts in the envelope [α, M] identified in § II.2.b.1, and

for both Reynolds = $1 \cdot 10^6$ and $3 \cdot 10^6$.

II.2.c.2   Dynamic Stability Analysis

The stability analyses will be conducted considering only the dynamic

stability properties: both the longitudinal and lateral-directional dynamic

stability analyses will be carried on using linearised models obtained by

means of a linearization of the non-linear equation of motion of the

vehicle (see Appendix 2). Given the dynamical matrices describing the

models, there will be performed an evaluation of their eigenvalues,

standing the property that stability is guaranteed if all of them present

real part < 0.

In order to build the linearised models , it is also necessary to find, for

each couple (M, Re) defining the aerodynamic coefficients (see §

II.2.b.1) the unique corresponding couple (V, Altitude). This can be done

on the basis of the geometrical characteristics of the vehicle and of the

physical parameters characterising the atmosphere model.

We have:

$$
\begin{cases}
M = \dfrac{V}{a} \\
Re = \dfrac{\rho \cdot V \cdot L_{ref}}{\mu}
\end{cases}
\rightarrow V = M \cdot a \rightarrow Re = \dfrac{\rho \cdot M \cdot a \cdot L_{ref}}{\mu}
$$

$$\downarrow$$

$$
\frac{Re}{M \cdot L_{ref}} = \frac{\rho \cdot a}{\mu} = f(\text{Altitude})
\qquad \textbf{(II - 4)}
$$

$$\Downarrow$$

$$
\text{Altitude} = f^{-1}\left(\frac{\rho \cdot a}{\mu}\right) = f^{-1}\left(\frac{Re}{M \cdot L_{ref}}\right)
$$

The function f is dependent on the atmosphere model considered, and

can be numerically inverted. In the present analysis the US 76 Standard

Atmosphere Model has been used. Given the value of the Altitude, is

possible to find the value of the speed of sound, a, and then, using the

value of the Mach number, it is possible to calculate the velocity V.

The results of the stability analyses will be shown in the following, by

means of the maps of the maximum real part of the linearised system

eigenvalues. Five different values of the pitch angle θ, i.e. $\theta = [30°, 0°, -$

30°, -60°, -89°] have been analysed, so covering the complete pitch range
of interest for the missions (see Fig. II - 6).

Being the sideslip angle $\beta = 0°$, the longitudinal and lateral-directional
dynamics can be separated; about the first one, the analysed model can be
further modified, neglecting the translational dynamics, i.e. considering
only the state variables α and q. This has been done in order to focus on
the rotational (short period) stability properties of the vehicle. Thus, in
the considered flight conditions, the equations of motion to be analysed
are:

$$\dot{\alpha} = q - \frac{L}{m\mathrm{V}} + \frac{g}{\mathrm{V}} \cdot \cos(\theta - \alpha) \qquad \textbf{(II - 5)}$$

$$\dot{q} = \frac{m}{\mathrm{I}_{yy}} \qquad \textbf{(II - 6)}$$

All the considered conditions are always characterised by

►   Trim value for the surfaces deflections;

►   Angular rates p, q, r identically = 0.

As already stated, in the following paragraphs, the stability
characteristics of the vehicle will be expressed by means of maps and

contours of the maximum real part of the eigenvalues. In all the maps

that will be shown, the adopted convention for the colours is:

► Red → Instability (maximum real part of eigenvalues ≥ 0);

► Green → Stability (maximum real part of eigenvalues < 0).

II.2.c.3   Effect of Uncertainties Evaluation

The adopted aerodynamic uncertainties model is the following:

$$C_L = C_L^*(M, Re, \alpha, \beta, \delta_{e\_right}, \delta_{e\_left}, \delta_{r\_right}, \delta_{r\_left}, \dot{\alpha}, q, X_{COM}, Y_{COM}, Z_{COM})$$
$$\pm C_{L0}^{unc}(M) \pm C_{L\alpha}^{unc}(M) \cdot \alpha \pm C_{L\delta_e}^{unc}(M) \cdot \delta_e \pm C_{L\dot{\alpha}}^{unc}(M) \cdot \frac{\dot{\alpha}c}{2V} \pm C_{Lq}^{unc}(M) \cdot \frac{qc}{2V}$$

$$C_D = C_D^*(M, Re, \alpha, \beta, \delta_{e\_right}, \delta_{e\_left}, \delta_{r\_right}, \delta_{r\_left}, \dot{\alpha}, q, X_{COM}, Y_{COM}, Z_{COM})$$
$$\pm C_{D0}^{unc}(M) \pm C_{D\alpha^2}^{unc}(M) \cdot \alpha^2 \pm C_{D\delta_e}^{unc}(M) \cdot \delta_e$$

$$C_m = C_m^*(M, Re, \alpha, \beta, \delta_{e\_right}, \delta_{e\_left}, \delta_{r\_right}, \delta_{r\_left}, \dot{\alpha}, q, X_{COM}, Y_{COM}, Z_{COM})$$
$$\pm C_{m0}^{unc}(M) \pm C_{m\alpha}^{unc}(M) \cdot \alpha \pm C_{m\delta_e}^{unc}(M) \cdot \delta_e \pm C_{m\dot{\alpha}}^{unc}(M) \cdot \frac{\dot{\alpha}c}{2V} \pm C_{mq}^{unc}(M) \cdot \frac{qc}{2V}$$

Table II - 4 – Longitudinal Coefficients Uncertainties Model

$$C_Y = C_Y^*(M, Re, \alpha, \beta, \delta_{e\_right}, \delta_{e\_left}, \delta_{r\_right}, \delta_{r\_left}, p, r, X_{COM}, Y_{COM}, Z_{COM})$$

$$\pm C_{Y\beta}^{unc}(M) \cdot \beta \pm C_{Y\delta_r}^{unc}(M) \cdot \delta_r \pm C_{Y\delta_a}^{unc}(M) \cdot \delta_a \pm C_{Yp}^{unc}(M) \cdot \frac{pb}{2V} \pm C_{Yr}^{unc}(M) \cdot \frac{rb}{2V}$$

$$C_l = C_l^*(M, Re, \alpha, \beta, \delta_{e\_right}, \delta_{e\_left}, \delta_{r\_right}, \delta_{r\_left}, p, r, X_{COM}, Y_{COM}, Z_{COM})$$

$$\pm C_{l\beta}^{unc}(M) \cdot \beta \pm C_{l\delta_r}^{unc}(M) \cdot \delta_r \pm C_{l\delta_a}^{unc}(M) \cdot \delta_a \pm C_{lp}^{unc}(M) \cdot \frac{pb}{2V} \pm C_{lr}^{unc}(M) \cdot \frac{rb}{2V}$$

$$C_n = C_n^*(M, Re, \alpha, \beta, \delta_{e\_right}, \delta_{e\_left}, \delta_{r\_right}, \delta_{r\_left}, p, r, X_{COM}, Y_{COM}, Z_{COM})$$

$$\pm C_{n\beta}^{unc}(M) \cdot \beta \pm C_{n\delta_r}^{unc}(M) \cdot \delta_r \pm C_{n\delta_a}^{unc}(M) \cdot \delta_a \pm C_{np}^{unc}(M) \cdot \frac{pb}{2V} \pm C_{nr}^{unc}(M) \cdot \frac{rb}{2V}$$

Table II - 5 – Lateral-Directional Coefficients Uncertainties Model

With the asterisk they have been indicated the nominal values of the coefficients.

As it can be seen, the uncertainties coefficient are function only of the Mach number; moreover, it is noticeable that the model is structured, i.e. it is directly supplied in the form of the stability derivatives.

The values of the uncertainties coefficient are reported in Appendix 3; they have to be intended as 2-σ conditions, and will be used for the here described evaluations.

It is worth noting that the uncertainties are supplied in two different versions, one that have to be used when it is necessary to perform a build up like the one described in Table II - 4 and Table II - 5, and one that have to be used when the aerodynamic coefficients are considered one by

one. In Table A.3 – 1 are indicated the coefficients for the first case,

while in Table A.3 – 2 are indicated the coefficients for the second case.

Given these tables, a rigorous approach to the treatment of uncertainties

should consider the evaluation of all their possible combination, for each

flight condition, and the identification of the worst (and, eventually, the

best) one.

In order to avoid this huge computational load, but to still obtain

significant information, some properly defined trajectories that limit the

mission flight envelope can be analysed. Then, a combination of

uncertainties that lead to the worst and best conditions for the criteria

under evaluation is applied[30].

Simply considerations about the model and the reference command

input allow to state that the aerodynamic uncertainties defining the

boundary trajectories correspond to conditions characterized by

maximum efficiency ratio L/D with minimum ballistic parameter

$W/C_D.S$, and vice versa[31]. It is easily proven that, for the mission at hand

(with positive values of AoA and negative values of elevons deflection

for trim) the extreme values of efficiency ratio and ballistic parameter

can be obtained with the following uncertainty combination, respectively:

$$[\Delta C_{L0MAX}, \Delta C_{L\alpha MAX}, \Delta C_{L\,\delta eMIN}], [\Delta C_{D0MAX}, \Delta C_{D\alpha\,MAX}, \Delta C_{D\,\delta eMIN}],$$
$$[\Delta C_{m0MAX}, \Delta C_{m\alpha\,MAX}, \Delta C_{m\,\delta eMIN}]$$
$$[\Delta C_{L0MIN}, \Delta C_{L\alpha\,MIN}, \Delta C_{L\,\delta e\,MAX}], [\Delta C_{D0MIN}, \Delta C_{D\alpha\,MIN}, \Delta C_{D\,\delta e\,MAX}],$$
$$[\Delta C_{m0MIN}, \Delta C_{m\alpha\,MIN}, \Delta C_{m\,\delta e\,MAX}]$$

(II - 7)

In Fig. II - 7 the resulting boundary trajectories are shown, in terms of Mach-Altitude paths; the Angle of Attack profile is the same of the reference trajectory introduced in § II.2.b.2.
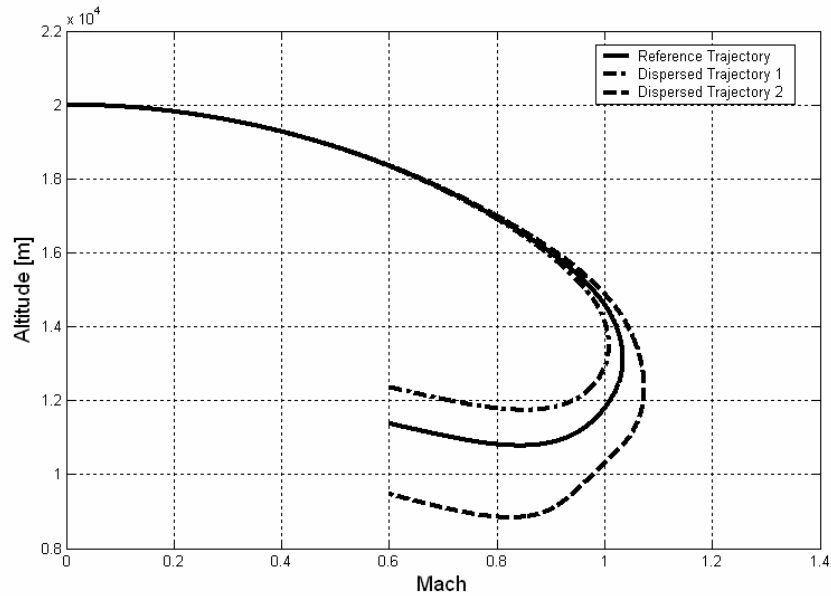
Fig. II - 7 – Reference and Boundary Trajectories – Altitude vs. Mach

These trajectories have been calcolated considering nominal structural parameters (CoM position, inertia matrix) and initial conditions (altitude, angular velocity vector).

It is worth to note that, as the applied uncertainty sets also produce the pitching moment values requiring respectively the lowest trim power (best manoeuvrability condition) and the highest trim power (worst manoeuvrability condition), the boundary trajectories of Fig. II - 7 will also correspond to the best and worst manoeuvrability conditions.

On the other hand, concerning stability and other dynamic properties (flying qualities), an analysis performed only on the above trajectories (and the associated uncertainty combinations) cannot be in principle assumed as completely characterizing the vehicle behaviour inside the envelope. Thus in order to obtain representative results some other considerations shall be applied[30].

First of all, it shall be noted that even if the trajectory solution of model (II - 7) is strictly dependent from the considered aerodatabase (which also means that the drag and lift time-histories are univocally defined along the trajectories), the presence of the uncertainty parameters can be used in order to obtain the same state variables trajectories with several different combinations of uncertainties. As a matter of fact, if we consider the relations in Table II - 4, Table II - 5, it can be easily verified that there is an infinite number of parameter combinations that give the same overall uncertainty values. Indeed, given ΔC_L, ΔC_D and ΔC_m values,

there are still 11 degree of freedom to be exploited (trim elevons deflection included).

This consideration can be used to justify the second step of the proposed approach. Indeed, considering that the aerodynamic derivatives affecting the longitudinal stability essentially are:

$$C_{L_\alpha}, C_{m\alpha}, C_{mq}, C_{m\dot{\alpha}} \qquad \textbf{(II - 8)}$$

the uncertainties on these coefficients can be freely varied, taking into account that the other uncertainty parameters can be exploited in order to still obtain the three selected trajectories (and thus the associated lift and drag time histories). This allows to use the uncertainty combinations that lead to the worst and best longitudinal stability conditions over the same trajectories. Similar consideration can be also performed for what concern the lateral-directional stability investigation.

Actually, the above procedure is rigorously applicable only when the uncertainty ranges are not limited. Obviously, in real cases, this assumption is never verified. The limited ranges of the uncertainties also limits the number of stability derivatives uncertainty combinations that give the same considered trajectories. As for the subsequent longitudinal

stability analyses it is not considered these limitation, some conservatism is introduced in the results. This last consideration does not apply to the lateral directional stability results, because, in this case, all the considered trajectories are not influenced by the lateral directional coefficients.

In conclusion, the below reported analysis results can be definitely considered well representative of the vehicle worst and best dynamic behaviour on all the possible mission trajectories.

II.2.d   Analysis of the Results

II.2.d.1   Trimmability and Manoeuvrability Analysis
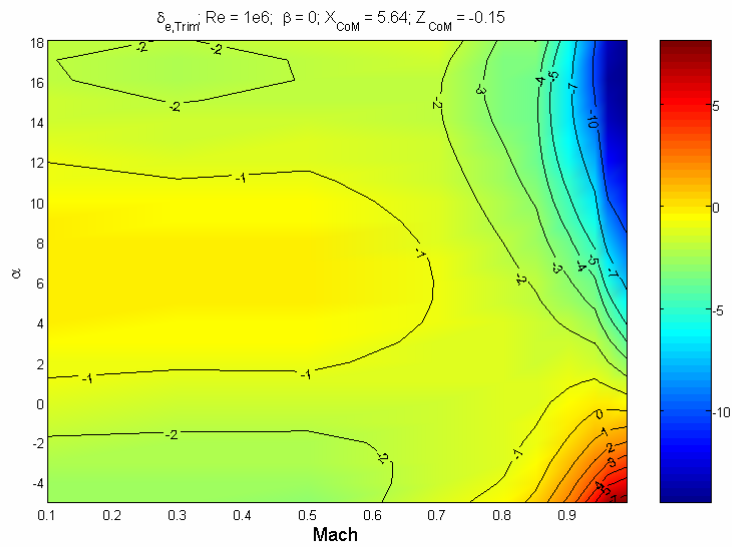
Fig. II - 8 – Trimmability Chart – Re = 1e6, β = 0°
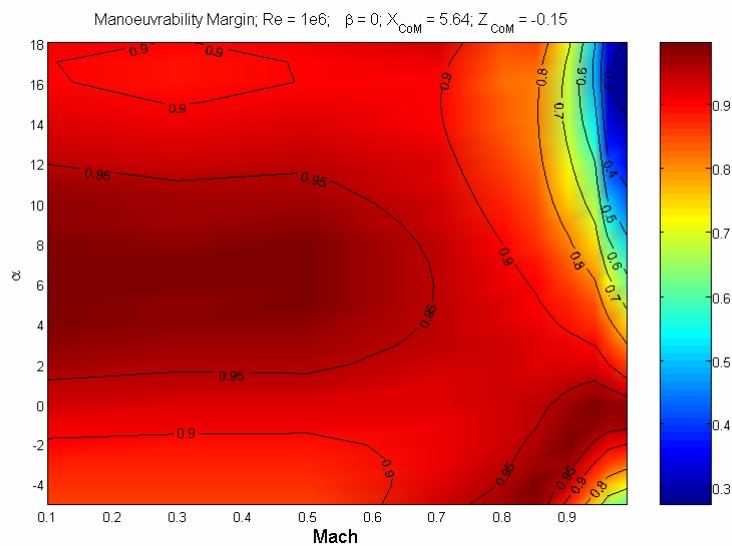
Fig. II - 9 – Manoeuvrability Margin – Re = 1e6, β = 0°
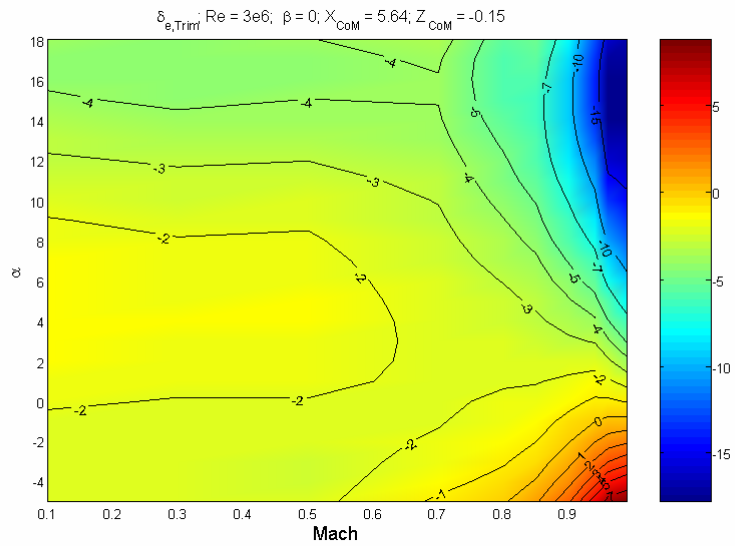
Fig. II - 10 – Trimmability Chart – Re = 3e6, β = 0°
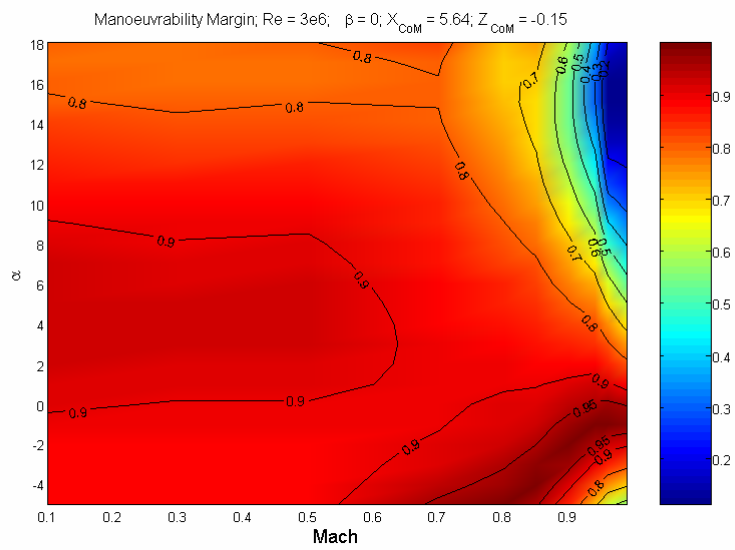
Fig. II - 11 – Manoeuvrability Margin – Re = 3e6, β = 0°

II.2.d.2   Dynamic Stability Analysis

II.2.d.2.1   Longitudinal Stability
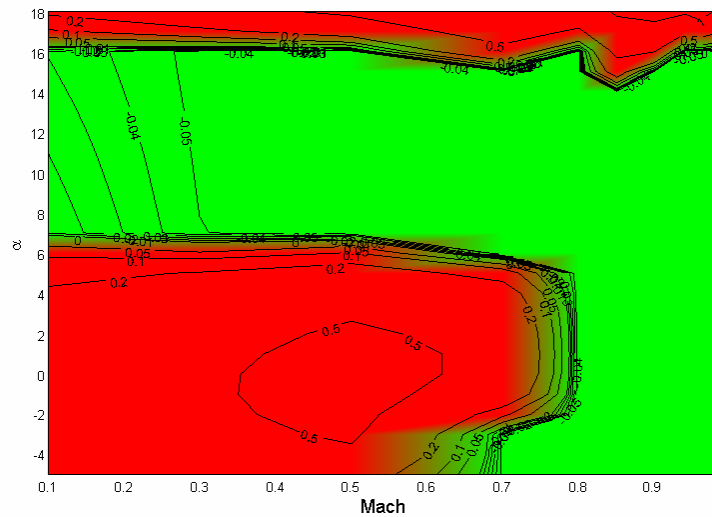
**Fig. II - 12 – Real Part of the Longitudinal Eigenvalues, Short Period
Approximation – Re = 1e6, β = 0°, θ = 30°**
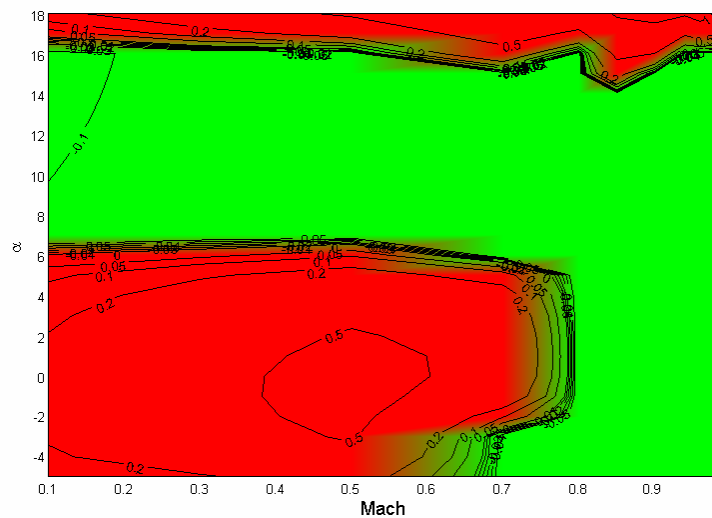
**Fig. II - 13 – Real Part of the Longitudinal Eigenvalues, Short Period
Approximation – Re = 1e6, β = 0°, θ = 0°**
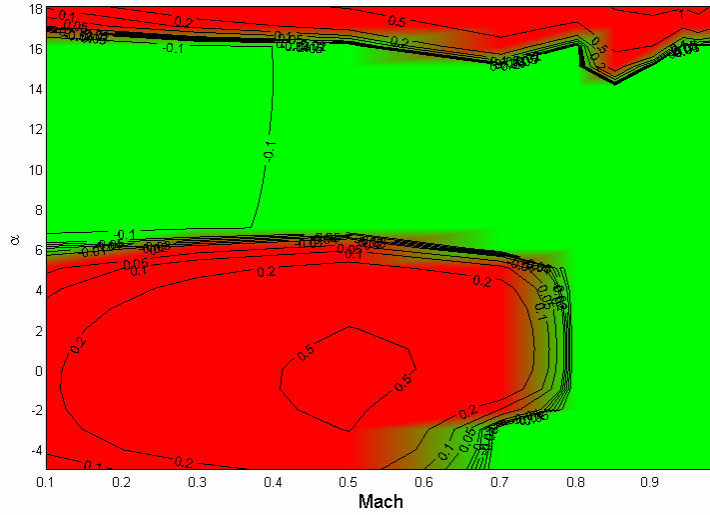
Fig. II - 14 – Real Part of the Longitudinal Eigenvalues, Short Period Approximation – Re = 1e6, β = 0°, θ = -30°
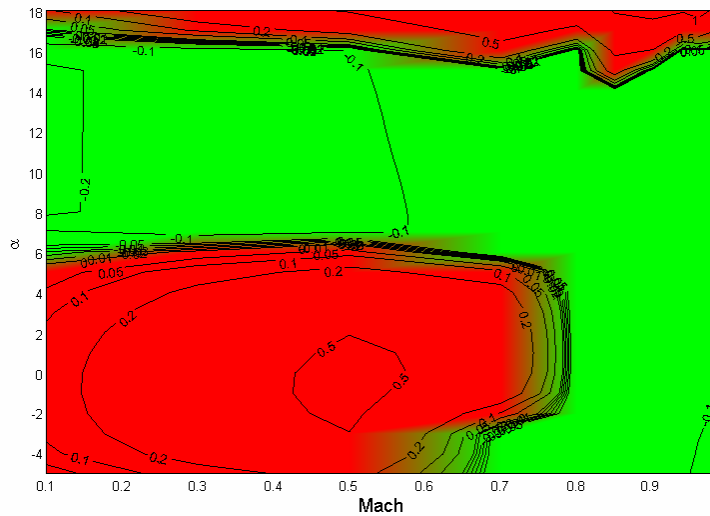
Fig. II - 15 – Real Part of the Longitudinal Eigenvalues, Short Period Approximation – Re = 1e6, β = 0°, θ = -60°
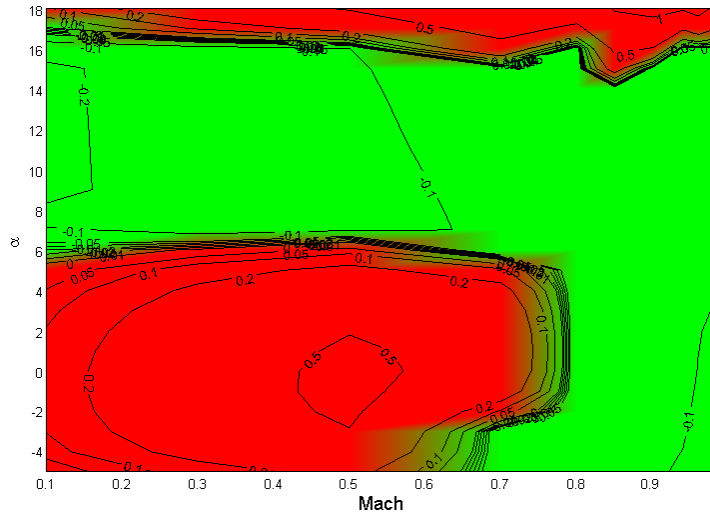
**Fig. II - 16 – Real Part of the Longitudinal Eigenvalues, Short Period
Approximation – Re = 1e6, β = 0°, θ = -89°**
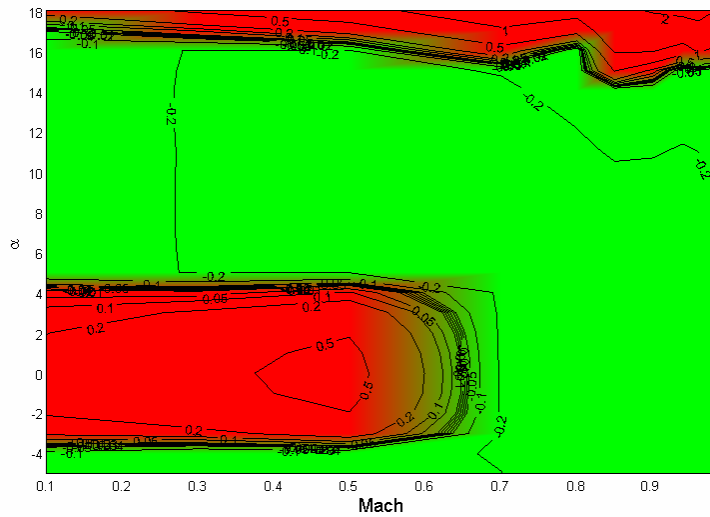
**Fig. II - 17 – Real Part of the Longitudinal Eigenvalues, Short Period
Approximation – Re = 3e6, β = 0°, θ = 30°**
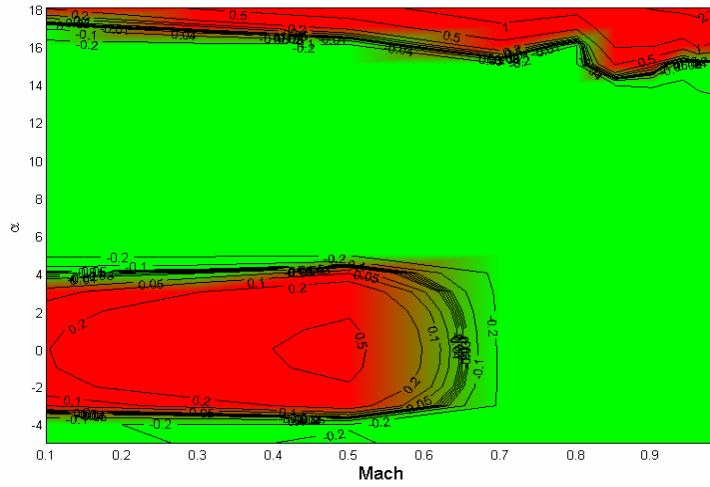
Fig. II - 18 – Real Part of the Longitudinal Eigenvalues, Short Period Approximation – Re = 3e6, β = 0°, θ = 0°
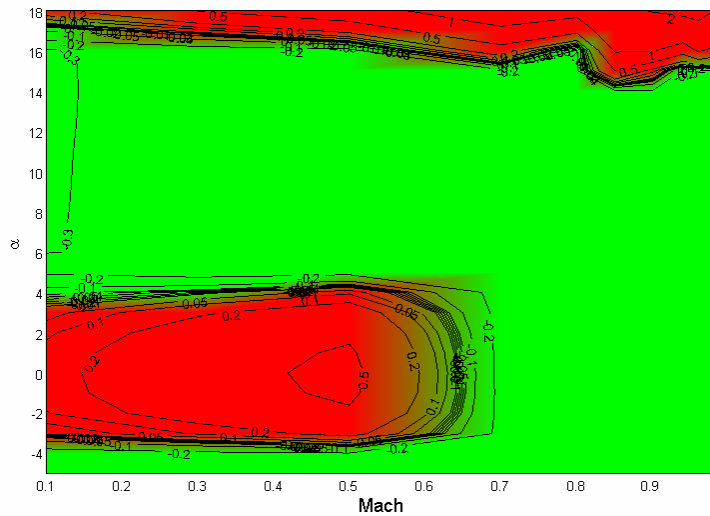
Fig. II - 19 – Real Part of the Longitudinal Eigenvalues, Short Period Approximation – Re = 3e6, β = 0°, θ = -30°
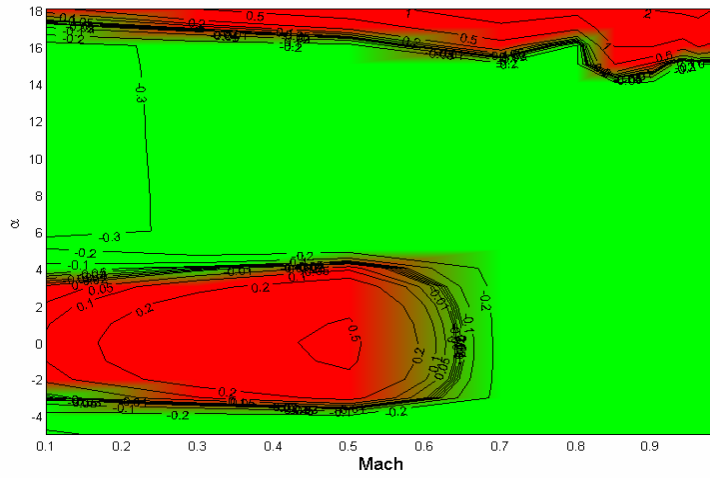
**Fig. II - 20 – Real Part of the Longitudinal Eigenvalues, Short Period
Approximation – Re = 3e6, β = 0°, θ = -60°**
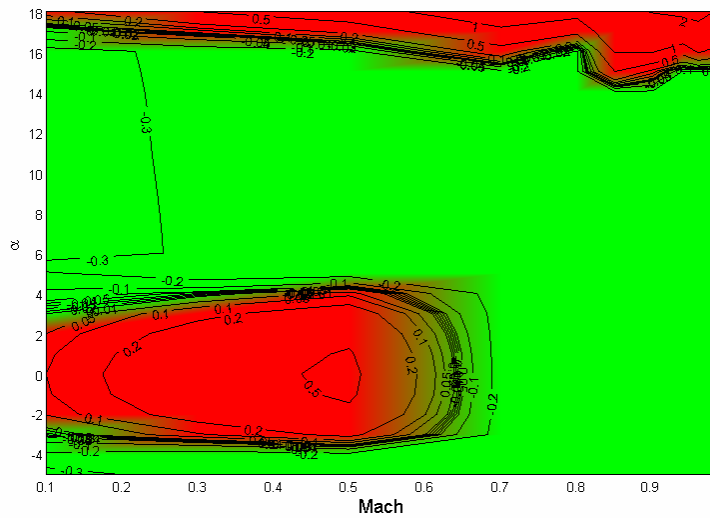
**Fig. II - 21 – Real Part of the Longitudinal Eigenvalues, Short Period
Approximation – Re = 3e6, β = 0°, θ = -89°**

II.2.d.2.2   Lateral-Directional Stability
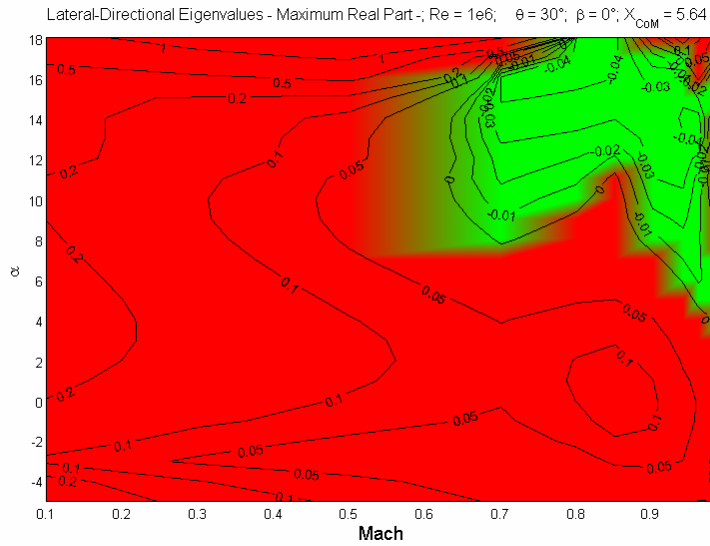
Fig. II - 22 – Real Part of the Lateral-Directional Eigenvalues – Re = 1e6, β = 0°, θ = 30°
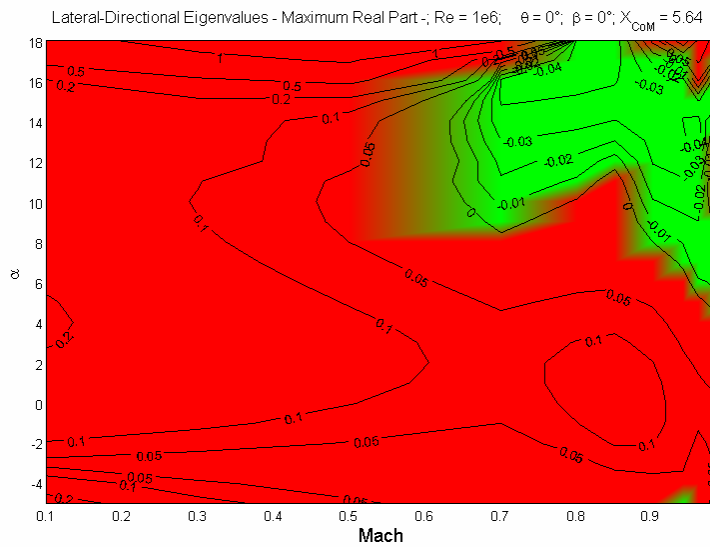
Fig. II - 23 – Real Part of the Lateral-Directional Eigenvalues – Re = 1e6, β = 0°, θ = 0°
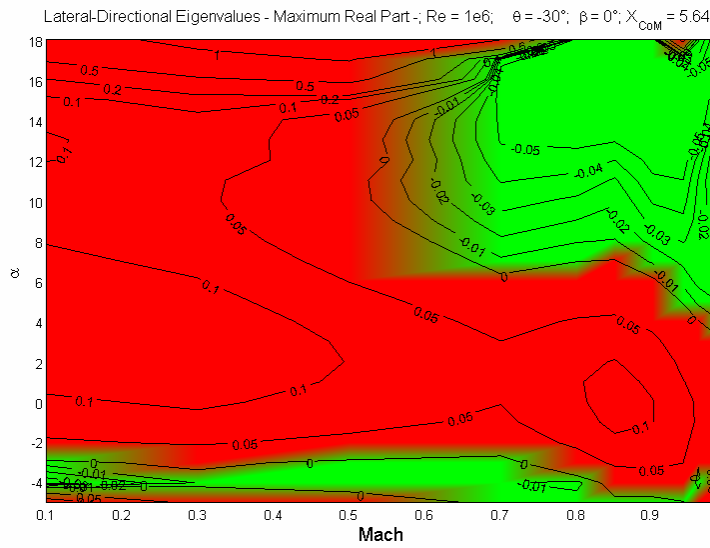
**Fig. II - 24 – Real Part of the Lateral-Directional Eigenvalues – Re = 1e6, β = 0°,
θ = -30°**
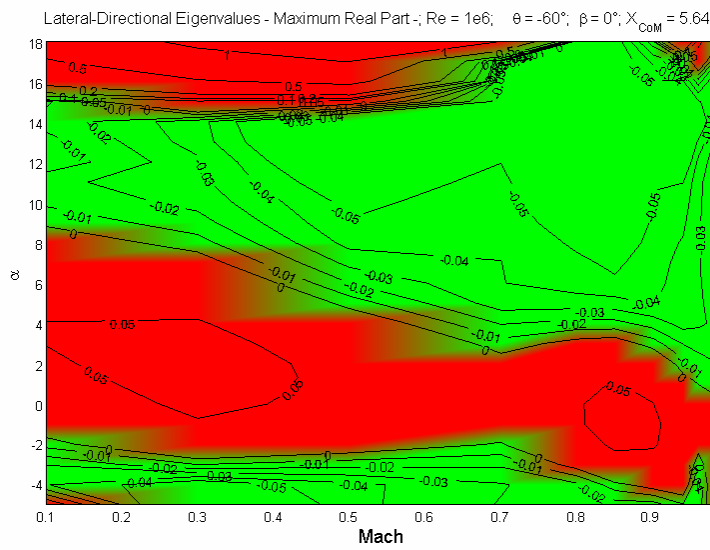
**Fig. II - 25 – Real Part of the Lateral-Directional Eigenvalues – Re = 1e6, β = 0°,
θ = -60°**
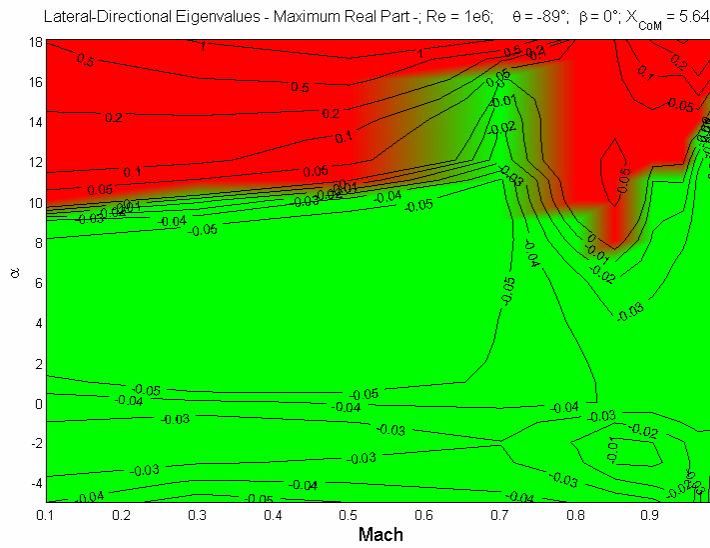
Fig. II - 26 – Real Part of the Lateral-Directional Eigenvalues – Re = 1e6, β = 0°, θ = -89°
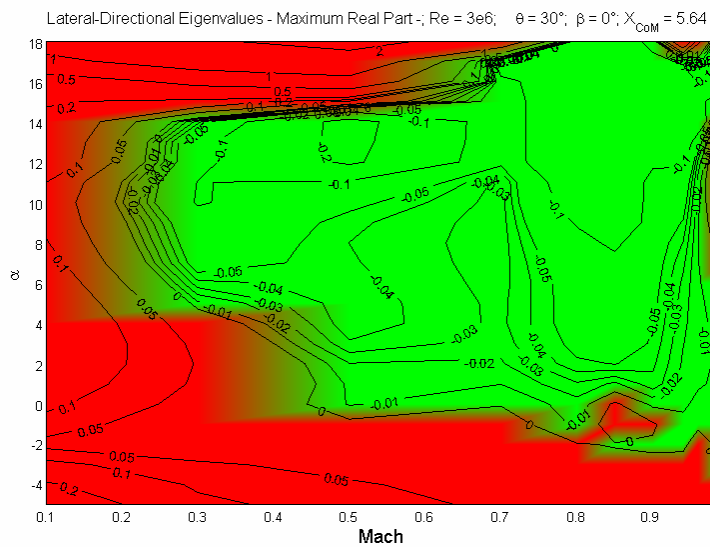
Fig. II - 27 – Real Part of the Lateral-Directional Eigenvalues – Re = 3e6, β = 0°, θ = 30°

**Fig. II - 28 – Real Part of the Lateral-Directional Eigenvalues – Re = 3e6, β = 0°,
θ = 0°**

**Fig. II - 29 – Real Part of the Lateral-Directional Eigenvalues – Re = 3e6, β = 0°,
θ = -30°**
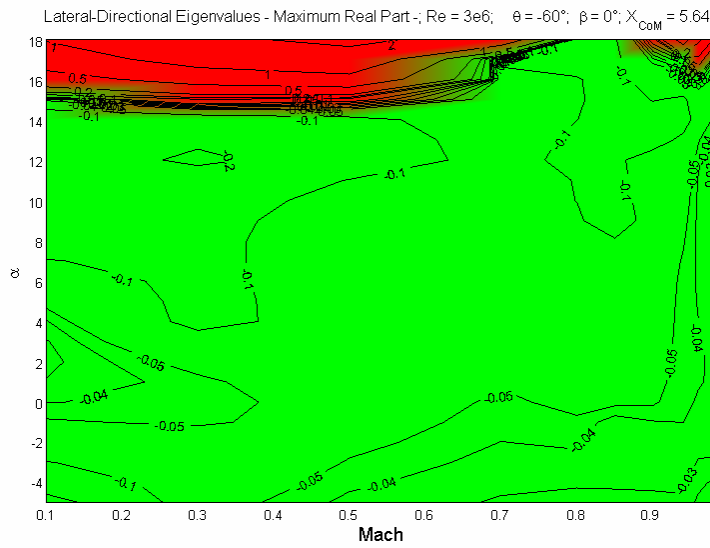
Fig. II - 30 – Real Part of the Lateral-Directional Eigenvalues – Re = 3e6, β = 0°, θ = -60°
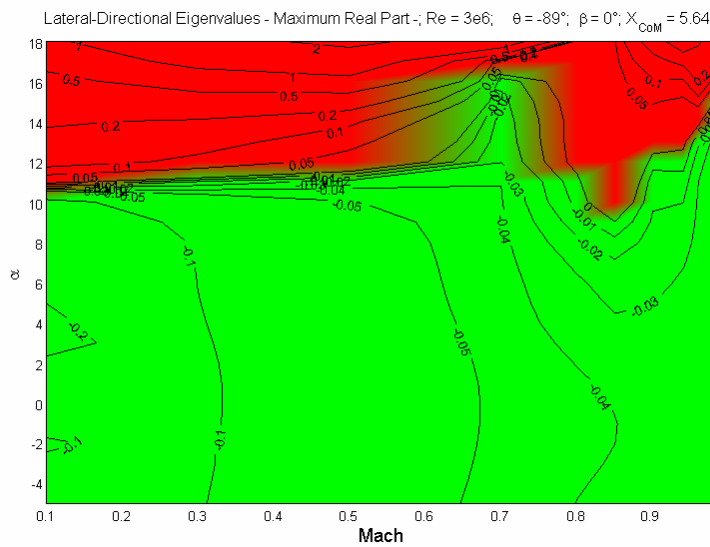
Fig. II - 31 – Real Part of the Lateral-Directional Eigenvalues – Re = 3e6, β = 0°, θ = -89°

II.2.d.3   Effect of Uncertainties

As explained in § II.2.c.3, the effect of uncertainties is evaluated by means of a reference trajectory and two dispersed trajectories.

For each point of these trajectories, an evaluation of the manoeuvrability margin, and of the eigenvalues of the longitudinal (short period) and lateral-directional linearised models, is performed.

The results are presented in this paragraph[29],[30].

II.2.d.3.1   Trimmability and Manoeuvrability

In the following Fig. II - 32 are depicted the Manoeuvrability Margins for the nominal and dispersed trajectories.
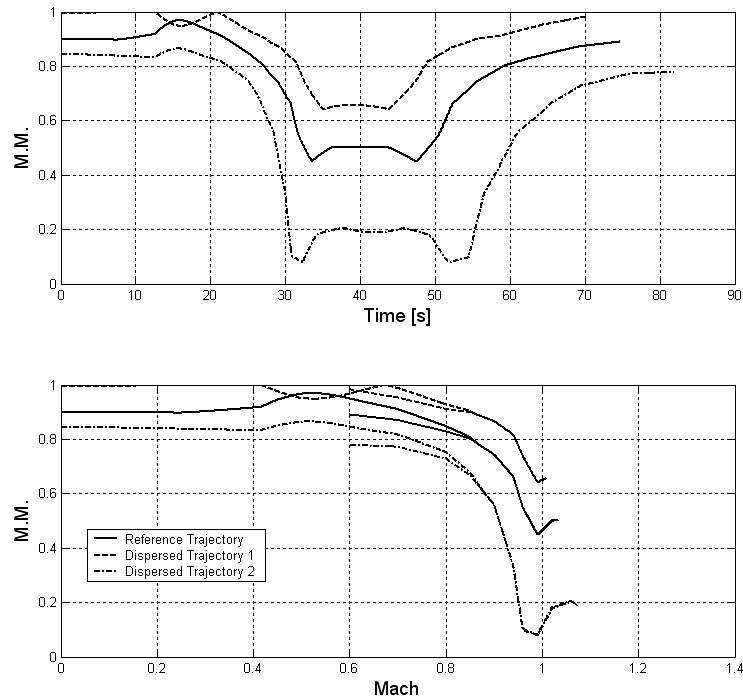
Fig. II - 32 – Manoeuvrability Properties

As already stated in § II.2.c.3, the dispersed trajectories are associated with the best and worse manoeuvrability conditions: it can be seen that the nominal case admits values of the margin up to 0.5, while the effect of decremental uncertainties (Dispersed Trajectory 2), leads to a loss in manoeuvrability. The remaining control power in this case is about 10%.

II.2.d.3.2   Longitudinal Stability

The effect of aerodynamic uncertainties on the longitudinal dynamic stability has been taken into account considering only the influence of the

static derivatives that affect the short period mode, i.e. $C_{L\alpha}$ and $C_{m\alpha}$; they

have been considered both the stabilizing and the destabilizing case:

$$\text{Stabilizing Uncertainties} \Rightarrow \begin{cases} \widetilde{C}_{L\alpha\_UNC} = C_{L\alpha\_NOM} - \Delta C_{L\alpha}^{-} \\ \widetilde{C}_{m\alpha\_UNC} = C_{m\alpha\_NOM} - \Delta C_{m\alpha}^{-} \end{cases}$$

$$\text{Destabilizing Uncertainties} \Rightarrow \begin{cases} \widetilde{C}_{L\alpha\_UNC} = C_{L\alpha\_NOM} + \Delta C_{L\alpha}^{+} \\ \widetilde{C}_{m\alpha\_UNC} = C_{m\alpha\_NOM} + \Delta C_{m\alpha}^{+} \end{cases} \qquad \textbf{(II - 9)}$$

In Fig. II - 33 are depicted the real and imaginary part of the short

period poles of the vehicle vs. the Mach number; are there represented

the reference case and the two most representative cases emerged from

the analyses, the one of Dispersed Trajectory 1, affected by Stabilising

Uncertainties, that is associated with the best stability properties, and the

one of Dispersed Trajectory 2, affected by Destabilising Uncertainties,

that, on the contrary, is associated with the worse stability properties.

Furthermore, Fig. II - 34 shows the short period eigenvalues on the

complex plane, with a continuous line for the nominal trajectory, and a

cyan zone where the poles of the system are located in case of dispersed

trajectories, with and without uncertainties.
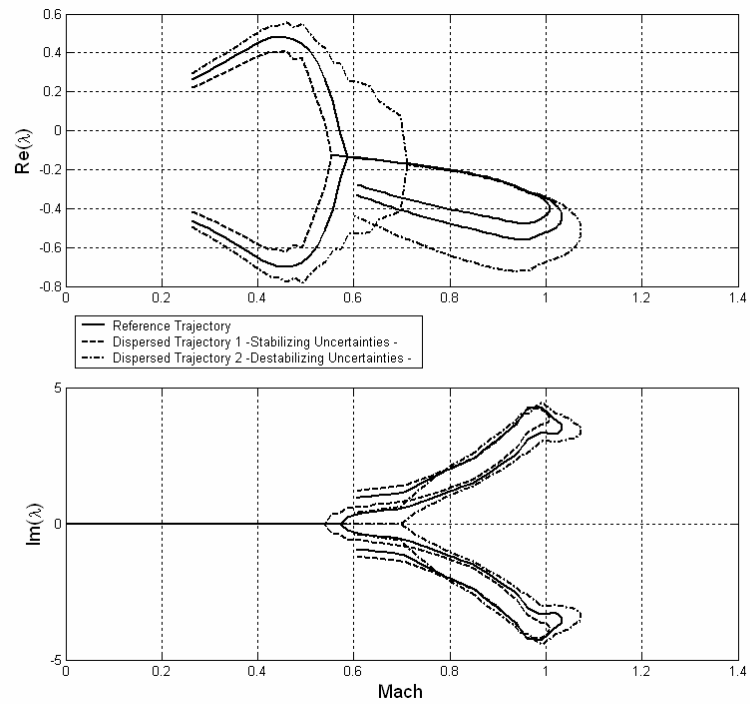
Fig. II - 33 – Real and Imaginary part of the Short Period Eigenvalues, vs. Mach Number
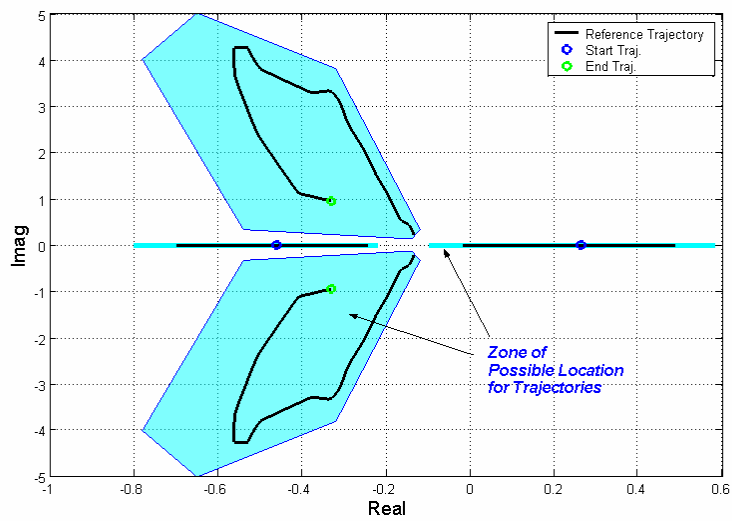
Fig. II - 34 – Short Period Eigenvalues

Frome these figures, it is clearly recognisable an instability in the initial phase of the trajectories; this in accordance with the results of the analyses reported in. the previous paragraph. In fact, in Fig. II - 12 to Fig. II - 16 are evidently reported "red zones" located in correspondence of low α/low M.

II.2.d.3.3   Lateral-Directional Stability

The lateral-directional stability analysis is conducted in nominal and off-nominal flight conditions. In particular, two indicative off-nominal cases are identified by considering extreme conditions, obtained combining the effects of uncertainties about aerodynamic stability derivatives with trajectory dispersion.

Concerning the former, from lateral–directional stability point of view, two contrasting effects occur. Indeed a roll and Dutch roll stability increase can be coupled with a decrease in spiral stability characteristics[32]. Therefore, two opposite aerodynamic derivatives uncertainties vectors are applied, intending to provide the worst stability features in terms of either roll and Dutch roll or spiral modes. These two uncertainties vectors are eventually applied to the previously identified boundary trajectories. Specifically, for each of the two destabilizing

effects, the corresponding uncertainty vector is combined with the two dispersed trajectories, and the worst case between the two is selected.

For the sake of clarity, the stability analyses are separately presented for Dutch roll and roll/spiral modes, limiting the analyses to the available aerodynamic dataset (Mach ≤ 0.99).

A.   *Dutch Roll Stability Analysis*

The most used criterion to predict Dutch roll static stability is the $C_{n\beta dyn}$ positiveness[33]. The $C_{n\beta dyn}$ profile along the nominal trajectory is shown in Fig. II - 35, resulting in an overall positiveness in all the flight conditions.

The expected dispersions, shown by the error bars in Fig. II - 35, include also negative values of $C_{n\beta dyn}$ in low subsonic (Mach < 0.5), higher altitude flight regimes. In this region the static criterion suggests that an open loop instability can occur.
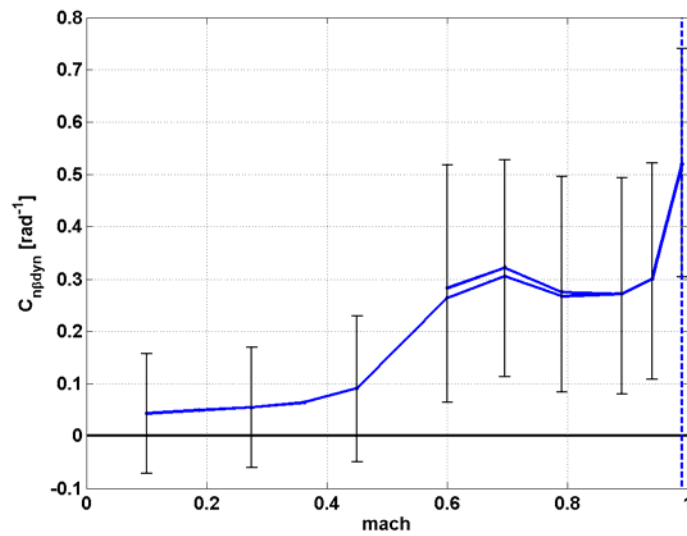
Fig. II - 35 – $C_{n\beta dyn}$ profile in nominal conditions and expected dispersions.

The linear analysis, conducted on both nominal and dispersed conditions has confirmed the indications given by static stability analysis. Indeed, a divergent real pole can be observed in dispersed conditions, as shown in Fig. II - 36. More precisely, Fig. II - 37 collects the real and imaginary eigenvalues components as a function of the Mach number, outlining how the unstable pole can arise in the same region pointed out by the static criterion application.
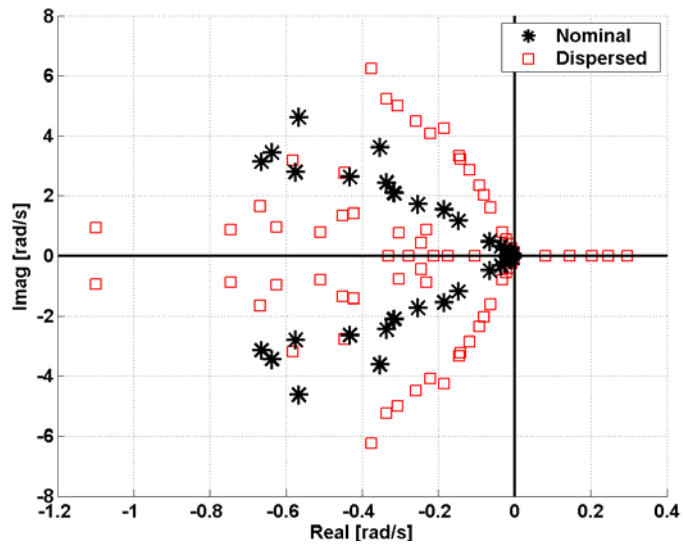
Fig. II - 36 – Dutch roll eigenvalues in nominal and dispersed conditions
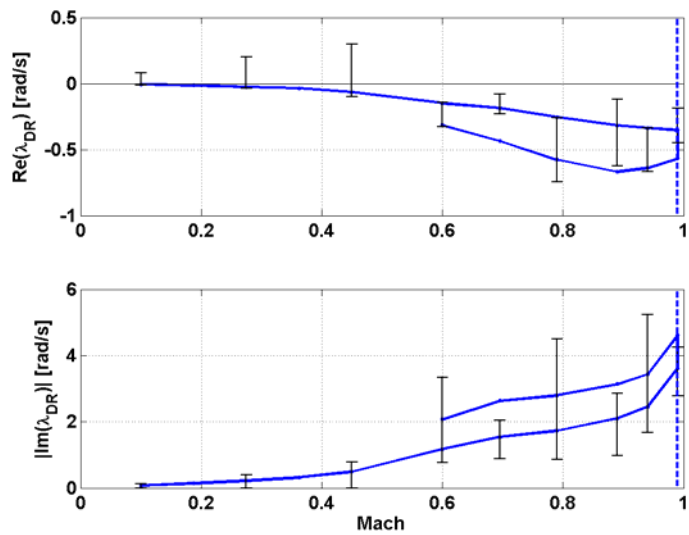
Fig. II - 37 – Dutch roll mode eigenvalues profile w.r.t. Mach number

B.   *Spiral Stability Analysis*

The Lateral Control Departure Parameter (LCDP) negativeness provides an indication of roll departure susceptibility[33],[34],[35]. In the present application case no aileron adverse yawing moment occurs, both in nominal and dispersed conditions. This implies that LCDP negativeness cannot be caused by roll reversal, but only by either directional ($C_{n\beta} < 0$) and/or lateral ($C_{l\beta} > 0$) static instability.

Fig. II - 38 shows the LCDP behavior in nominal and dispersed flight conditions. It can be seen that, except in the initial phase of the mission (up to Mach numbers of about 0.5), in which static instability occurs in dispersed flight conditions, the LCDP is always positive.

However, roll and spiral mode linear analysis results point out that in dispersed conditions, a stable roll mode and an unstable spiral mode take place (Fig. II - 39). Moreover, note that in nominal flight conditions, around Mach numbers of 0.3, the roll and spiral real poles merge to form a single oscillatory mode, usually named lateral phugoid[36], occurring, for instance, in lifting body configurations[37].

Fig. II - 40 shows the spiral and roll eigenvalues versus the Mach number. It can be seen that the observed spiral instability occurs only in dispersed flight conditions for Mach numbers higher than 0.5.

Fig. II - 38 – LCDP in nominal and dispersed flight conditions

Fig. II - 39 – Roll and spiral poles in nominal and dispersed conditions
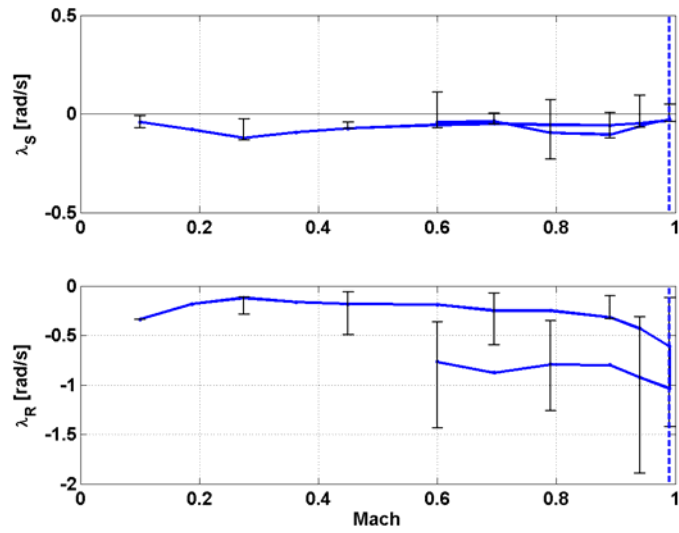
Fig. II - 40 – Roll and spiral eigenvalues in nominal and dispersed flight conditions
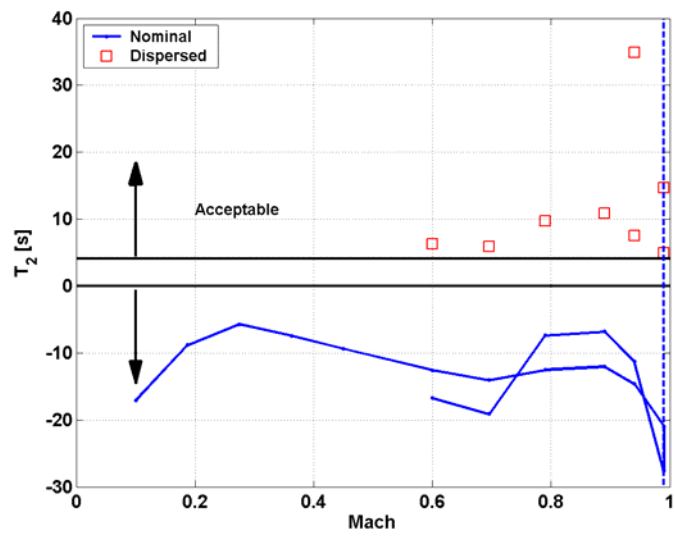
Fig. II - 41 – Spiral mode time to double the amplitude in nominal and dispersed flight conditions

Fig. II - 41 shows the time to double amplitude of the spiral mode in nominal and in unstable dispersed flight conditions as a function of Mach number. In this case, a spiral instability is considered acceptable if, in accordance with the MIL standards[38], the time to double is > 4 s. It can be observed that this requirement is always satisfied.

II.2.e   Conclusions

The FTB_1 vehicle flyability has been the aim of the analyses performed and documented in this paragraph.

Few premises are here pointed out before tracing the final conclusion:

a. The nominal flyability analyses have been performed over a prefixed envelope in the variables (M, α, β, θ, Re, δ_{e_R}, δ_{e_L}, δ_r).

b. A preliminary evaluation of the effect of uncertainties has been performed considering the reference trajectory and two dispersed trajectories.

This stated, summarising the conclusions of the analyses it is possible to affirm that:

1. The present vehicle configuration, for the present nominal C.o.M. position, shows highly favourable behaviour with respect to trimmability, with

manoeuvrability margin that results greater than 40% all along the reference trajectory.

2. In the same condition the vehicle longitudinal stability results highly critical, with zones of instability that can be crossed by the reference trajectory (as specified in § II.2.d.3.2).

3. Lateral-directional stability is verified in wide regions of the analysed flight envelope, but instabilities have been founded, in particular for flight conditions characterised by $\theta \geq 0°$. Further investigations shows that these instabilities can be either oscillatory (dutch roll, low α) or not ("spiral", high α).

4. The effect of uncertainties does not modify the structure of the longitudinal dynamics of the vehicle, but can lead to a further reduction in the stability properties; about the lateral-directional behaviour, it can be strongly affected by uncertainties, with a structure of the modes of evolution that can change with reference to the nominal case.

II.3 Monte Carlo Analysis

II.3.a   Introduction

The scope of this analysis is the evaluation of some well-defined metrics, aimed to verify the fulfilment of the mission and system requirements by the vehicle, during the execution of its flight, in presence of statistically characterised random disturbances, that can be of various nature: aerodynamic or inertial uncertainties, environmental disturbances, errors on the sensors[39],[40],[41],[42].

Executing a high number of mission simulations it will be possible to completely investigate the behaviour of the vehicle. It is here considered a number of simulations $N_{SIM} = 3000$.

II.3.b   Description of the Model and of the Applied Uncertainties

II.3.b.1   Considered Model

The model used in the analysis is shown in Fig. II - 42; it has been developed entirely in a Matlab/Simulink® environment, and consist of a series of blocks describing:

► The flight dynamics of the USV-FTB_1 vehicle;

► The model of the sensors installed on board;

► The model of the Guidance and Control Laws installed on board;

► The model of the actuators installed on board.

Further details about all this models can be found in [43],[44].

In order to allow the execution of a great number of simulations, the developed model has been compiled using Real Time Workshop/Stateflow Coder®, using an appropriate target, generating a .exe file. This procedure significantly reduces the time of execution for a single simulation.
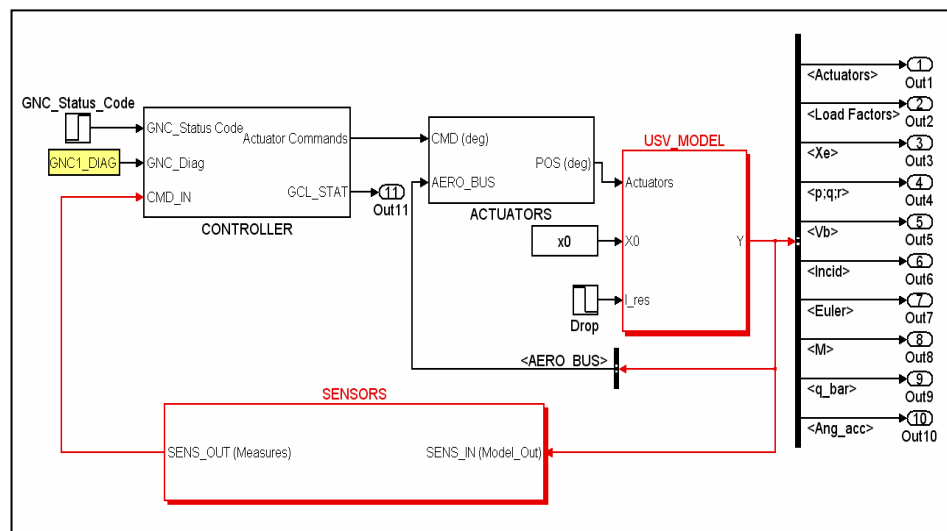
Fig. II - 42 – MC Analysis Simulation Model

II.3.b.2   Aerodynamic Uncertainties

The uncertainty coefficients are supposed to be distributed as normal variables, with zero mean and variances defined in Appendix 3.

In addition to the Mach values indicated in the tables of the Appendix, the uncertainties are considered also in correspondence of M = 0.96, 1.02, 1.015, performing a linear interpolation between the next values.

The uncertainty profile is built executing a single random extraction for Mach from 0.1 to 0.7, in such a way that the nominal bound (except for a scaling operation) is followed. After M = 0.7, a series of uncorrelated extractions is realised. An example of uncertainty profile ($\Delta C_{m\alpha}$) is shown in the following figure:
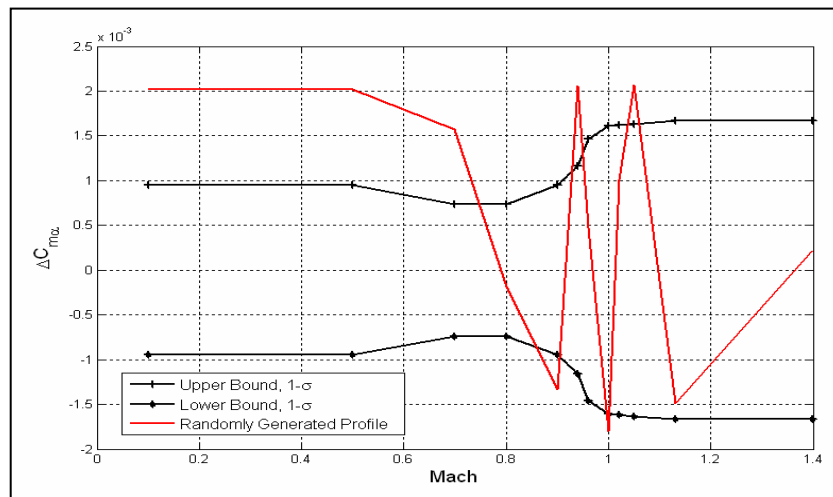
Fig. II - 43 – Example of Uncertainty Profile

II.3.b.3   Inertial Uncertainties

The Centre of Mass of the vehicle is supposed to be located in the nominal position, described in § II.1; on this one, are applied:

> ► A positioning uncertainties described by:
>
>> ○ $\Delta X_{CoM} = \pm 4E\text{-}2$ m
>>
>> ○ $\Delta Y_{CoM} = \pm 1E\text{-}2$ m
>>
>> ○ $\Delta Z_{CoM} = \pm 1E\text{-}2$ m
>
> ► The maximum uncertainty associable with the measurement process:
>
>> ○ $\Delta X_{CoM} = \pm 5.2E\text{-}3$ m
>>
>> ○ $\Delta Y_{CoM} = \pm 0.3E\text{-}3$ m
>>
>> ○ $\Delta Z_{CoM} = \pm 10.3E\text{-}3$ m

For both it is supposed a uniform distribution.

About the inertia matrix, values of expectable uncertainties on it are not available, and so, a uniformly distributed uncertainty limited in the range $\pm$ 10% has been applied to all its elements.

II.3.b.4   Environmental Uncertainties

The effects of wind and turbulence have been taken into account as environmental disturbances; moreover, the launch site atmospheric characteristics have been analysed and considered.

About turbulence, for it a uniform distribution of the admissible probability of exceedance, from 10^{-1} to 10^{-6} has been considered.

The wind gust intensity has been calculated as dependant from the turbulence intensity, except for the case of severe wind gust, as described in [28], [43]. The probability of occurrence of severe wind gust is considered to be the same of the one of normal wind gust. For gust length and gust application time, a uniform distribution of the values: [80; 90; 100; 110; 120] m and [10; 20; 30; 40; 50; 60; 70; 80; 90; 100] s has been considered. The wind gust is always applied on all the three axis of the NED reference frame (see Appendix 1).

The Perdasdefogu launch environment has been characterised by means of local soundings in terms of wind (intensity and direction), and atmospheric characteristics (pressure and temperature). The reference period considered consists in the months of January and December, for

both 2002 and 2003, and all the soundings are supposed to have the ame

probability of occurrence.

II.3.b.5   Initial State Uncertainties

The nominal state foreseen for the FTB-1 vehicle at the beginning of

the mission is the following:

Initial Altitude	h_0	20	km
Initial Attitude	$[\phi, \theta, \psi]_0$	[0, -90, 0]	deg
Initial Velocity *(in a NED reference frame)*	$[V_N, V_E, V_D]_0$	[0, 0, 30]	m/s
Initial Angular Rates	$[p, q, r]_0$	[0, 0, 0]	deg/s

Table II - 6– Nominal Initial State for the FTB-1 Vehicle

The initial velocity of 30 m/s is due to the lack of aerodynamic data

below Mach = 0.1.

This state is perturbed considering an error on the initial altitude and on

the initial heading; it is so considered:

> ► h_0 uniformly distributed in the interval [19, 21] km

> ► ψ_0 uniformly distributed in the interval [0, 180] deg

It is also considered the effect of the wind velocity on the initial one.

II.3.b.5   Sensors Uncertainties

All the modelled sensors are affected by random disturbances characterised thanks to their data sheets or after an experimental investigation[44].

As an example, the bias characterising the Inertial Navigation Sensors mounted on board are modelled as normal variables, with zero mean and variances:

► $\sigma_{gyros} = 3/3600$ °/s;

► $\sigma_{accelerometers} = 1.5E\text{-}3$ g.

II.3.c   Evaluation Metrics Considered

The mission success rate is evaluated by means of several metrics, oriented either to the safety and to the performance aspects.

II.3.c.1   Safety Metrics

The safety metric adopted defines the Safety Success Rate as the percentage of the simulations that are such to respect the imposed limits on the load factors and on the pitch angular velocity/ acceleration[28]:

Parameter		Max. Value	Min. Value
n_x		1.5	-1
n_y		3	-3
n_z		3	-1
Pitch Angular Velocity	[°/s]	26	/
Pitch Angular Acceleration	[°/s^2]	162	/

Table II - 7 – Safety Metrics Limits

II.3.c.2   Mission Execution Metrics

The mission execution metric adopted defines the Mission Execution Success Rate as the percentage of the simulations satisfying the safety metrics that are such to respect the imposed limits on the tracking precision of angle of attack, angle of sideslip and roll angle. Moreover, a requirement is imposed also on the ground track of the trajectory flown:

Parameter		Max. RMS Error	Max Value
Angle of Attack α	[°]	1	/
Angle of Sideslip β	[°]	1	/
Roll angle ϕ	[°]	3	/
Ground Track – *end of flight phase* –	[km]	/	30
Ground Track – *splashdown* –	[km]	/	52

Table II - 8 – Mission Execution Metrics Limits

About the Tracking precision, it has to be considered with respect to he reference values, that are:

► 7° for the Angle of Attack α;

► 0° for the Angle of Sideslip β;

► 0° for the Roll Angle ϕ.

II.3.d   Analysis of the Results

In the following, the trajectories resulting from the set of simulations are evaluated separating two cases, identified thanks to the existing limits on the recovery system. In fact two separate curves, in the Mach-Altitude plane, describe two forbidden zones in which the safe opening of the parachute is not possible, because the load factor on itself exceed, respectively, the value of 4.5 or 5.6 g (see also § I.4). The situation is shown in Fig. II - 44; the forbidden zones ore located below the curves.
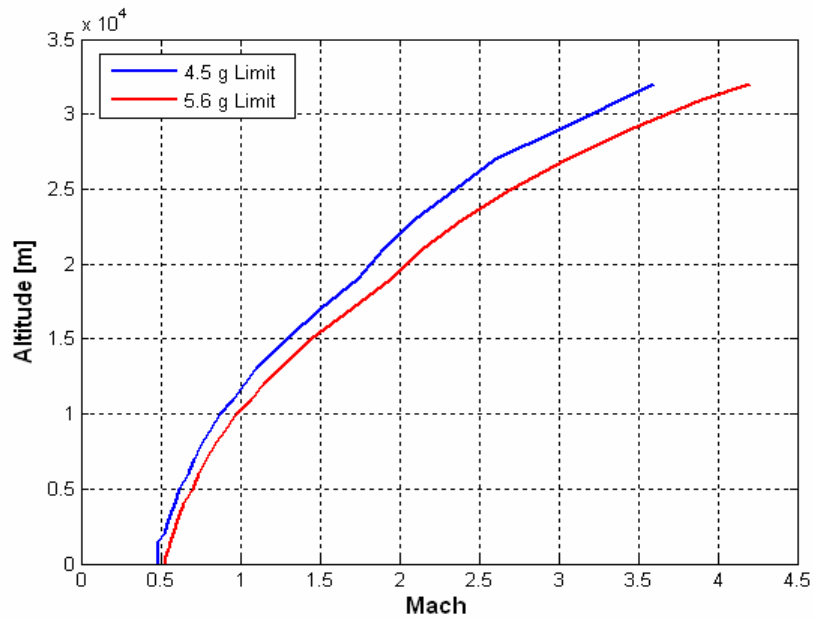
Fig. II - 44 – Parachute Opening Limits

Thus, the cases in which the parachute limit at 4.5 g is crossed will be considered separately from the ones in which the limit at 5.6 g is crossed. In both cases, a simulation is considered satisfactory for the analysed metric if the imposed requirement are fulfilled before the crossing of the limit. It is so assumed that the recovery system will activate at the crossing instant, starting the parachuted phase.

In the evaluation of the safety metric here reported, it is considered as admissible the case in which the limits indicated in Table II - 7 are exceeded, but the time of exceedance must be ≤ 1 s, and the values of the considered parameters must be in any case ≤ 1.5 times the limits indicated in the same Table.

In the plot of the trajectories endpoints, (Fig. II - 51, Fig. II - 57), the blue diamond represent the origin of the trajectory, the red crosses the points in which the considered parachute limit is crossed, and the black stars the points in which it is reached the terminal condition that is univocally identified as:

► $M = 0.6$ AND time_of_flight > 30 s.

II.3.d.1   4.5 g Parachute Limit Crossed

Fig. II - 45 – Altitude vs. Mach

Fig. II - 46 – Normal Load Factor

Fig. II - 47 – Anlgle of Attack
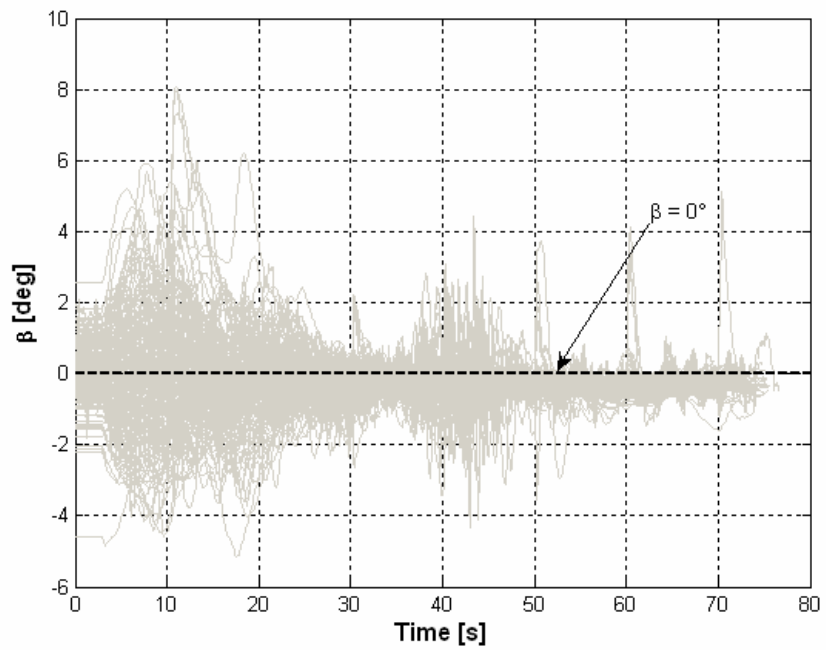
Fig. II - 48 – Angle of Sideslip
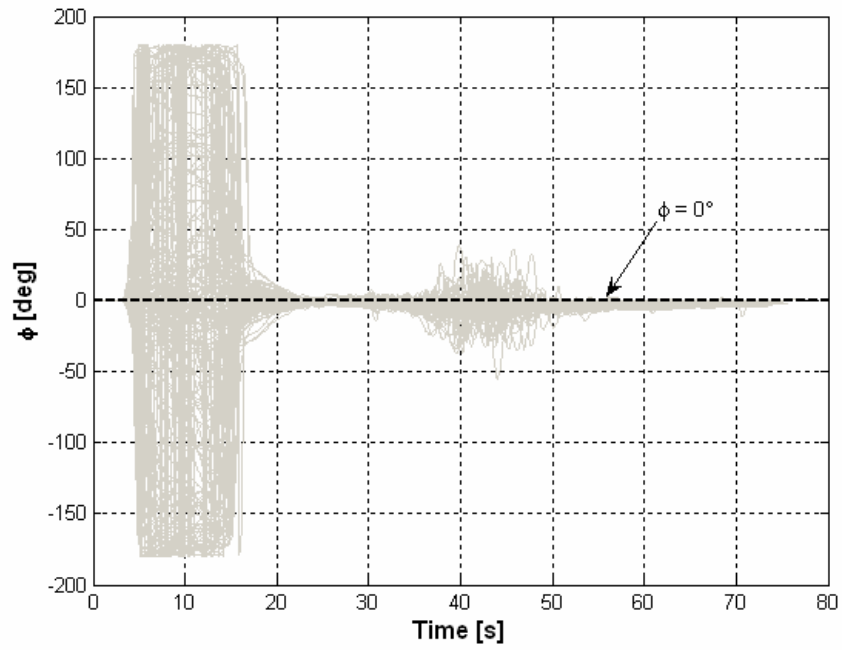
Fig. II - 49 – Roll Angle
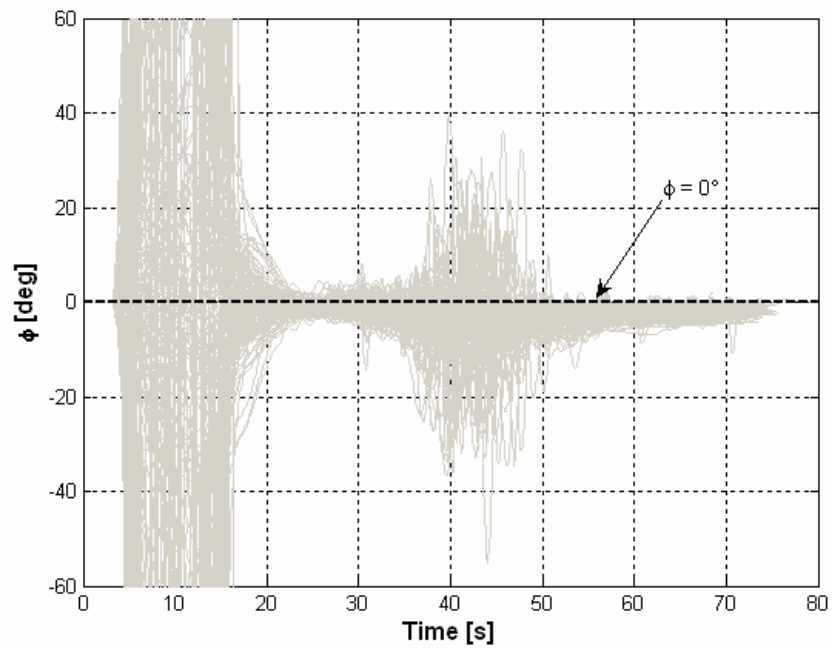
Fig. II - 50 – Roll Angle (Zoom)
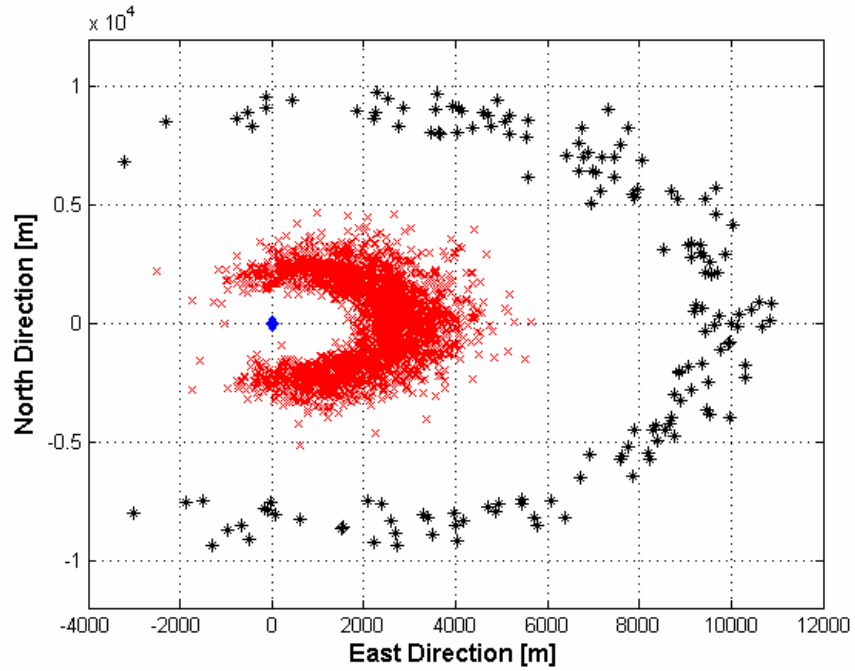
Fig. II - 51 – Trajectory Endpoints

In this case safety and mission execution metrics lead to the following success rates:

> ► Safety Success Rate = 94.93%
>
> ► Mission Execution Success Rate = 3.55%.
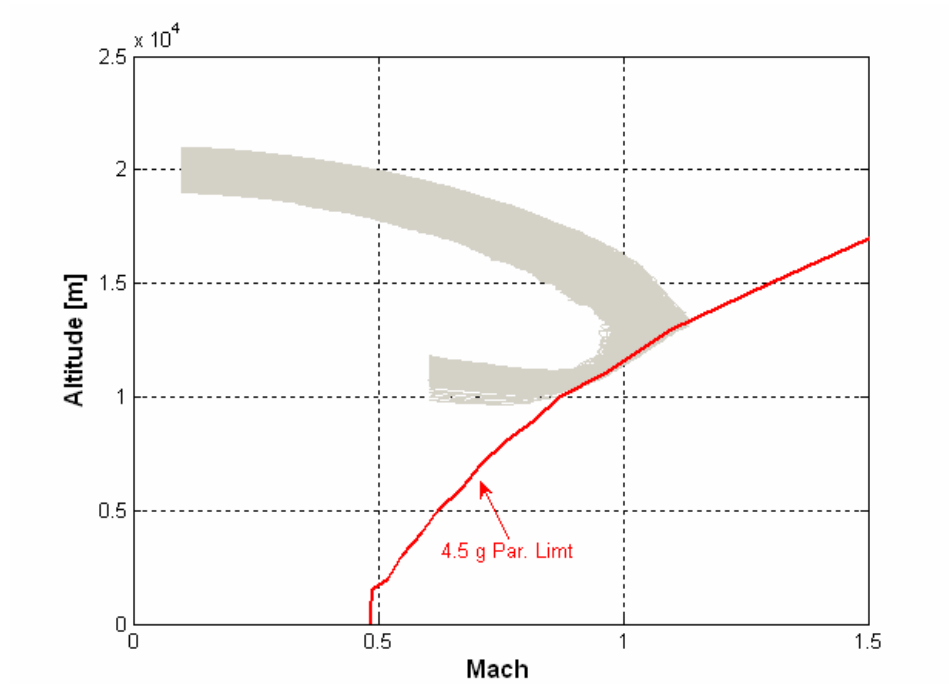
II.3.d.2   5.6 g Parachute Limit Crossed
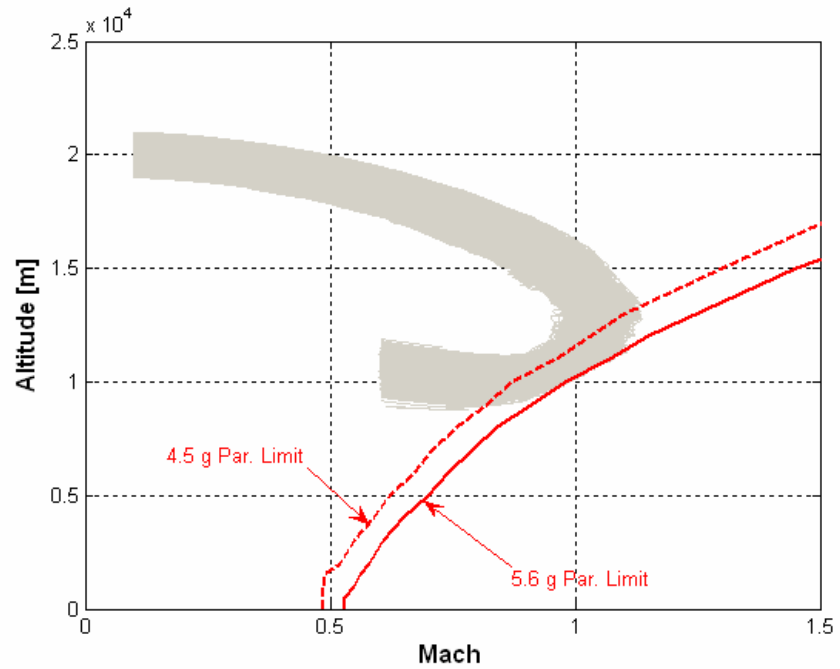
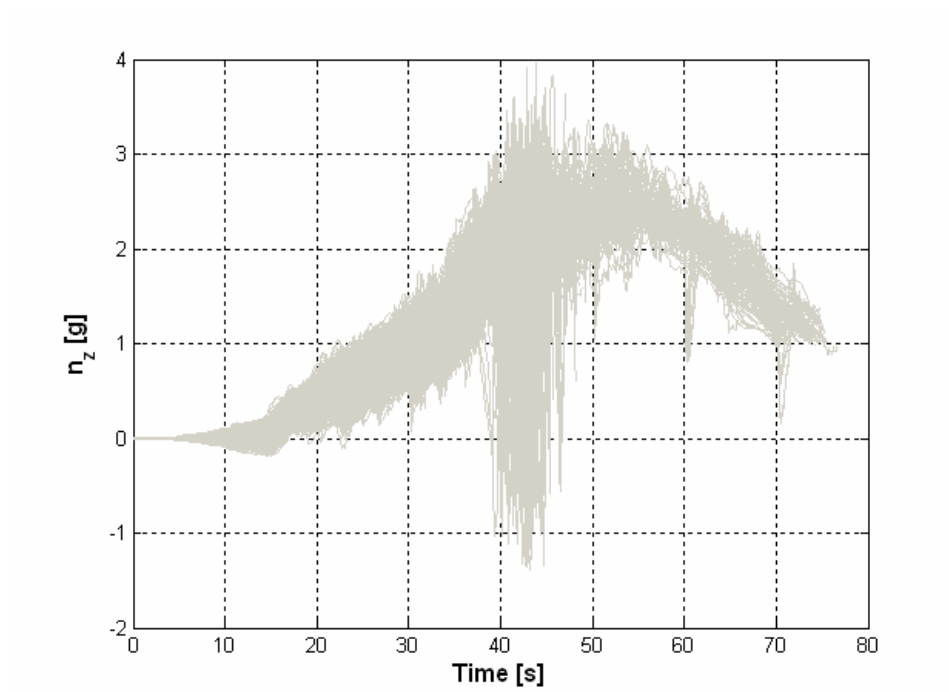**Fig. II - 52 – Alitude vs. Mach**
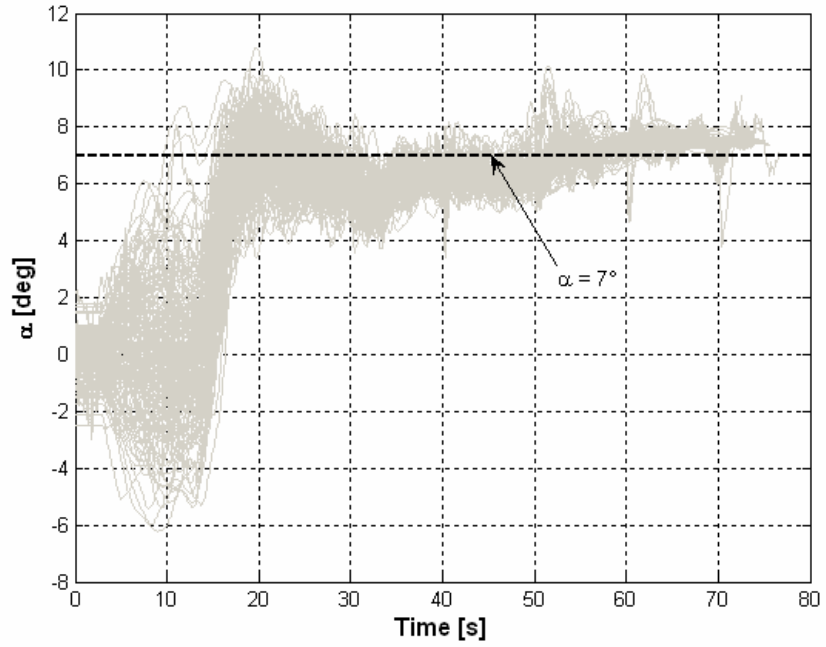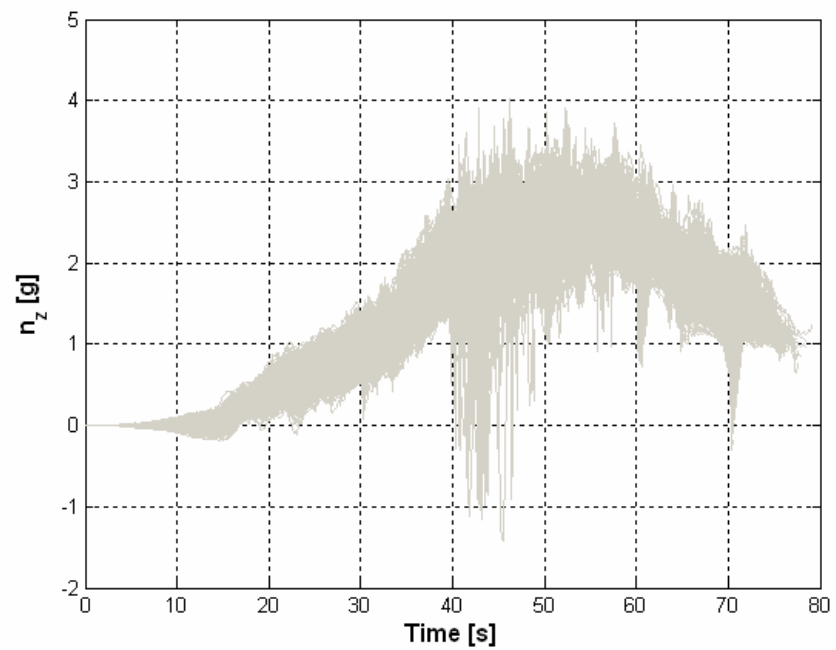

Fig. II - 53 – Normal Load Factor
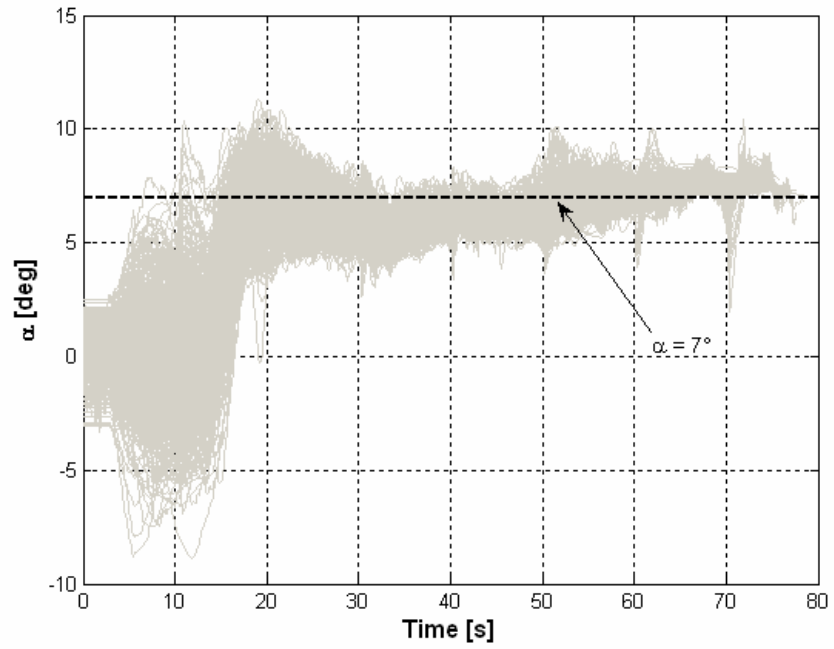
Fig. II - 54 – Angle of Attack
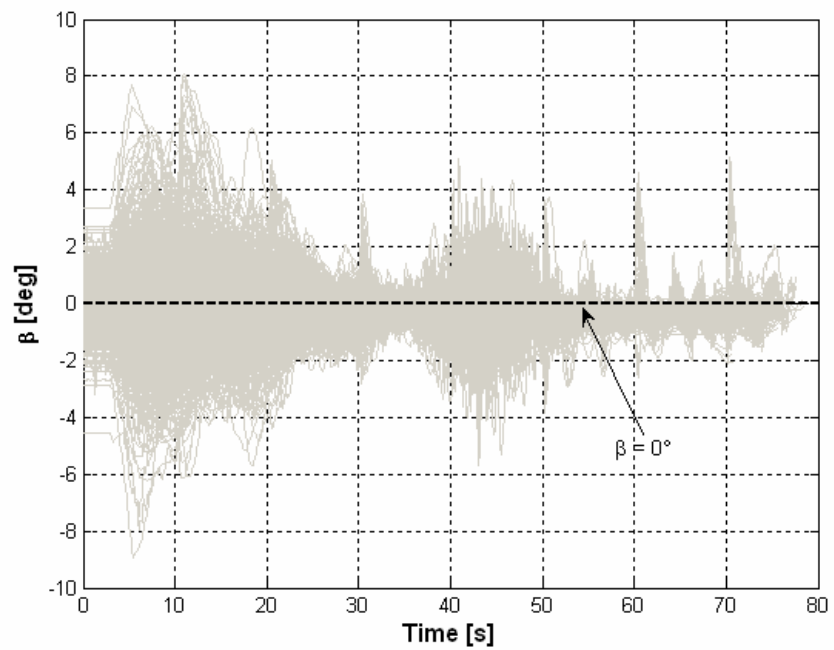
Fig. II - 55 – Angle of Sideslip
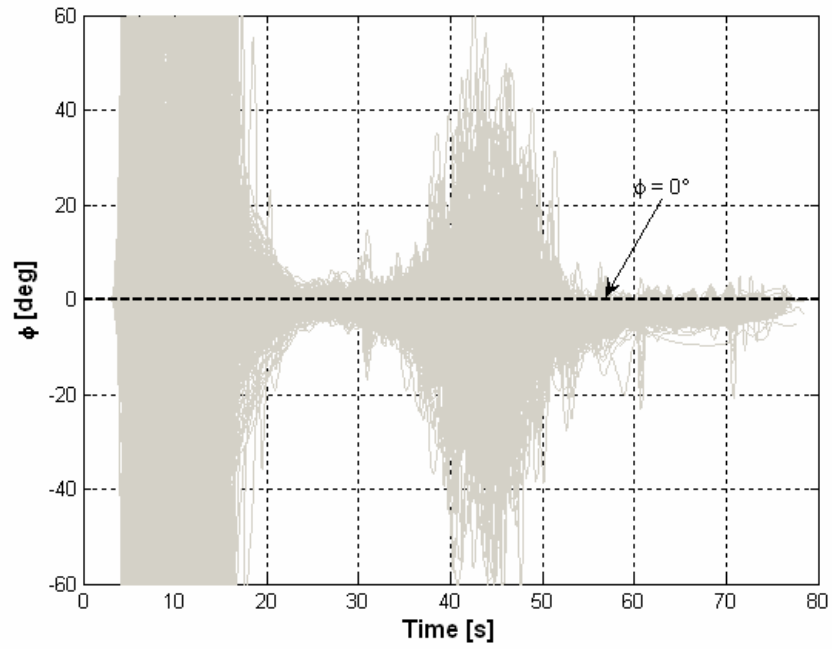
Fig. II - 56 – Roll Angle
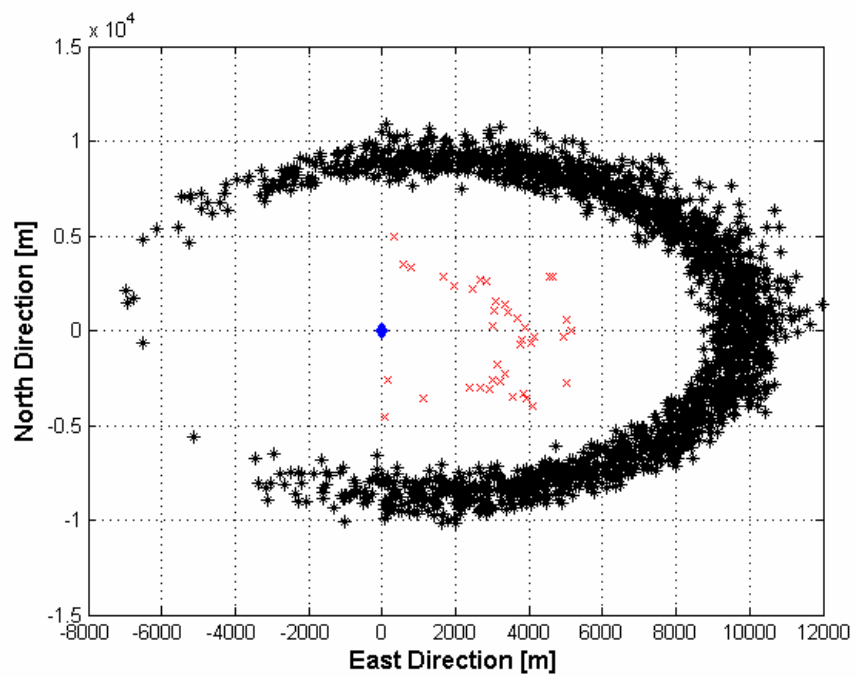
Fig. II - 57 – Trajectory Endpoints

In this case safety and mission execution metrics lead to the following success rates:

► Safety Success Rate = 71.53 %;

► Mission Execution Success Rate = 17.84 %.

II.3.e   Conclusions

As it can be seen from the results indicated in this paragraph, the vehicle shows an acceptable safety success rate only if the 4.5 g parachute limit is considered as constraining. This can be justified considering that the nominal (i.e. with no uncertainties applied) trajectory flown by the vehicle is characterised by an altitude-Mach diagram and an angle of attack profile that are shown in Fig. II - 58 and Fig. II - 59. As it can be seen they are different from the reference plots, shown in Fig. II - 4 and Fig. II - 5; it should be remarked that the latter are characteristic of the point-of mass model (II - 1), not of the six degree-of freedom complete model depicted in Fig. II - 42, much more complex. Moreover, in Fig. II - 60 is shown the normal load factor nominal profile.
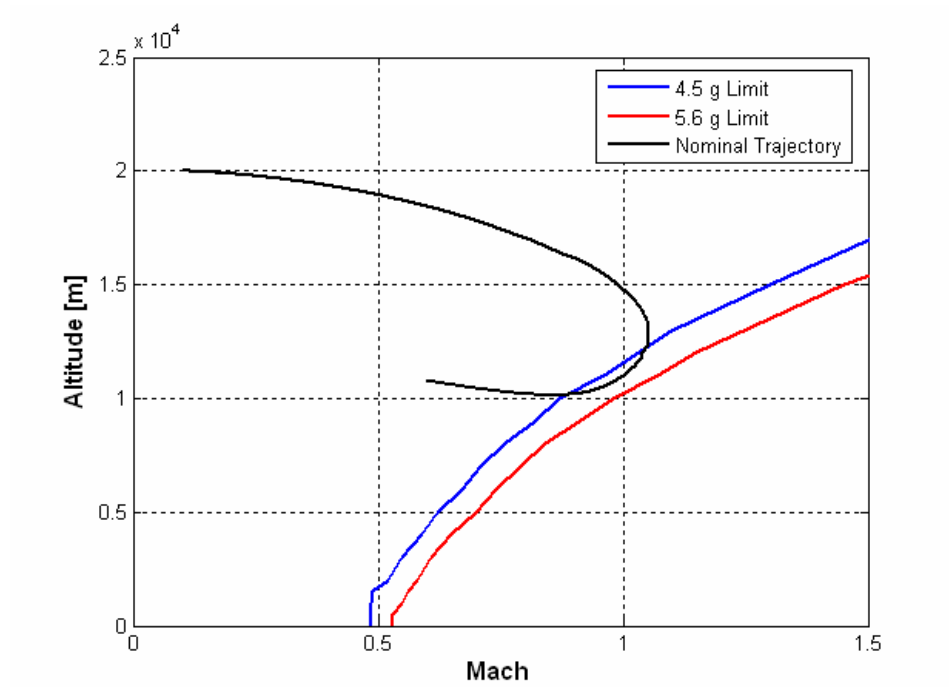
Fig. II - 58 – Altitude vs. Mach – Nominal Profile
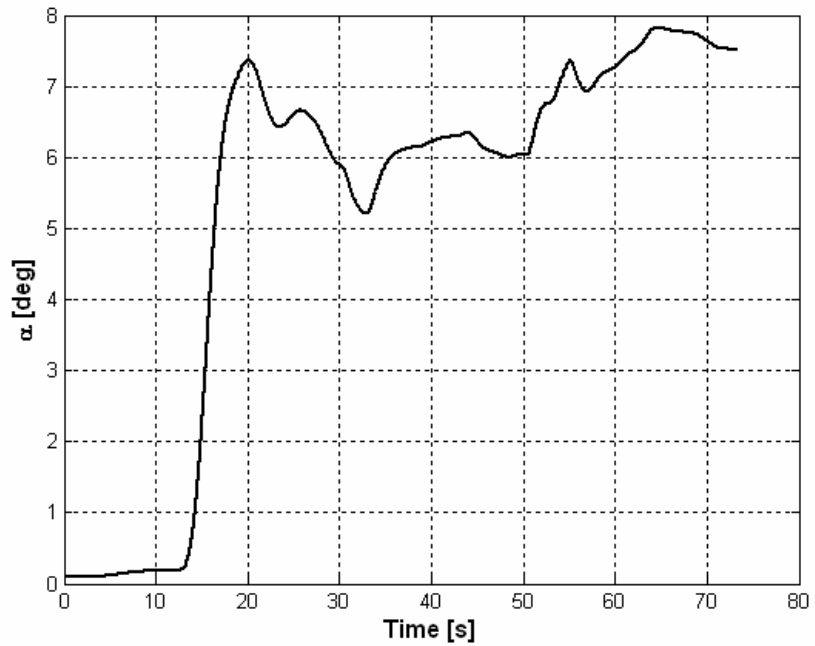
Fig. II - 59 – Angle of Attack – Nominal Profile
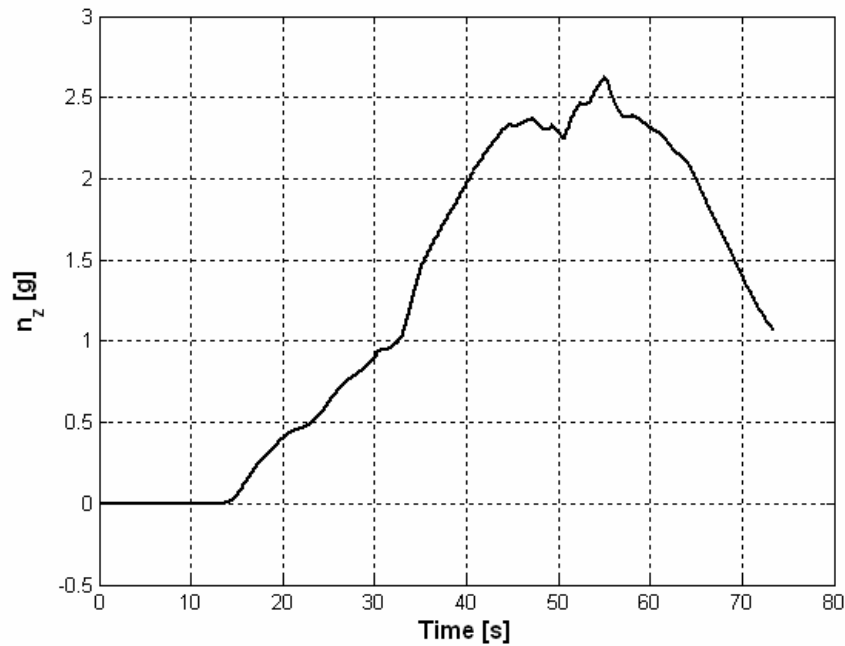
Fig. II - 60 – Normal Load Factor – Nominal Profile

As it can be seen, all the parameters are already close to their limits in the nominal case: the Altitude-Mach plot cross the 4.5 g limit and the maximum normal load factor is >2.5; this last consideration leads to a high sensitivity to the load factor limits when the trajectories are constrained within the 5.6 g limit. By the other hand, considering the 4.5 g limit, the angle of attack nominal profile (that in this case ends after about 45 s) shows a constant tracking error, that gives as consequence the poor value for the performance success rate in this case.

Finally, one word can be spent on the roll angle profile depicted in Fig. II - 49; the values of about 180° that can be seen at the beginning of the

trajectory are a consequence of the fact that the initial pitch angle is $\approx$ 90°, so the situation is next to a singularity in the kinematical equations of motion (see Appendix 2). Actually, the indicated values for [ϕ, θ, ψ] in any case correctly describe the attitude of the vehicle.

Chapter III

Gravity Level Analysis

III.1 Introduction

The aim of this chapter is the analysis and the complete characterisation of the gravitational environment proper of the USV-FTB_1 vehicle, performing the DTFT mission..

It could be objected, from an analysis of the results presented in the previous chapter, that the values of the load factors that can be reached during the mission are clearly higher than the ones characterising a microgravity condition.

In this chapter it will be shown how, despite the fact that the DTFT mission is not a parabolic flight, and, in general, it has not, among its objectives, the realisation of microgravitational conditions, it is possible to identify a phase of the trajectory that could be interesting for this purpose.

III.2 Methodology and Tools

In order to evaluate the microgravity level inherent to the USV-FTB_1 vehicle performing the DTFT mission, the following procedure has been developed and followed:

► First of all, a three-dimensional grid of points, with coordinates expressed in the body reference frame, will be defined. These points will be the ones where the gravity level will be analysed; for a generic point p the situation depicted in Fig. III - 1 can be considered:
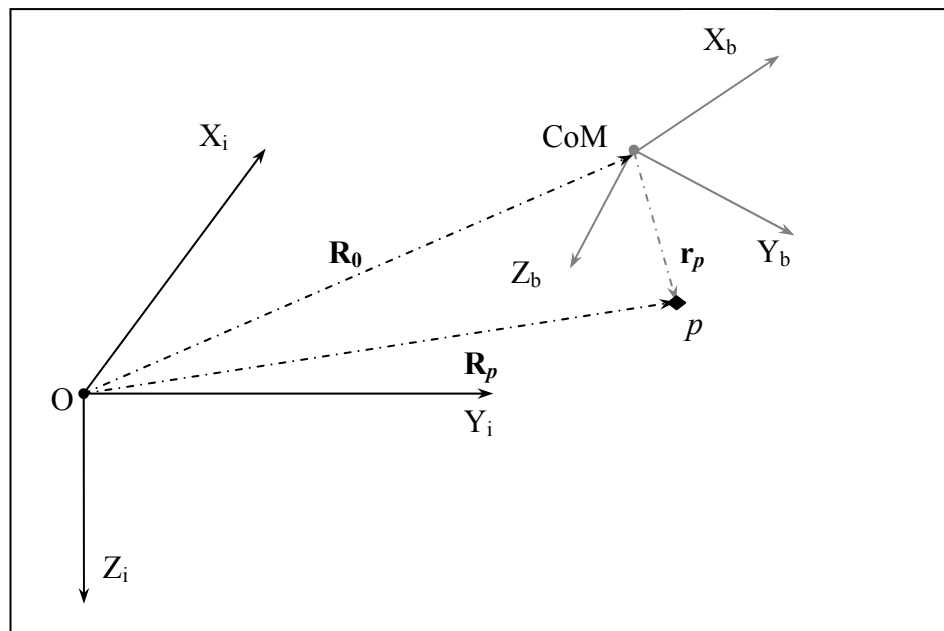
Fig. III - 1 – Generic Point Representation

where:

[X_i, Y_i, Z_i]   is the triad defining the Inertial Reference Frame
[IRF];

[X_b, Y_b, Z_b]   is the triad defining the Body Reference Frame
[BRF];

R_0   is the vector defining the position of the origin of
the BRF ($\equiv$ with the Centre of Mass of the vehicle),
with reference to the IRF;

R_p   is the vector defining the position of the p-th
analysed point, with reference to he IRF;

r_p   is the vector defining the position of the p-th
analysed point, with reference to he BRF

It is clearly noticeable that:

$$\mathbf{R}_p = \mathbf{R}_0 + \mathbf{r}_p \qquad \textbf{(III - 1)}$$

► The acceleration in the generic p-th point previously defined can
be calculated using the following equation:

$$\ddot{\mathbf{R}}_p = \ddot{\mathbf{R}}_0 + \left[\ddot{\mathbf{r}}_p\right]_B + 2\,\boldsymbol{\omega}\times\left[\dot{\mathbf{r}}_p\right]_B + \left[\dot{\boldsymbol{\omega}}\right]_B \times \mathbf{r}_p + \boldsymbol{\omega}\times\left(\boldsymbol{\omega}\times\mathbf{r}_p\right) \qquad \textbf{(III - 2)}$$

where :

$\ddot{\mathbf{R}}_p$	is the acceleration in the p-th point, with reference to the IRF;
$\ddot{\mathbf{R}}_0$	is the acceleration of the origin of the BRF, with reference to the IRF;
$[\ddot{\mathbf{r}}_p]_B$	is the acceleration of the p-th point, with reference to the BRF;
$\boldsymbol{\omega}$	is the angular velocity of the BRF with reference to the IRF;
$[\dot{\mathbf{r}}_p]_B$	is the velocity of the p-th point, with reference to the BRF;
$2\,\boldsymbol{\omega} \times [\dot{\mathbf{r}}_p]_B$	is the Coriolis acceleration;
$[\dot{\boldsymbol{\omega}}]_B$	is the angular acceleration of the BRF, with reference to the IRF;
$[\dot{\boldsymbol{\omega}}]_B \times \mathbf{r}_p$	is the linear acceleration of the p-th point, due to modifications of ω;
$\boldsymbol{\omega} \times (\boldsymbol{\omega} \times \mathbf{r}_p)$	is the centripetal acceleration in the p-th point.

The Equation (III - 2) can be written in any reference frame; in the following it will be evaluated in the BRF.

► The nominal trajectory will subsequently be analysed; for each point of the analysis grid, the acceleration will be calculated, by means of Eq. (III - 2).

► The same procedure will be repeated considering a family of dispersed trajectories available after the Monte Carlo analysis described n the previous chapter.

III.3 Analysis of the Results

The points composing the grid to be analysed are defined by the following coordinates, in the BRF:

$x_p \in$ [-2, -1, 0, 1, 2, 3, 4]

$y_p \in$ [-1, 0, 1]

$z_p \in$ [-1, 0, 1]

All the coordinates are expressed in meters; the situation is depicted in Fig. III - 2.

It should be noted that, being this grid just an artifice to investigate the modification in the measured gravity level as far as the analysed point moves far from the CoM of the vehicle, also points actually not included in the FTB_1 body can be considered.
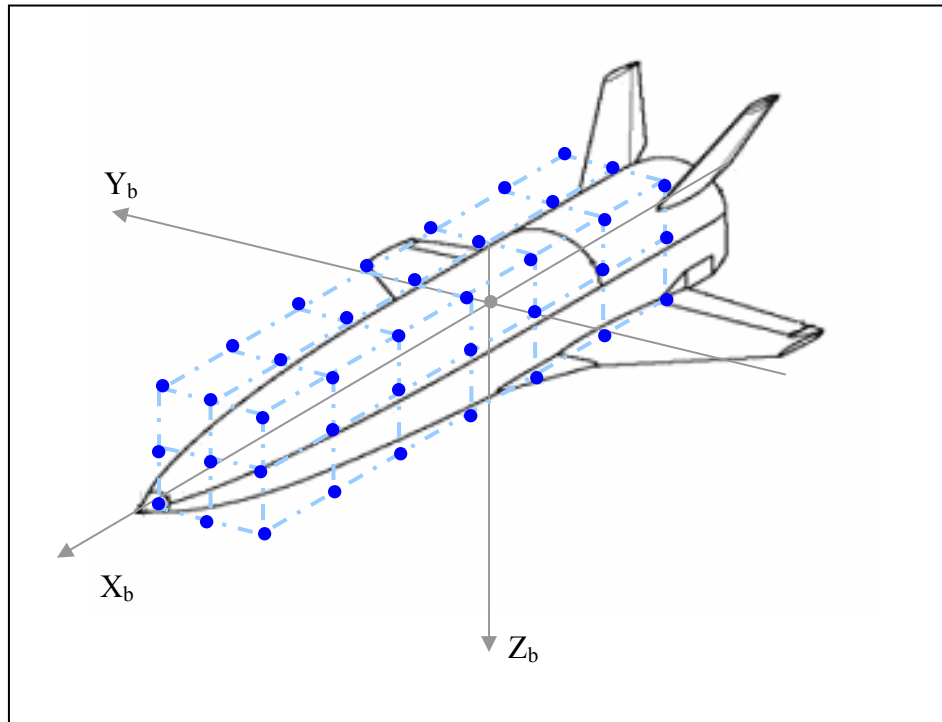
Fig. III - 2 – Analysis Grid (*not in scale*)

Following with the analysis, first of all it must be pointed up that in all the analyses conducted since now, the FTB_1 vehicle has been considered a rigid body; this means that, in the Eq. (III - 2):

$$\left[\dot{\mathbf{r}}_p\right]_B = \left[\ddot{\mathbf{r}}_p\right]_B = 0 \qquad \textbf{(III - 3)}$$

So, Eq. (III - 2) can be simplified and written as it follows:

$$\ddot{\mathbf{R}}_p = \ddot{\mathbf{R}}_0 + \left[\dot{\boldsymbol{\omega}}\right]_B \times \mathbf{r}_p + \boldsymbol{\omega} \times \left(\boldsymbol{\omega} \times \mathbf{r}_p\right) \qquad \textbf{(III - 4)}$$

Moreover, the Eq. (III - 4) can be explicitly rewritten considering that:

$$[\dot{\boldsymbol{\omega}}]_B \times \mathbf{r}_p = \begin{bmatrix} \dot{q}z_p - \dot{r}y_p \\ \dot{r}x_p - \dot{p}z_p \\ \dot{p}y_p - \dot{q}x_p \end{bmatrix}$$

(III - 5)

and:

$$\boldsymbol{\omega} \times (\boldsymbol{\omega} \times \mathbf{r}_p) = \begin{bmatrix} -(q^2 + r^2)x_p + pqy_p + prz_p \\ pqx_p - (p^2 + r^2)y_p + qrz_p \\ prx_p + qry_p - (p^2 + q^2)z_p \end{bmatrix}$$

(III - 6)

So, at the end we have:

$$\begin{cases} a_{x,p} = a_{x0} + \dot{q}z_p - \dot{r}y_p - (q^2 + r^2)x_p + pqy_p + prz_p \\ a_{y,p} = a_{y0} + \dot{r}x_p - \dot{p}z_p + pqx_p - (p^2 + r^2)y_p + qrz_p \\ a_{z,p} = a_{z0} + \dot{p}y_p - \dot{q}x_p + prx_p + qry_p - (p^2 + q^2)z_p \end{cases}$$

(III - 7)

III.3.a   Nominal Trajectory Analysis

About the nominal trajectory, the first thing that should be remarked is that, as already stated in § II.2.b.2, it is constrained in a longitudinal plane of motion; this means that both the roll and yaw angular rates (p, r) and angular accelerations ($\dot{p}, \dot{r}$) are identically = 0. As a consequence, we have:

$$[\dot{\boldsymbol{\omega}}]_B \times \mathbf{r}_p = \begin{bmatrix} \dot{q} z_p \\ 0 \\ -\dot{q} x_p \end{bmatrix} \qquad \textbf{(III - 8)}$$

and:

$$\boldsymbol{\omega} \times (\boldsymbol{\omega} \times \mathbf{r}_p) = \begin{bmatrix} -q^2 x_p \\ 0 \\ -q^2 z_p \end{bmatrix} \qquad \textbf{(III - 9)}$$

and, finally:

$$\begin{cases} a_{x,p} = a_{x0} + \dot{q} z_p - q^2 x_p \\ a_{y,p} = a_{y0} = 0 \\ a_{z,p} = a_{z0} - \dot{q} x_p - q^2 z_p \end{cases} \qquad \textbf{(III - 10)}$$

The acceleration on the y-axis is $= 0$ again because of the characteristics of the nominal trajectory.

From Eq. (III - 10) it can be deduced that the points of the analysis grid in which it will be possible to expertise a modification in the sensed accelerations are identified just by means of the x_p, z_p coordinates, i.e. the modifications on the sensed accelerations are independent of y_p. Moreover, the only components of accelerations that are affected are the ones along the x and z axes.

As a consequence, in order to obtain the results that will now be shown, it has been considered a 2-D analysis grid, constrained in the x-z plane, supposing $y_p = 0$. The grid is shown in Fig. III - 3.
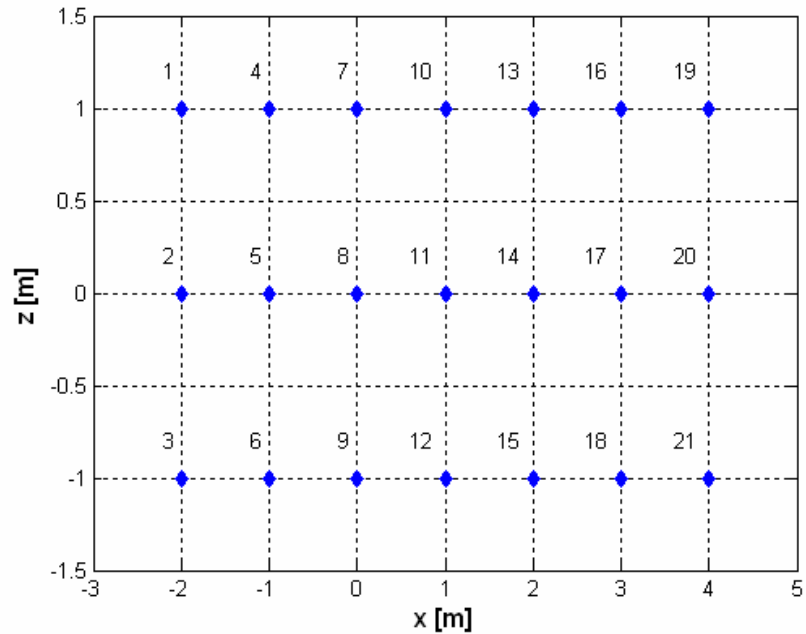
Fig. III - 3 – 2-D Analysis Grid for the Nominal Trajectory Case

In the following there will be shown the plots of the accelerations along the x and z axes, for the points of the analysis grid (Fig. III - 4); moreover, there will be shown the plots of the residual acceleration, i.e. the difference between the sensed acceleration in the *p*-th point and the acceleration of the C.o.M. of the vehicle (Fig. III - 5 to Fig. III - 7).
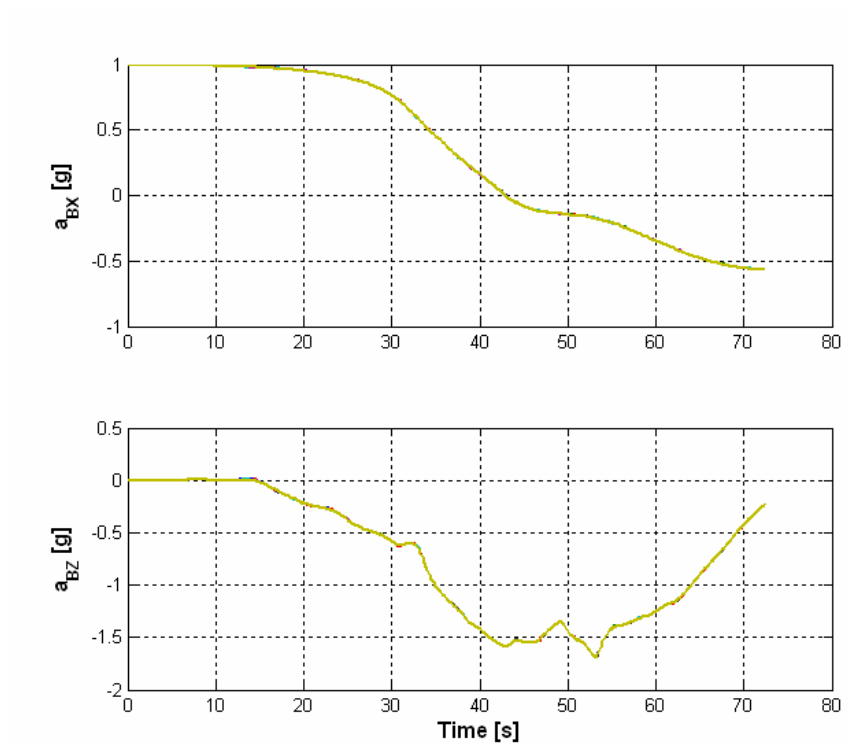
Fig. III - 4 – Acceleration in the Analysis Grid Points, along the Noiminal Trajectory

As it can be seen from Fig. III - 4, the accelerations in the considered points are actually superimposed; in fact, the following plots of the residual accelerations show a very slight difference (in order of magnitude of mg) with respect to the one in the centre of mass.

About the plots of the residual accelerations, in them of course is not considered Point 8 of the grid, ≡ with the C.o.M., and so such to have no residual acceleration.
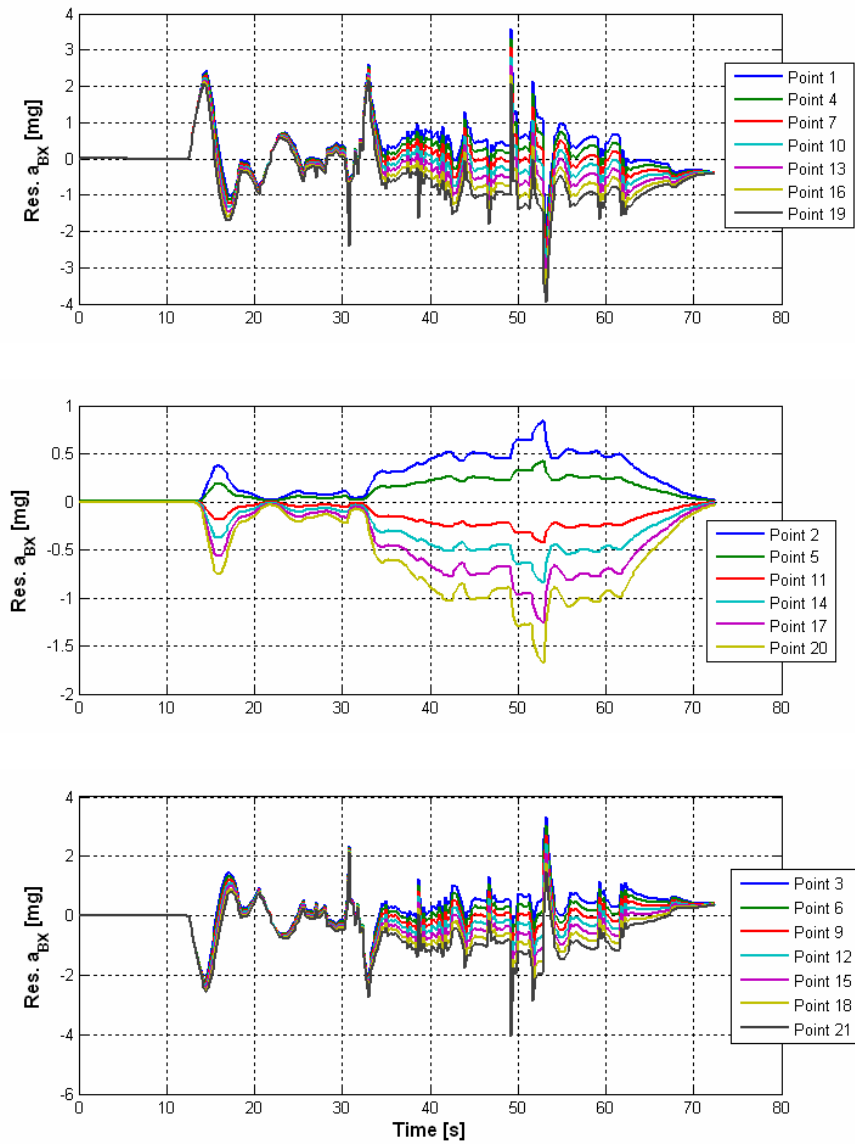
Fig. III - 5 – Residual X-Accelerations in the Analysis Grid Points, along the Noiminal Trajectory
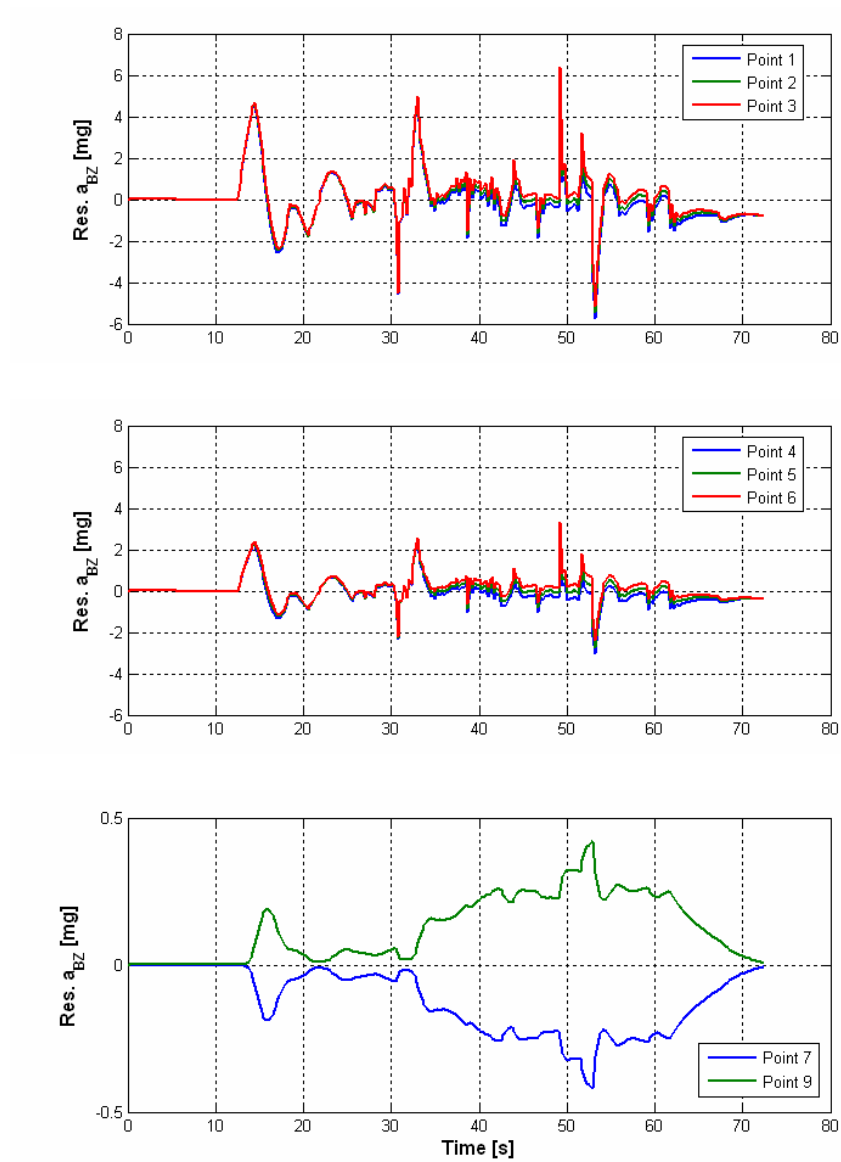
**Fig. III - 6 – Residual Z-Accelerations in the Analysis Grid Points, along the
Noiminal Trajectory – 1/2**
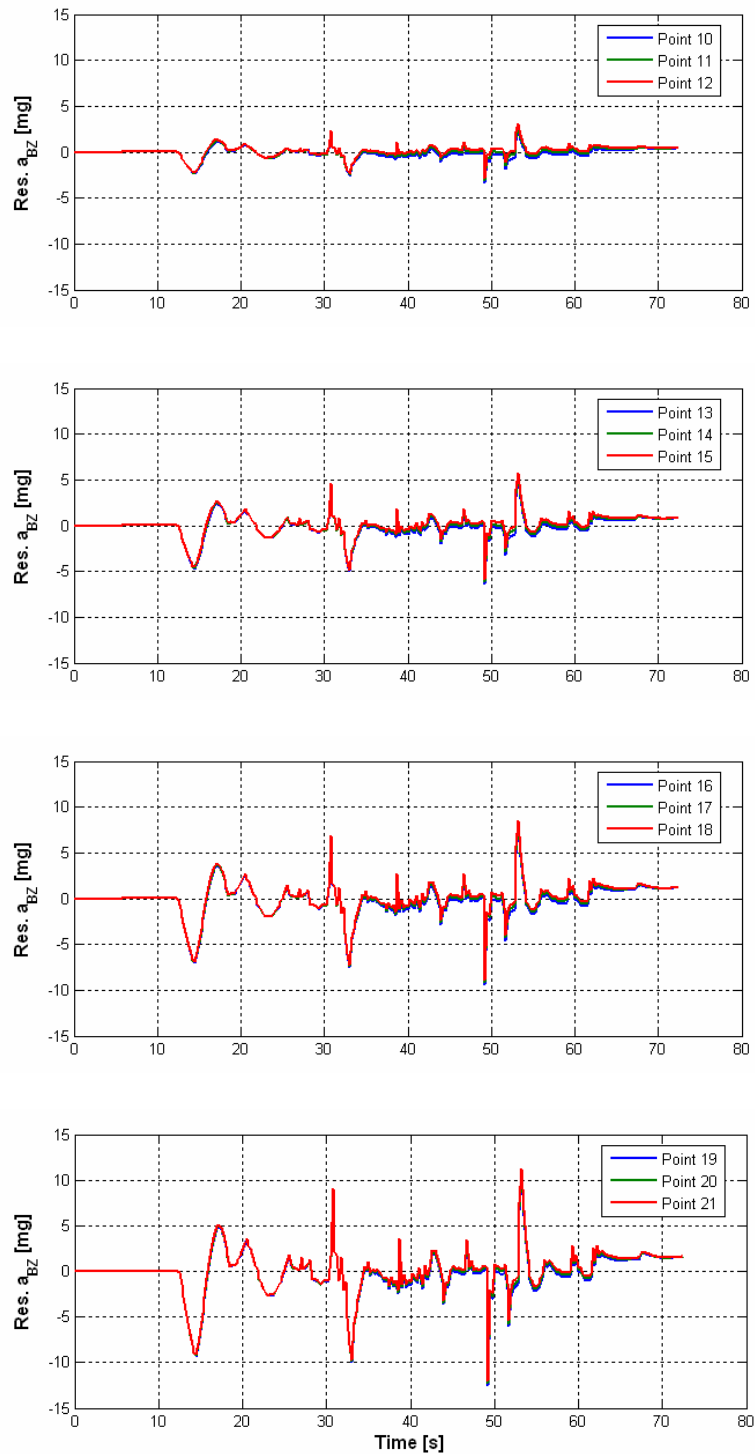
Fig. III - 7– Residual Z-Accelerations in the Analysis Grid Points, along the Noiminal Trajectory – 2/2

From an analysis of Fig. III - 4 to Fig. III - 7, several conclusions can be drawn.

First of all, it can be noticed how the acceleration levels along the x-axis change remarkably as the z_p coordinate changes, and, at the same way, how the acceleration levels along the z-axis change with the x_p coordinate. In Fig. III - 5, in fact, the three subplot regroup points with the same z_p but with different x_p, while in Fig. III - 6/Fig. III - 7 they regroup points with the same x_p but with different z_p. Comparing the differences the aforementioned behaviour appears as evident.

Recalling Eq. (III - 10), it is possible to understand that what happens is that the term in q^2 is predominant with respect to the term in $\dot{q}$; the following Fig. III - 8, Fig. III - 9 show q^2 and $\dot{q}$ along the nominal trajectory, demonstrating the correctness of this conclusion.
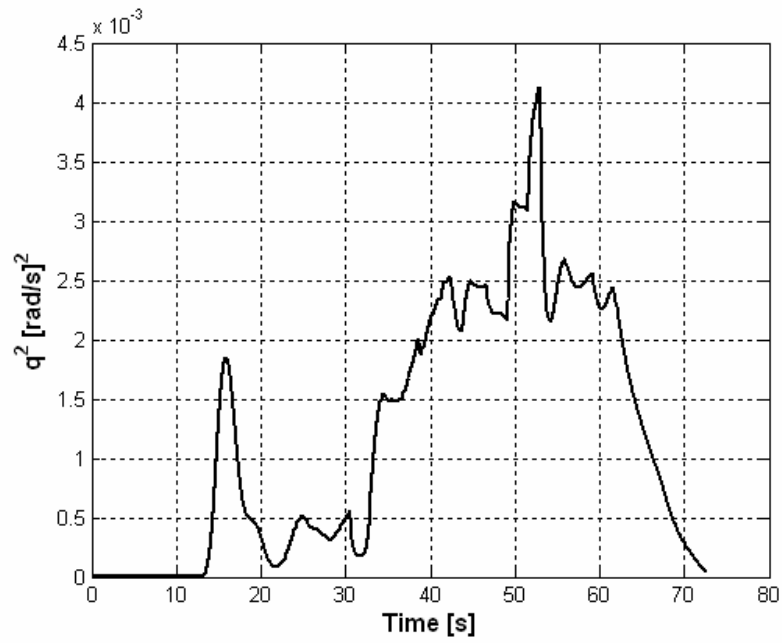
Fig. III - 8 – q^2 Pofile along the Nominal Trajectry
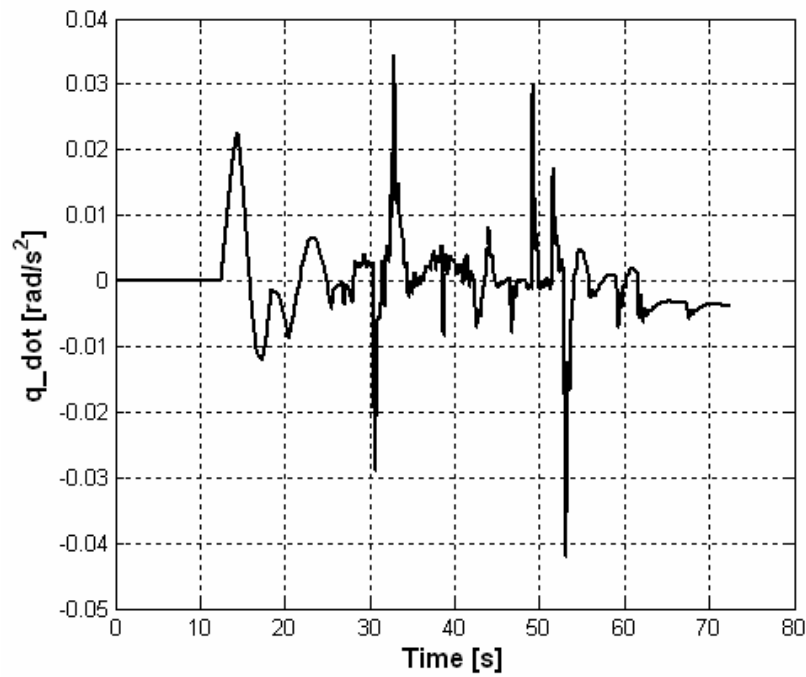
Fig. III - 9 – q̇ Profile Along the Nominal Trajectory

Another relevant conclusion that can be drawn from an analysis of the figures, especially Fig. III - 4, is that the gravity levels inherent to the DTFT Mission are sensibly higher than the ones of a microgravity mission, and this independently of the analysed point. The only part of the trajectory that seems to be characterised by low gravity level is the first one, when the vehicle is free-falling after the drop from the balloon, and its velocity is too low to generate relevant aerodynamic forces.

This phase has been already identified as significant in the design of the flight control laws; prior to the point in which the aerodynamic controls become effective, in fact, there is no possibility to guide the vehicle on any pre-fixed path, and so in this phase the control system simply try to nullify the eventually present angular rates This phase of the trajectory is named "Acceleration Phase". The condition in which there is enough controllability to pilot the vehicle is identified as:

► Mach > 0.4 AND q_∞ > 400 Pa

The time in which this condition is reached is, for the nominal trajectory, ≈ 12 s;

In the following figures, the gravity levels associated with the flight phase before this condition is reached are shown.
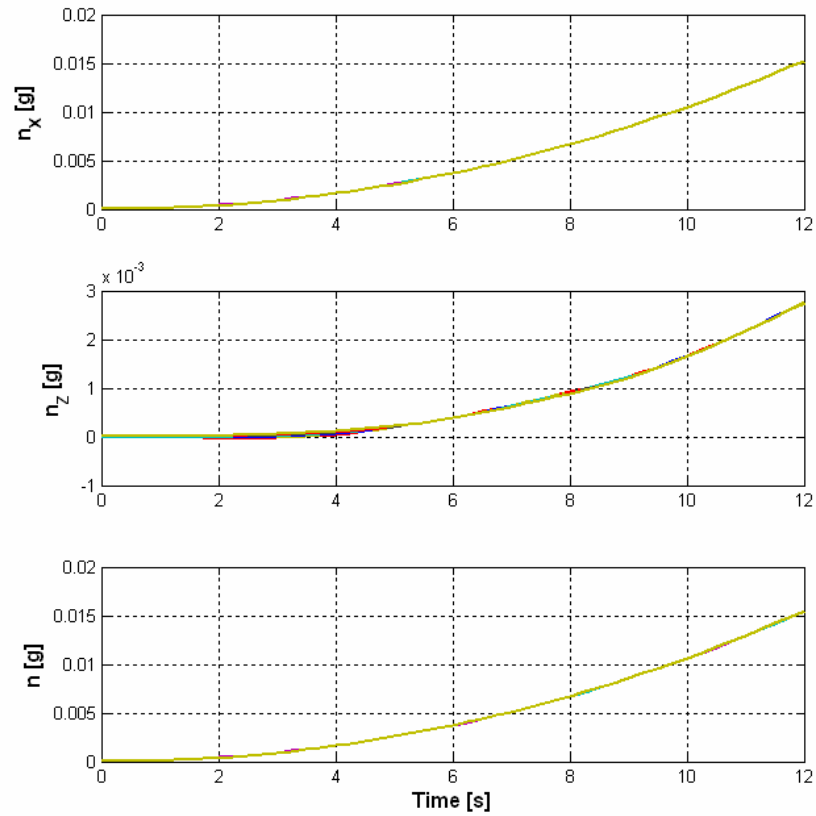
**Fig. III - 10 – Load Factors in the Analysis Grid Points, along the Nominal
Trajectory – Acceleration Phase**

In Fig. III - 10 are shown the load factors along the nominal trajectory;

recall that they are defined as:

$$\begin{cases} n_X = \dfrac{g_X - a_{B,X}}{g} \\[3mm] n_Z = \dfrac{g_Z - a_{B,Z}}{g} \end{cases} \qquad\qquad \textbf{(III - 11)}$$

$$\downarrow$$

$$n = \sqrt{n_X^2 + n_Z^2}$$

As it can be seen from the figure, also in this case, as for the accelerations in Fig. III - 4, the plots for the different analysed points are superimposed; this is a consequence of the fact that, in this phase of the trajectory, the angular rates are very low.

In the following there will be shown the total and residual accelerations in the analysed points.
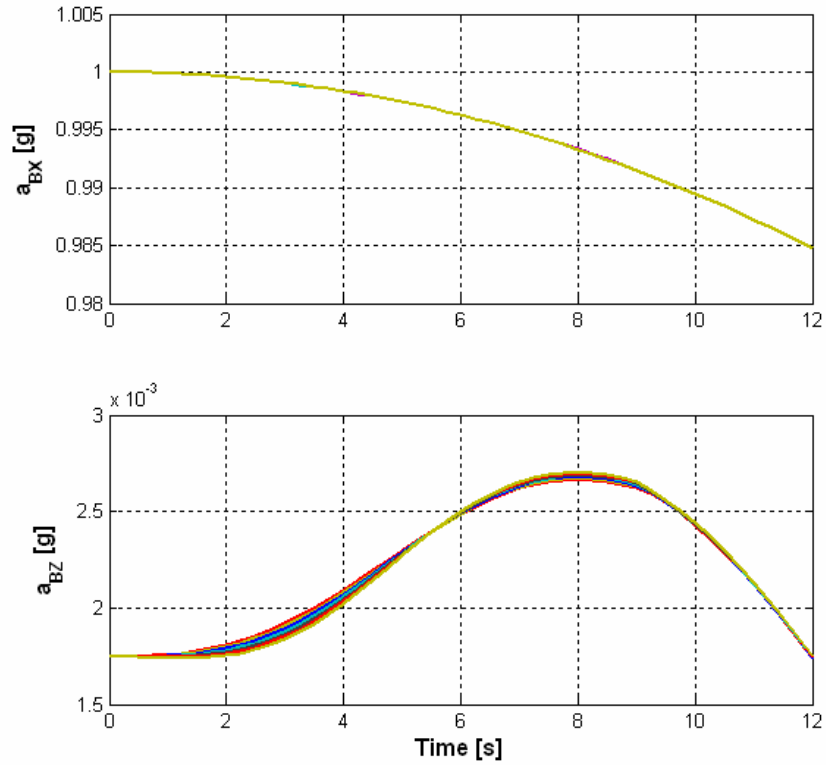
**Fig. III - 11 - – Acceleration in the Analysis Grid Points, along the Noiminal
Trajectory – Acceleration Phase**
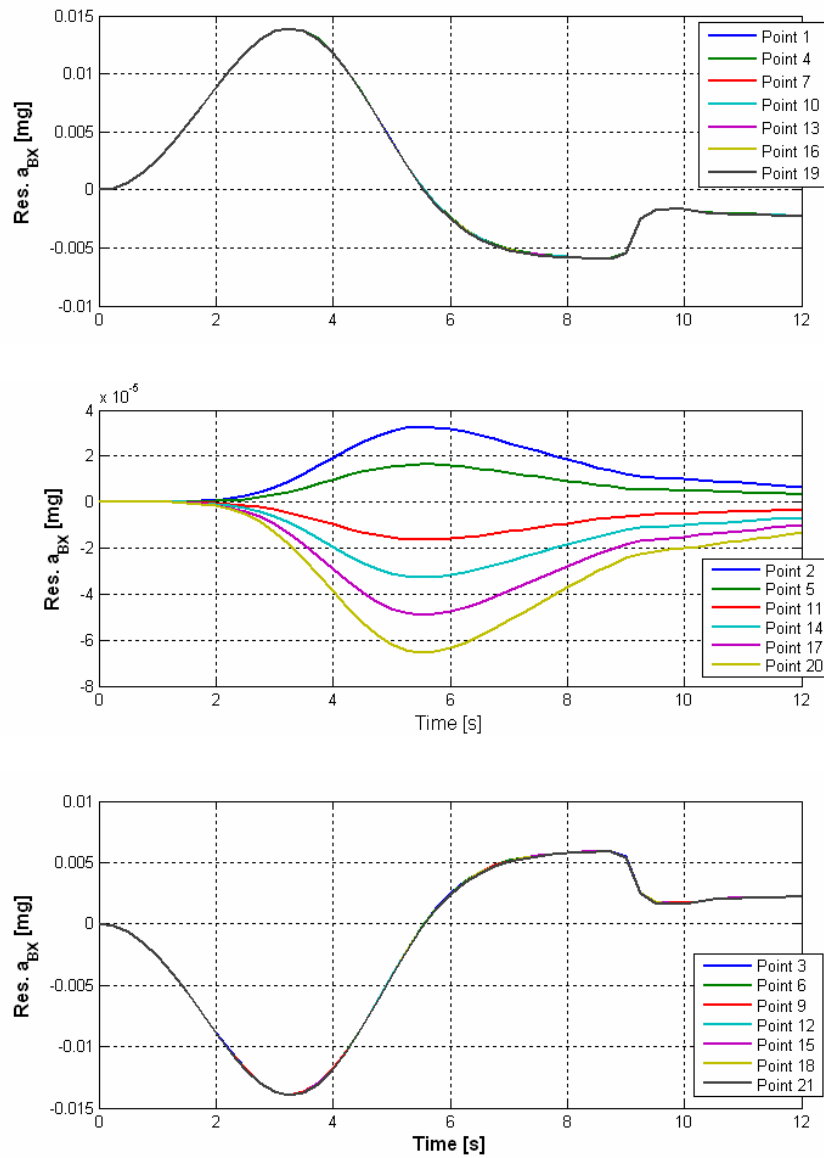
**Fig. III - 12 – Residual X-Accelerations in the Analysis Grid Points, along the
Nominal Trajectory – Acceleration Phase**
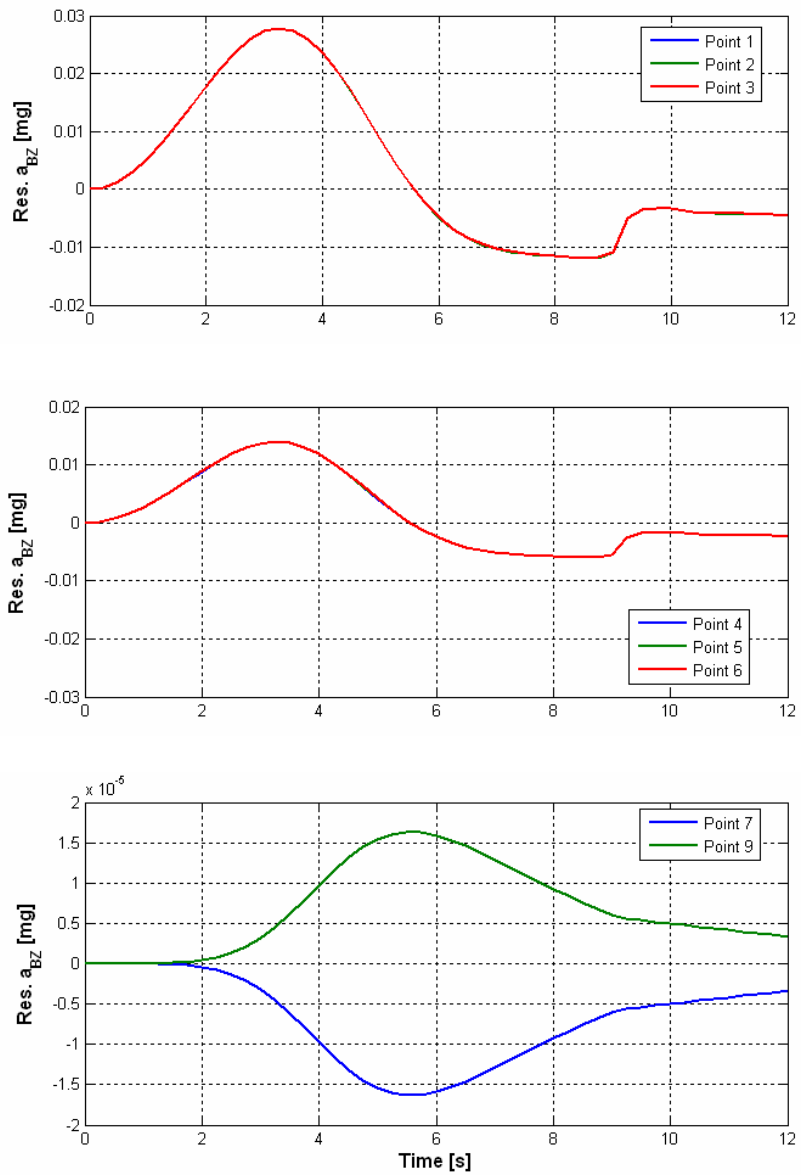
**Fig. III - 13– Residual Z-Accelerations in the Analysis Grid Points, along the
Nominal Trajectory – Acceleration Phase – 1/2**
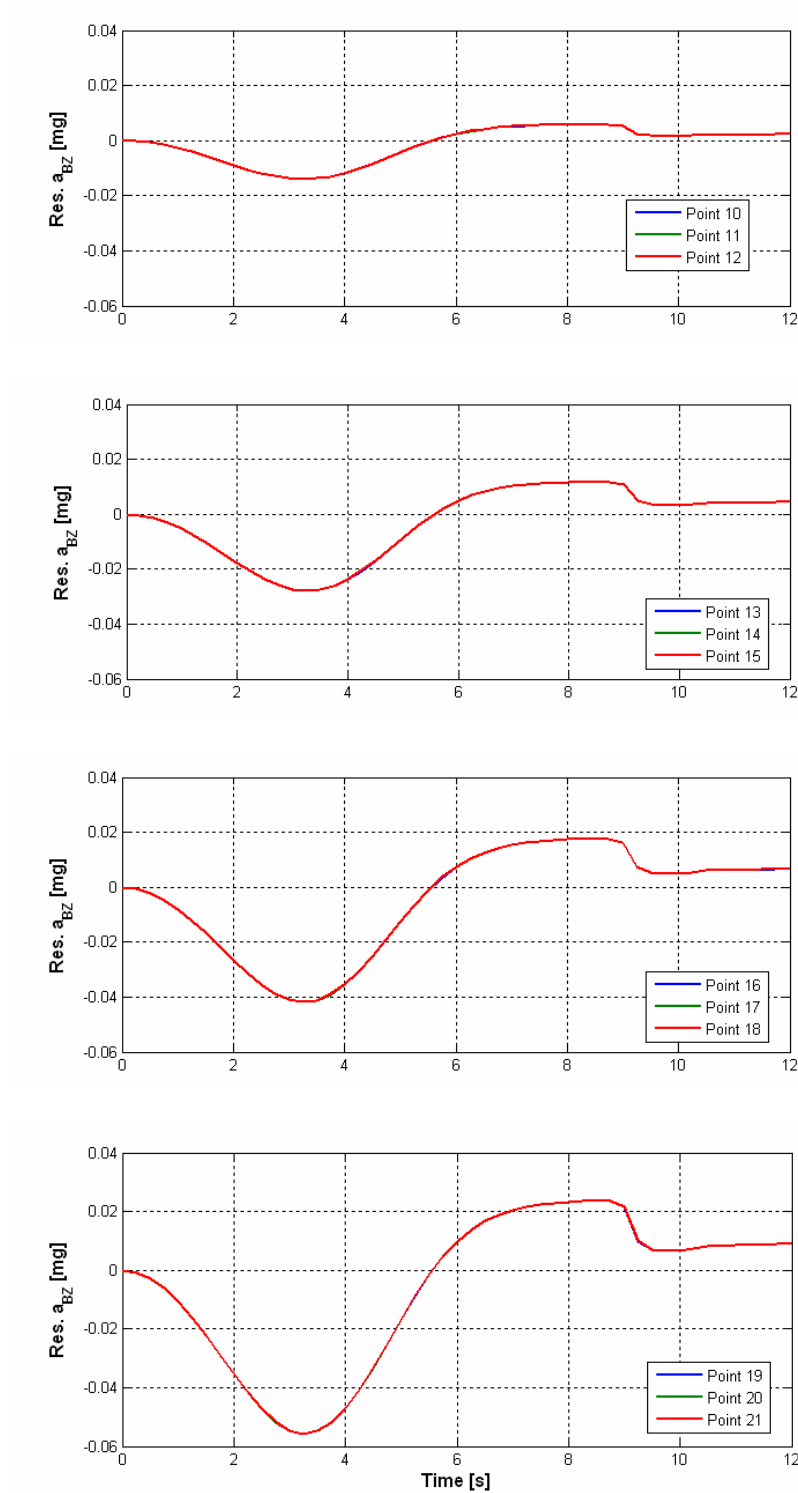
Fig.III - 14– Residual Z-Accelerations in the Analysis Grid Points, along the Nominal Trajectory – Acceleration Phase – 2/2

III.3.b   Dispersed Trajectories Analysis

In this paragraph there will be documented the results of the study of the gravitational levels characterising the DTFT dispersed trajectories obtained from the Monte Carlo analysis described in the previous chapter.

This study has been conducted considering all the points of the 3-D analysis grid shown in Fig. III - 2; in the analysed cases, in fact, it is not possible to make simplifications as the ones reported at the beginning of the previous paragraph, because, due to the various acting disturbances, the trajectories are no more constrained in a longitudinal plane of motion. In any case, for simplicity and clarity there will reported only the results referred to the origin of the body reference frame (i.e. the C.o.M, with coordinates [0,0,0]) and the extreme points of the grid.

In the following figures there will be shown the profiles of the load factors (where it will be defined $n = \sqrt{n_X^2 + n_Y^2 + n_Z^2}$) and, for the points different from the C.o.M., of the residual accelerations; it will be considered only the acceleration phase.
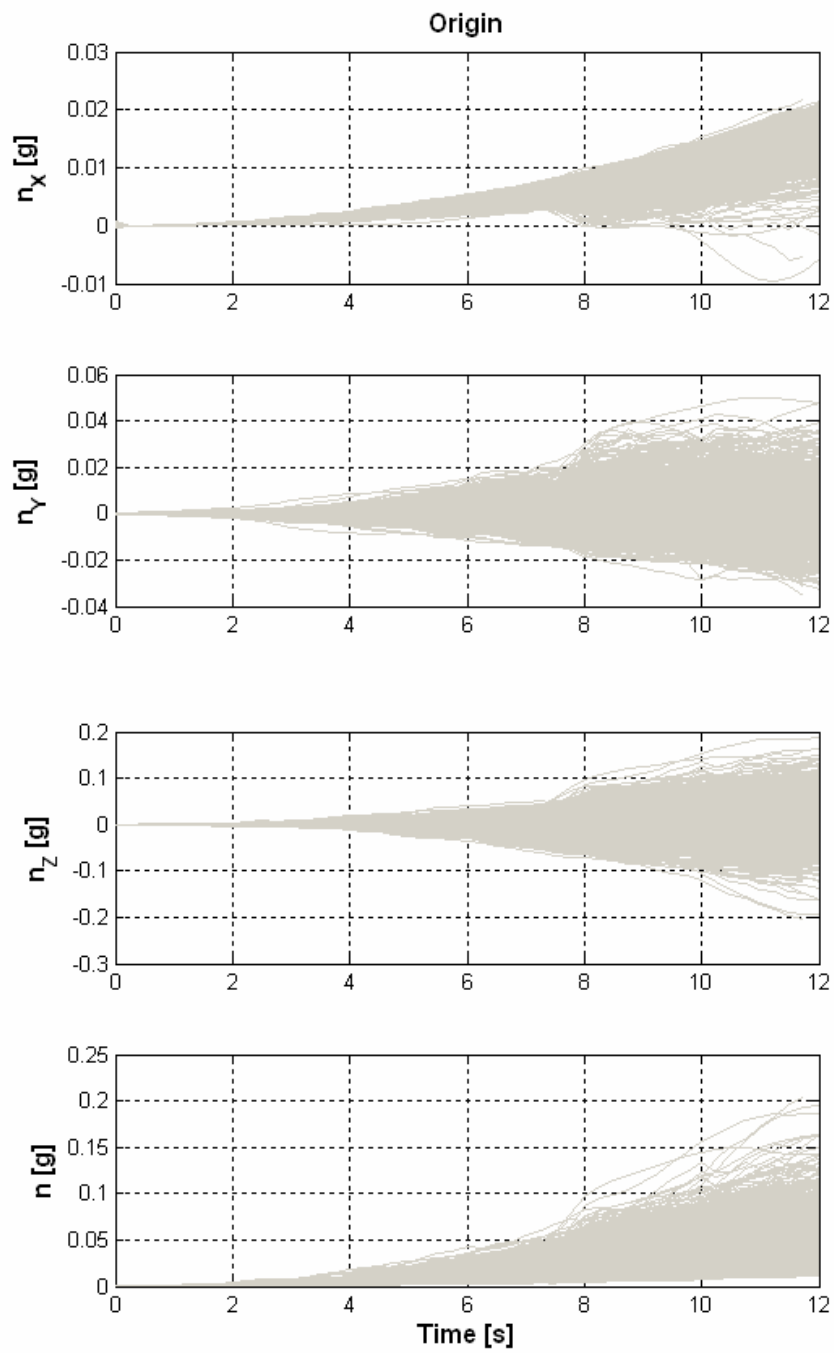
Fig. III - 15 – Load Factors – Acceleration Phase
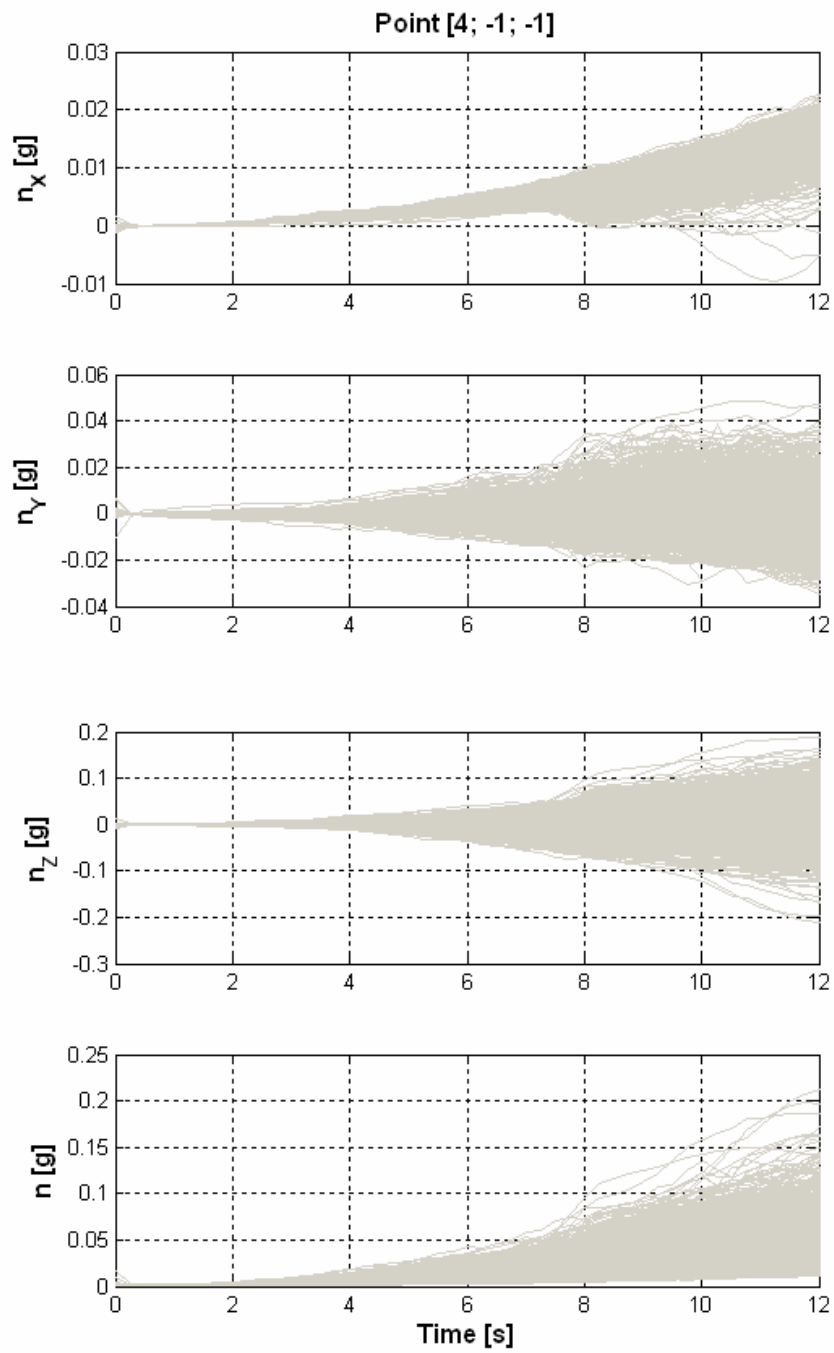
Fig. III - 16 – Load Factors in the Grid Point [4, -1, -1] – Acceleration Phase
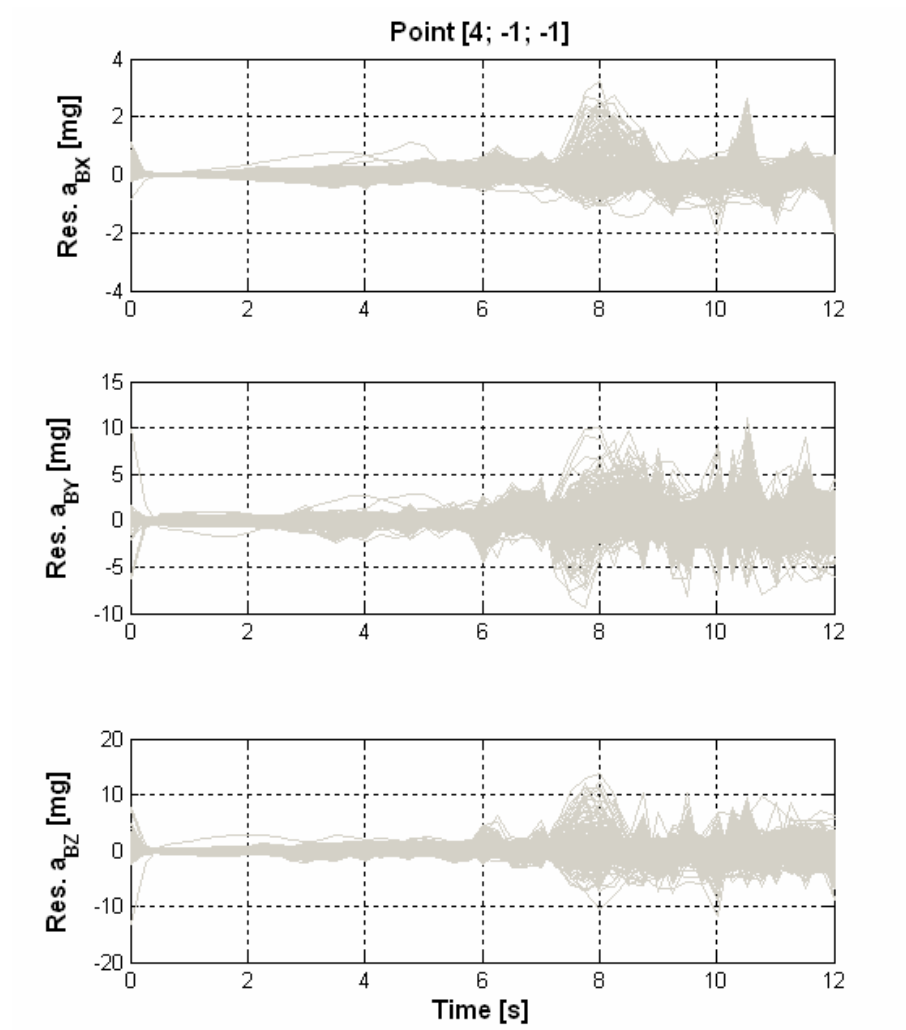
Fig. III - 17– Residual Accelerations in the Grid Point [4, -1, -1] – Acceleration Phase
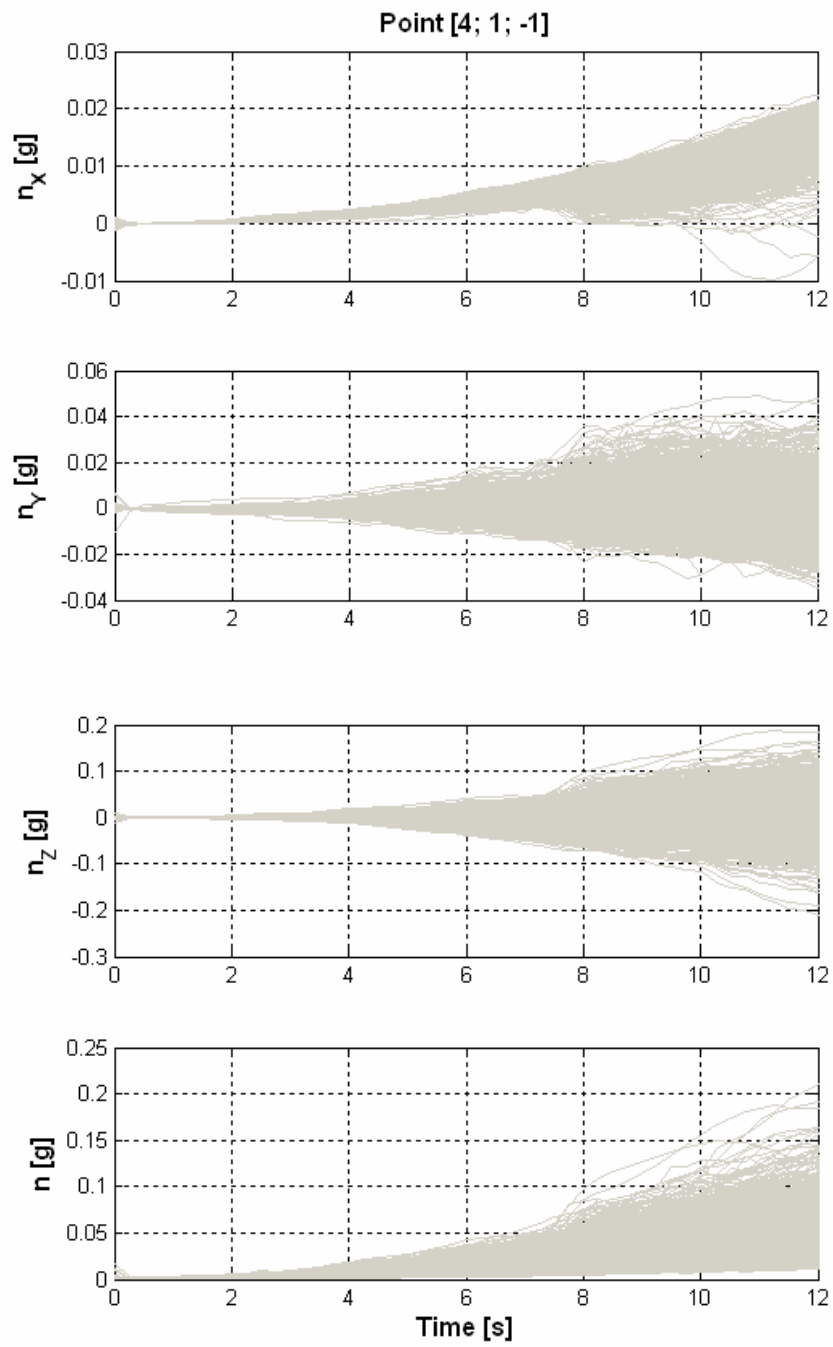
Fig. III - 18 – Load Factors in the Grid Point [4, 1, -1] – Acceleration Phase
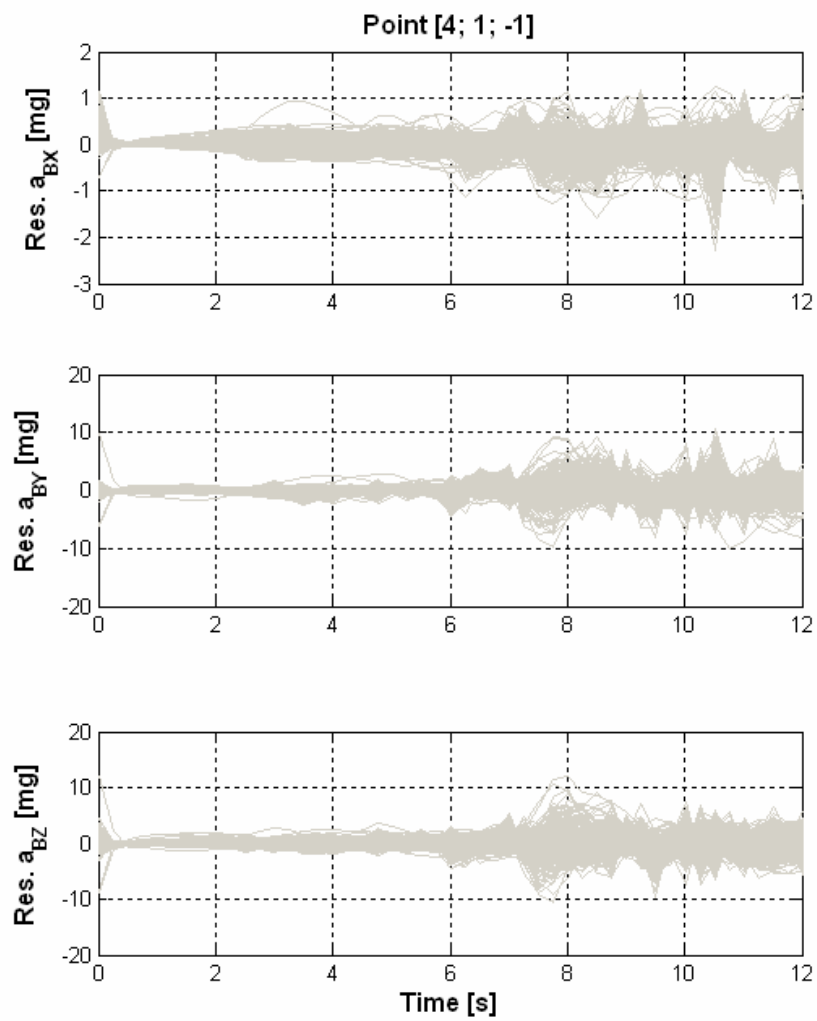
**Fig. III - 19– Residual Accelerations in the Grid Point [4, 1, -1] – Acceleration
Phase**
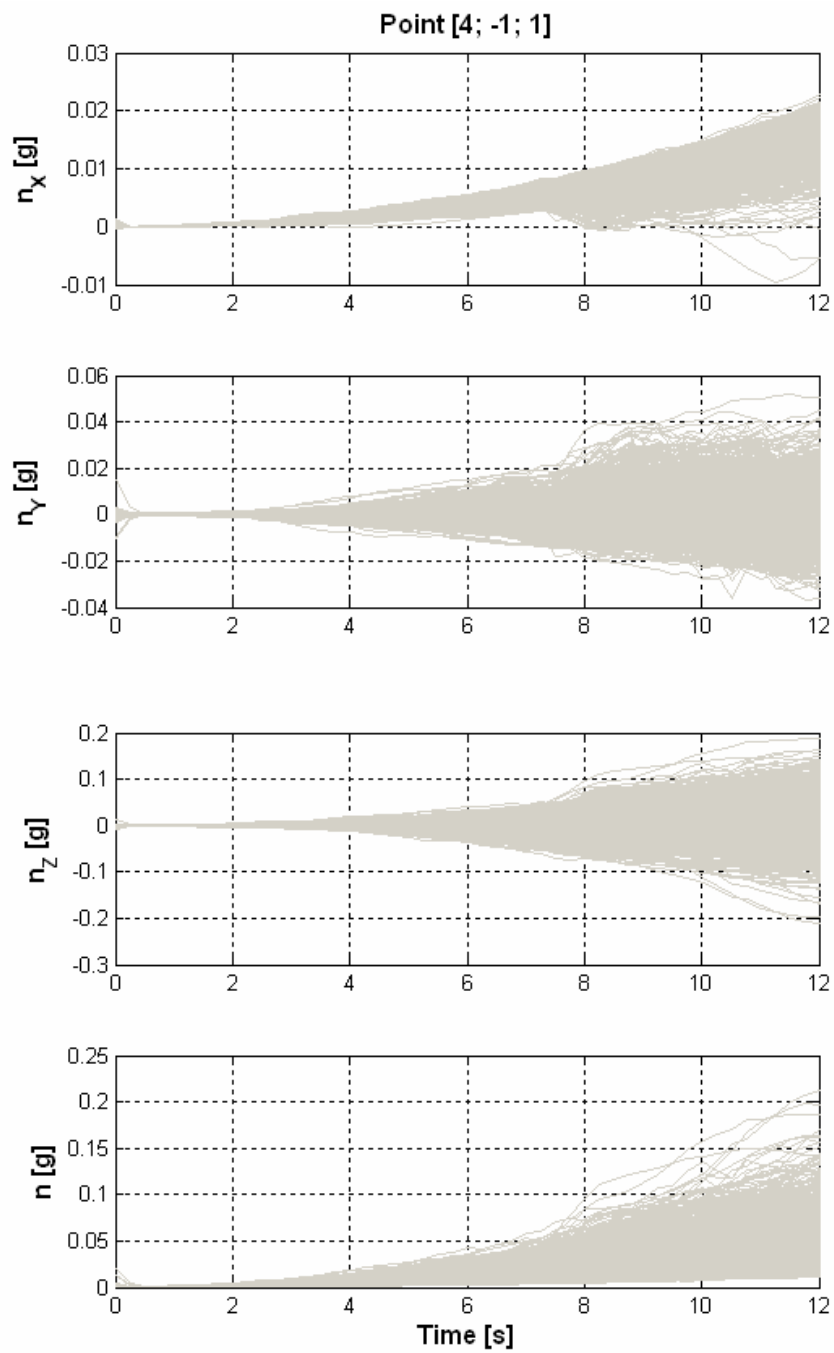
Fig. III - 20 – Load Factors in the Grid Point [4, -1, 1] – Acceleration Phase
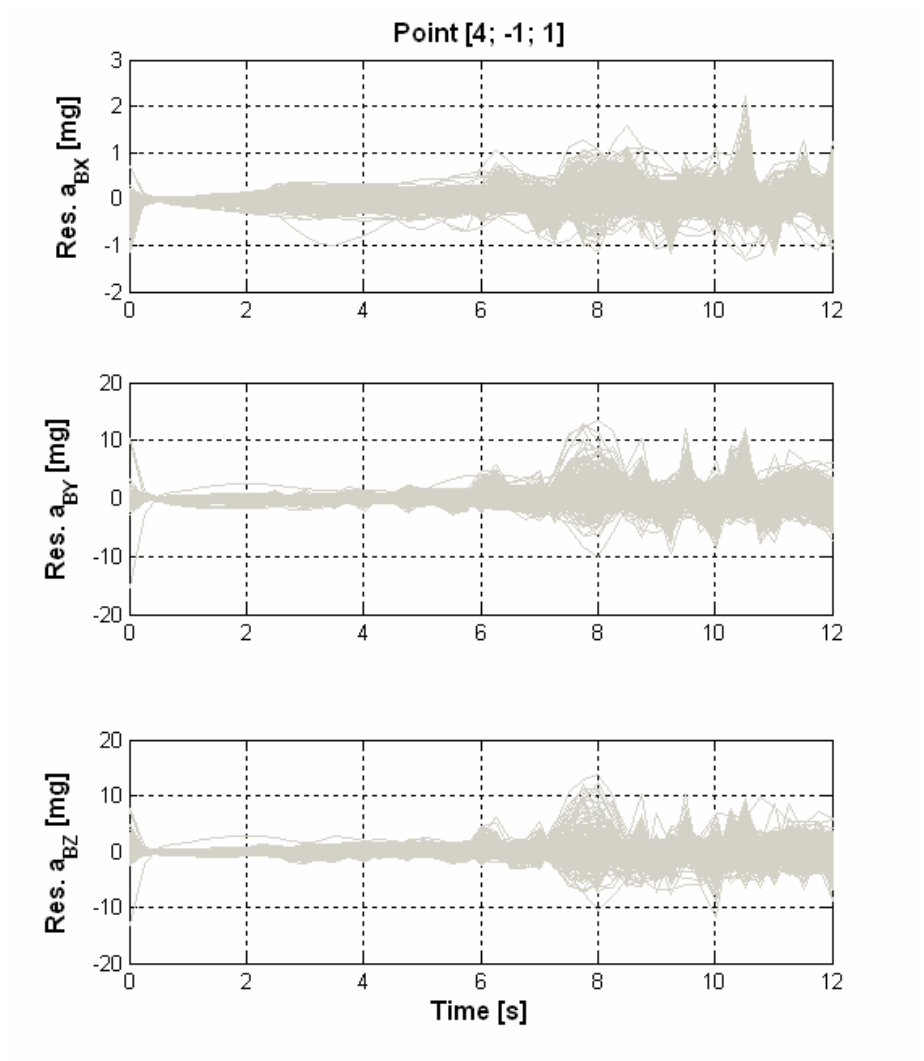
Fig. III - 21– Residual Accelerations in the Grid Point [4, -1, 1] – Acceleration Phase
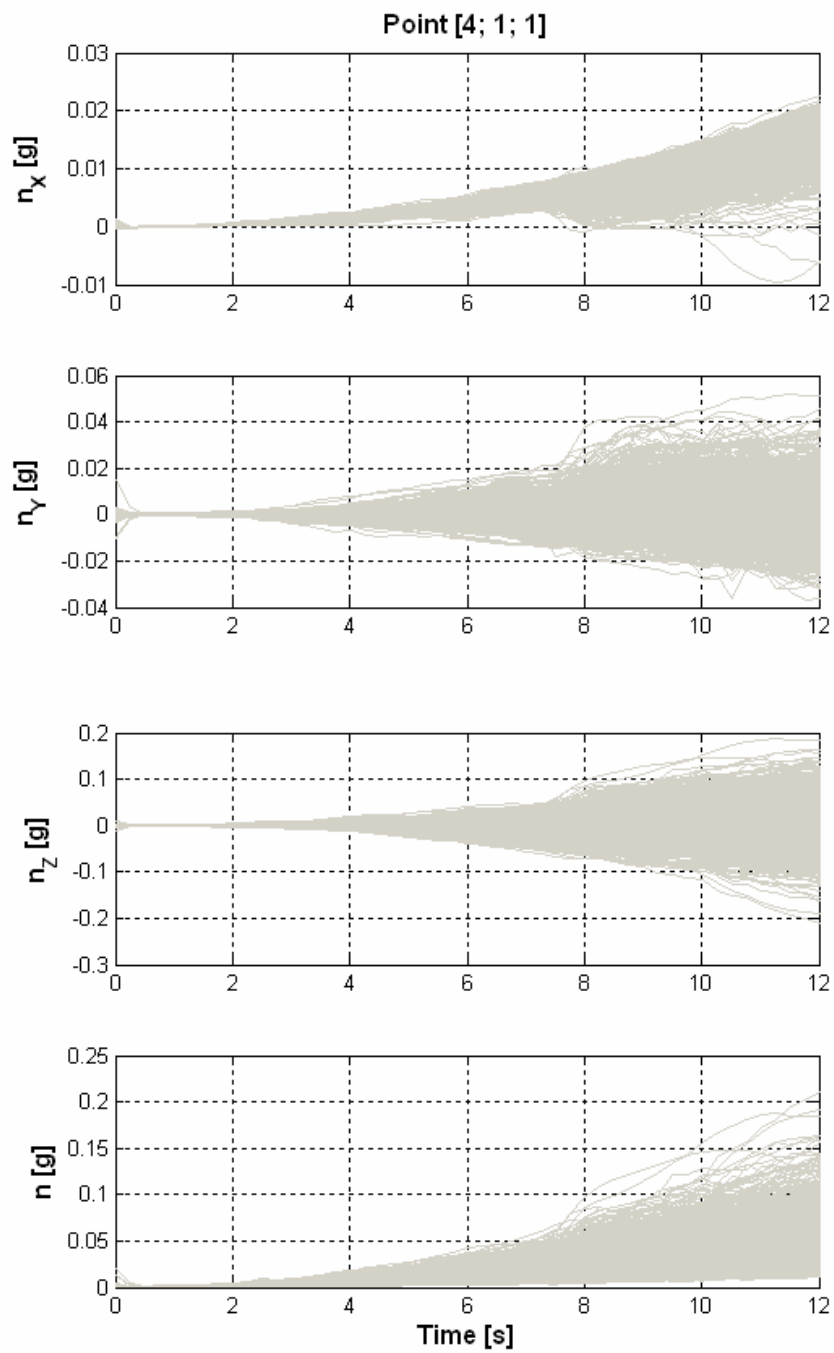
Fig. III - 22 – Load Factors in the Grid Point [4, 1, 1] – Acceleration Phase
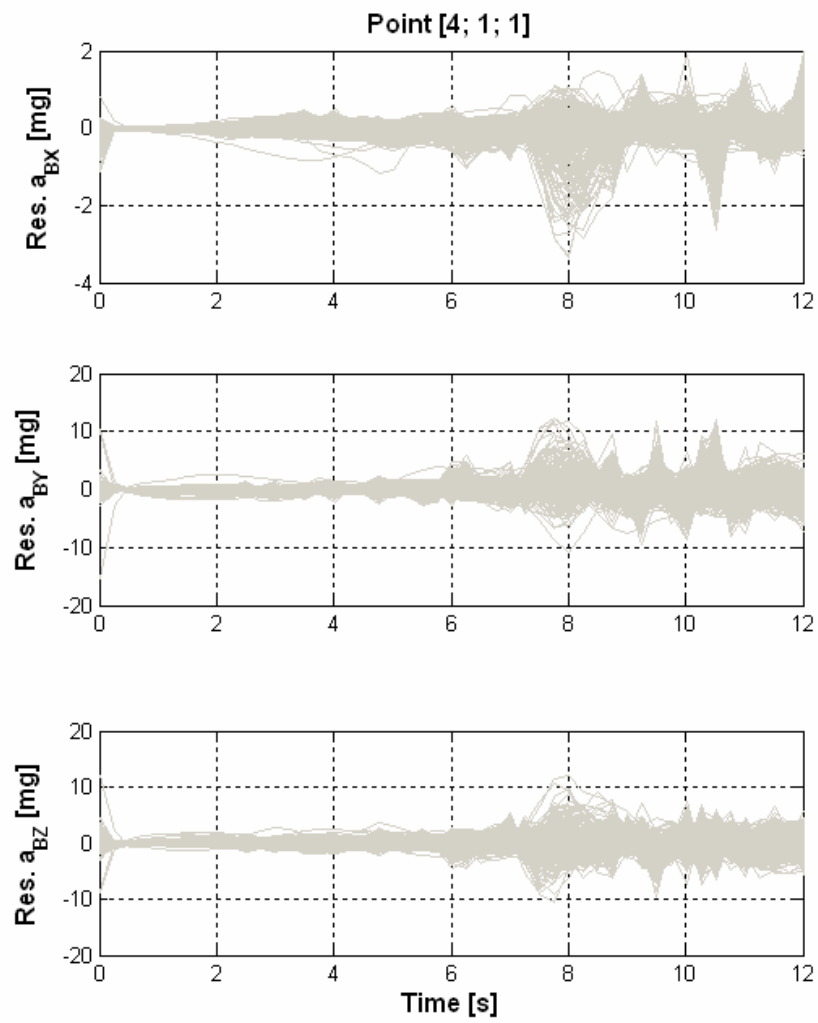
Fig. III - 23– Residual Accelerations in the Grid Point [4, 1, 1] – Acceleration Phase
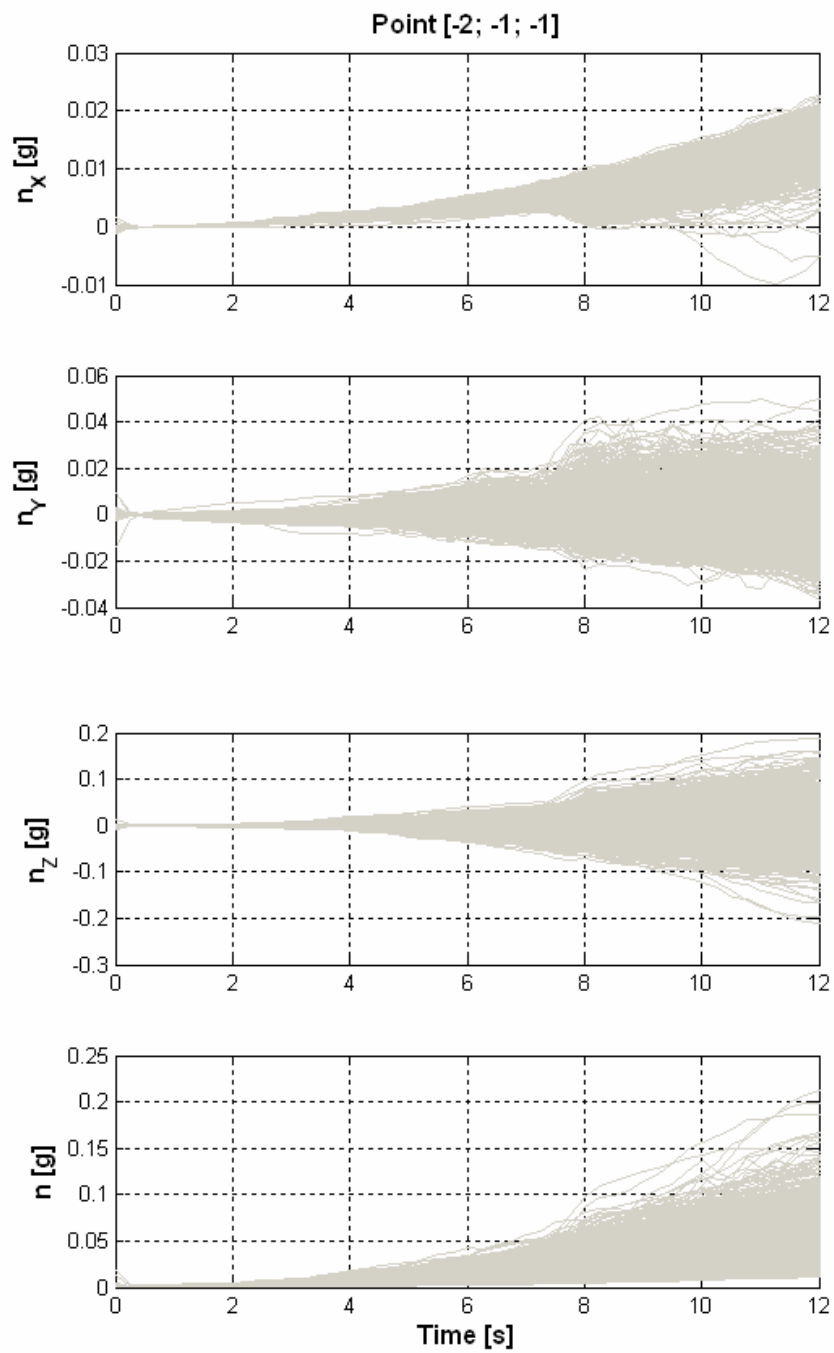
Fig. III - 24 – Load Factors in the Grid Point [-2, -1, -1] – Acceleration Phase
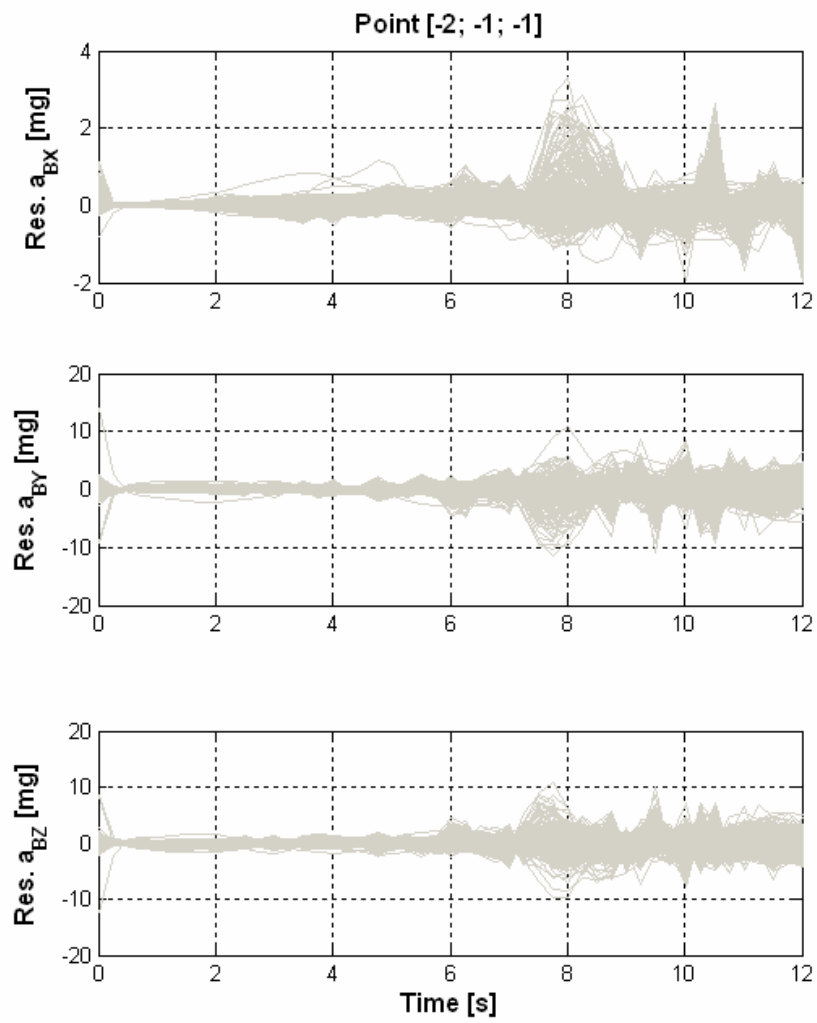
**Fig. III - 25– Residual Accelerations in the Grid Point [-2, -1, -1] – Acceleration
Phase**
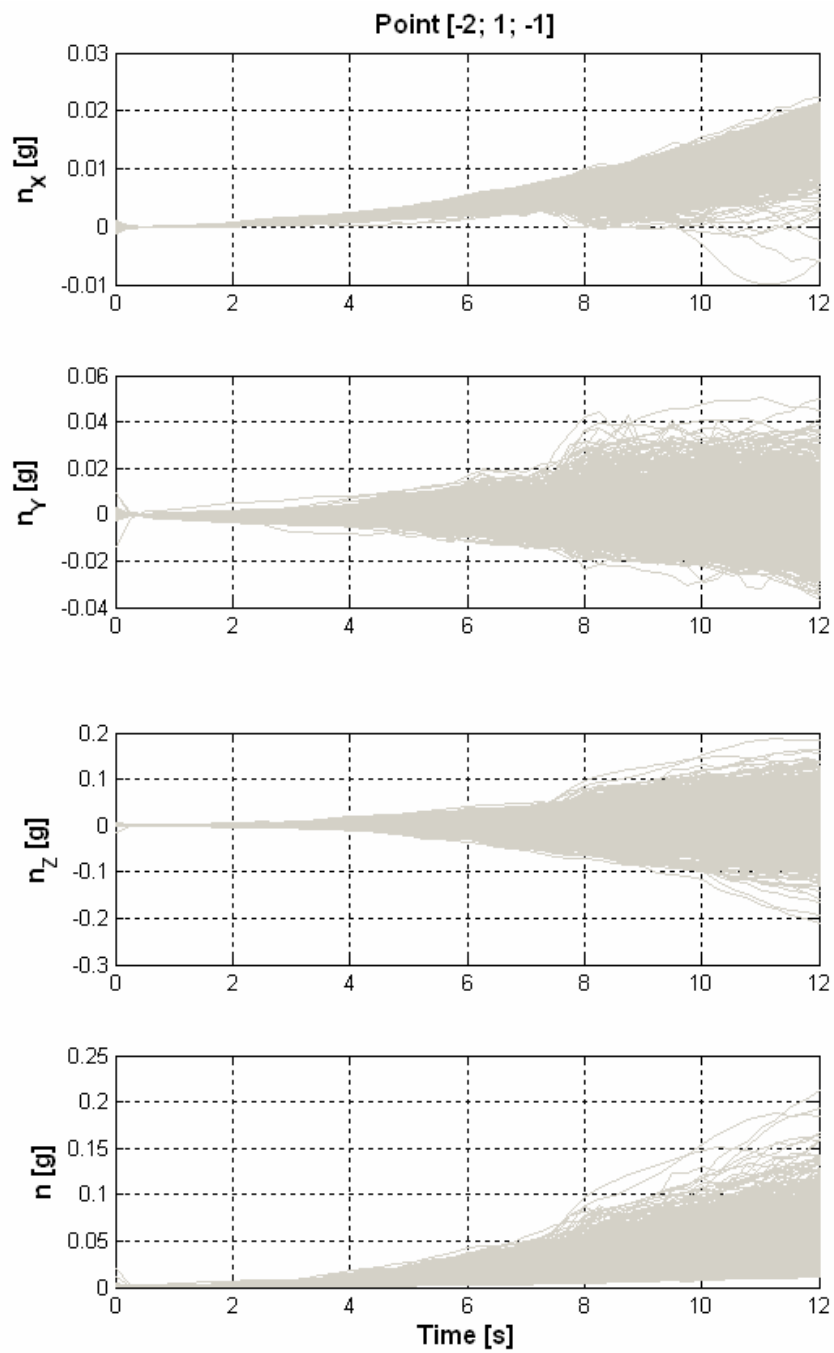
Fig. III - 26 – Load Factors in the Grid Point [-2, 1, -1] – Acceleration Phase
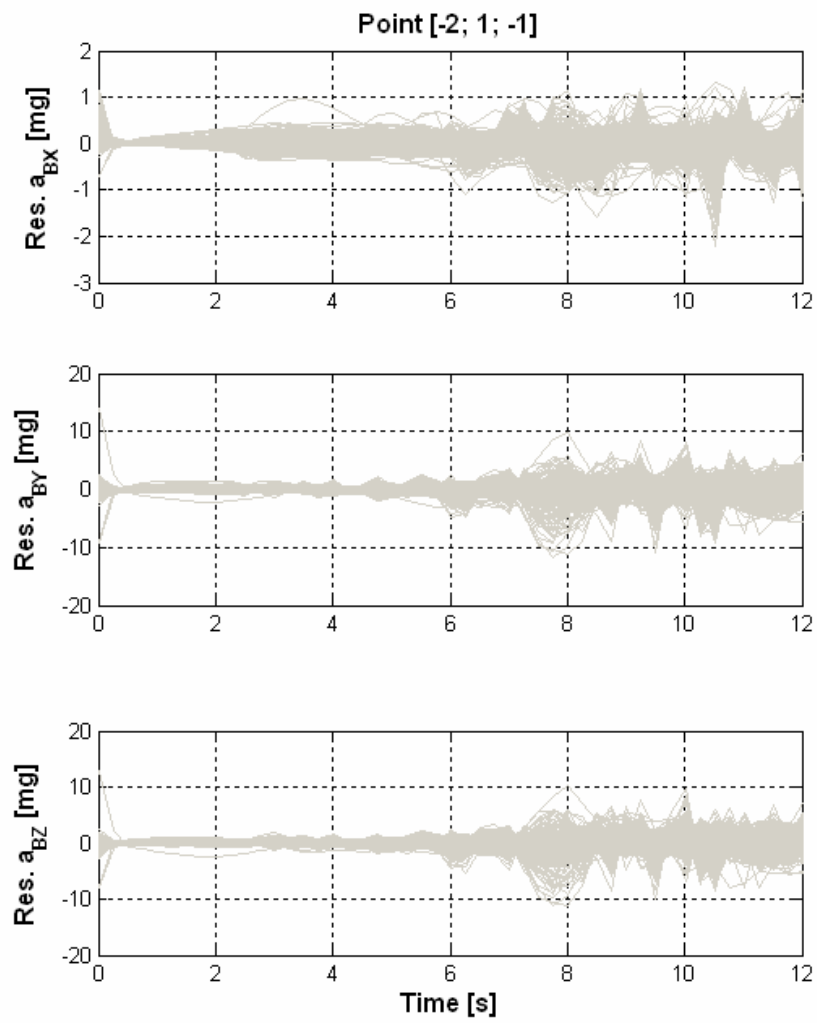
**Fig. III - 27– Residual Accelerations in the Grid Point [-2, 1, -1] – Acceleration
Phase**
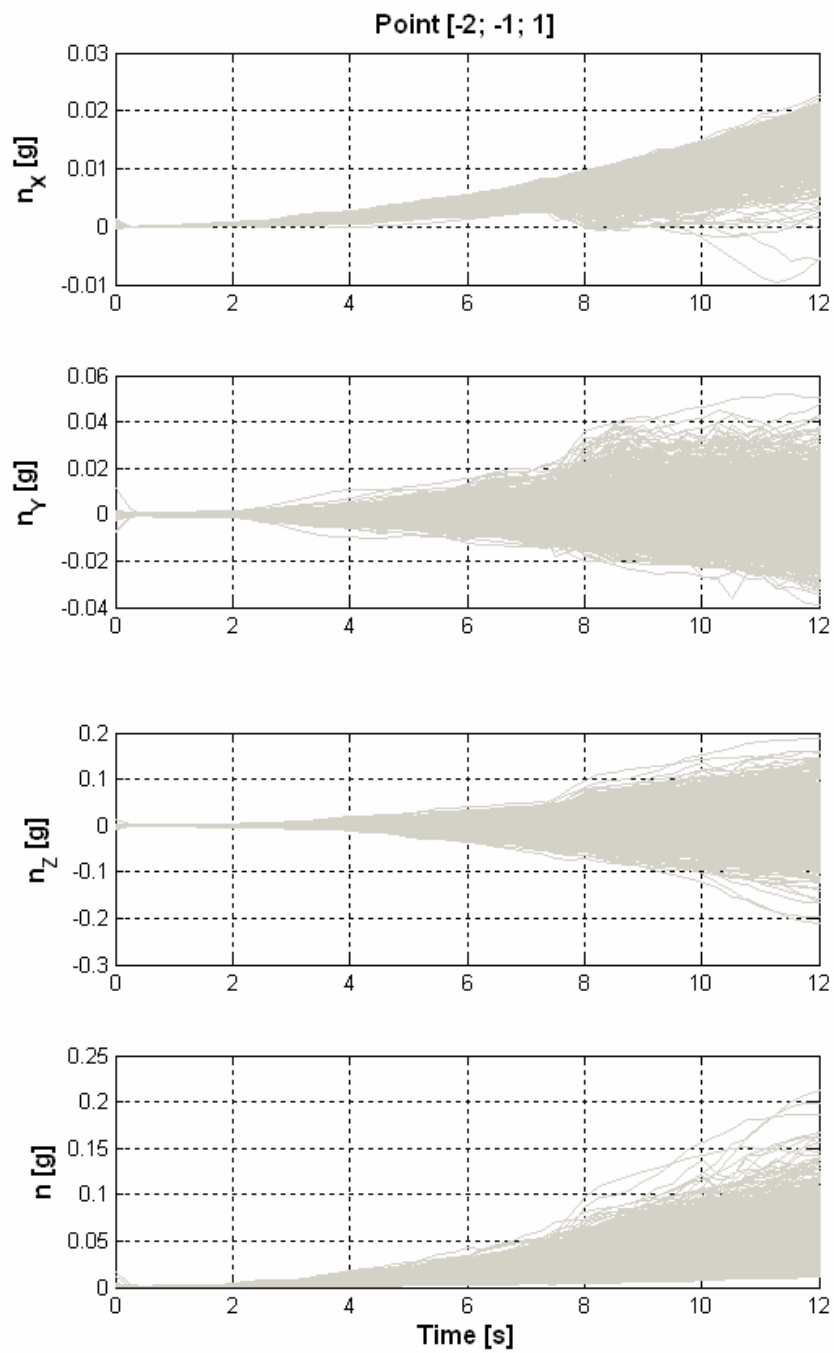
Fig. III - 28 – Load Factors in the Grid Point [-2, -1, 1] – Acceleration Phase
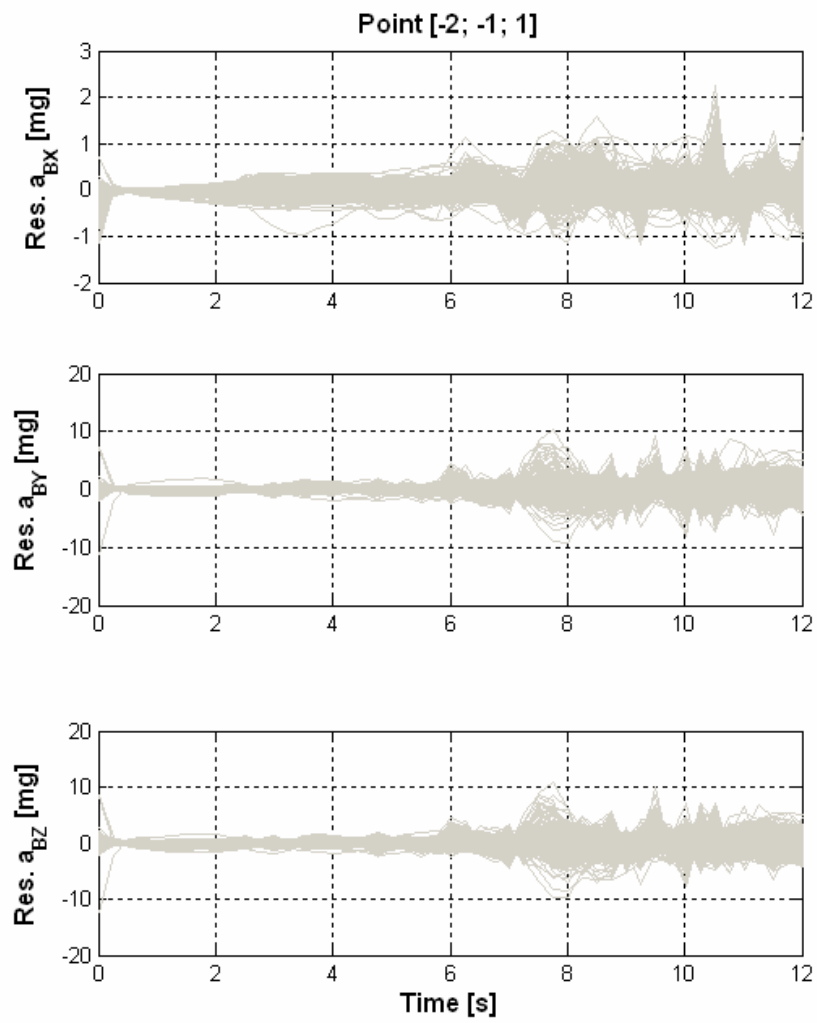
Fig. III - 29– Residual Accelerations in the Grid Point [-2, -1, 1] – Acceleration Phase
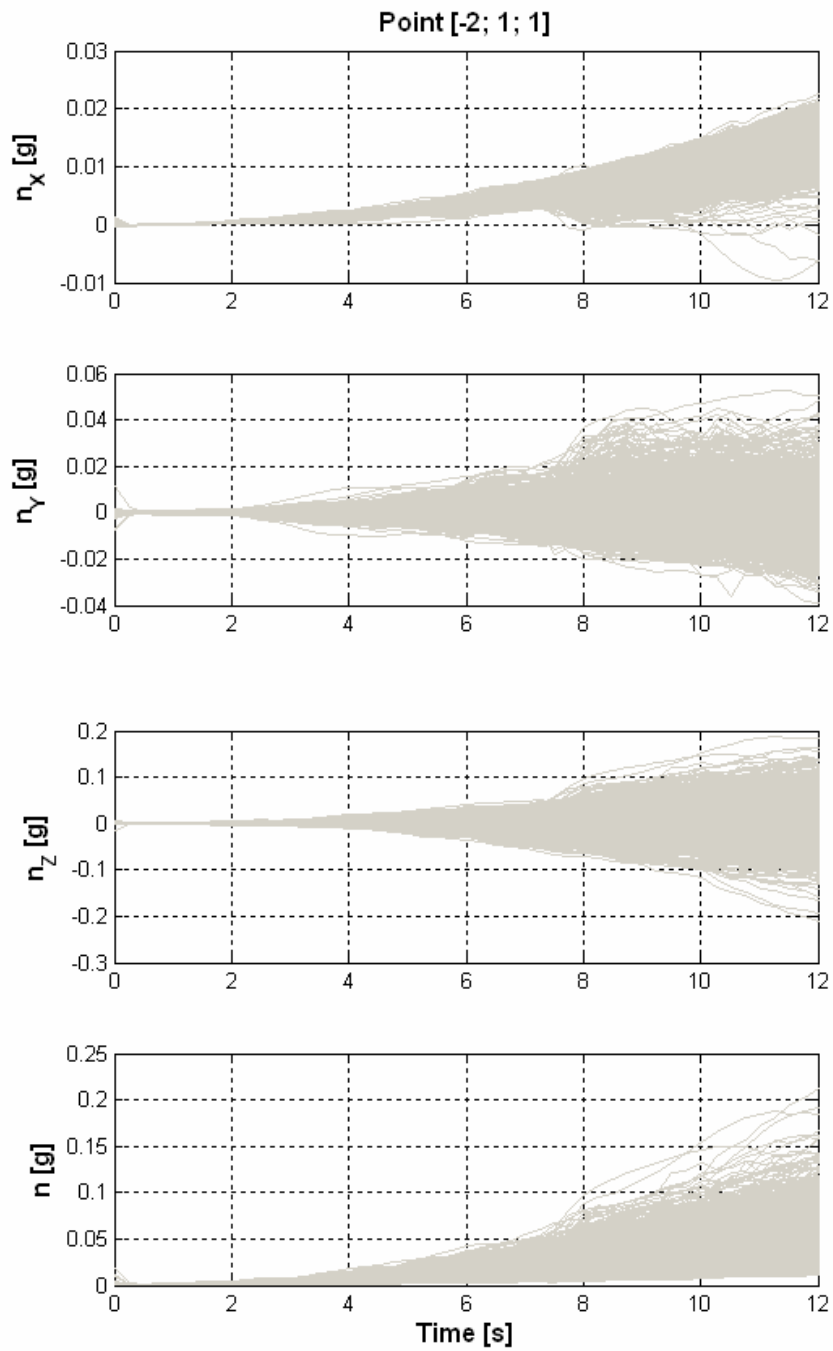
Fig. III - 30 – Load Factors in the Grid Point [-2, 1, 1] – Acceleration Phase
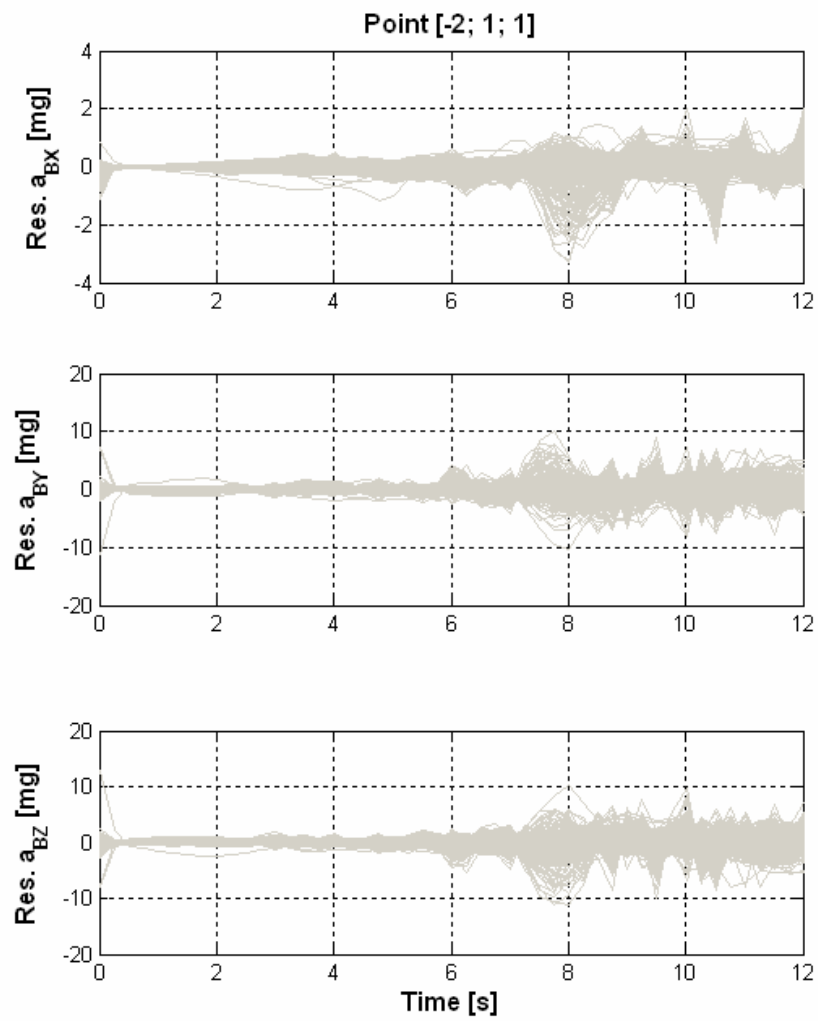
**Fig. III - 31– Residual Accelerations in the Grid Point [-2, 1, 1] – Acceleration
Phase**

III.4 Performance Improvement Strategies

In this paragraph there will be presented two different strategies that could improve the performance levels expressed by the results presented in the previous paragraph. They could be intended as guidelines for future research and development.

III.4.a *Mission Characteristics Modifications*

The first strategy proposed foresees a modification in the mission characteristics, and, specifically, it is based on the simple assumption that higher drop altitudes mean lower density values, and, as a consequence, lower levels of the aerodynamic forces that can stand for more time.

In Fig. III - 32 are shown the load factors realised in the cases of drop altitude = 24 km and 30 km; it is there represented only the acceleration phase.

It can be noticed how the low-gravity phase can last for almost 19 seconds in the case of 30 km drop.
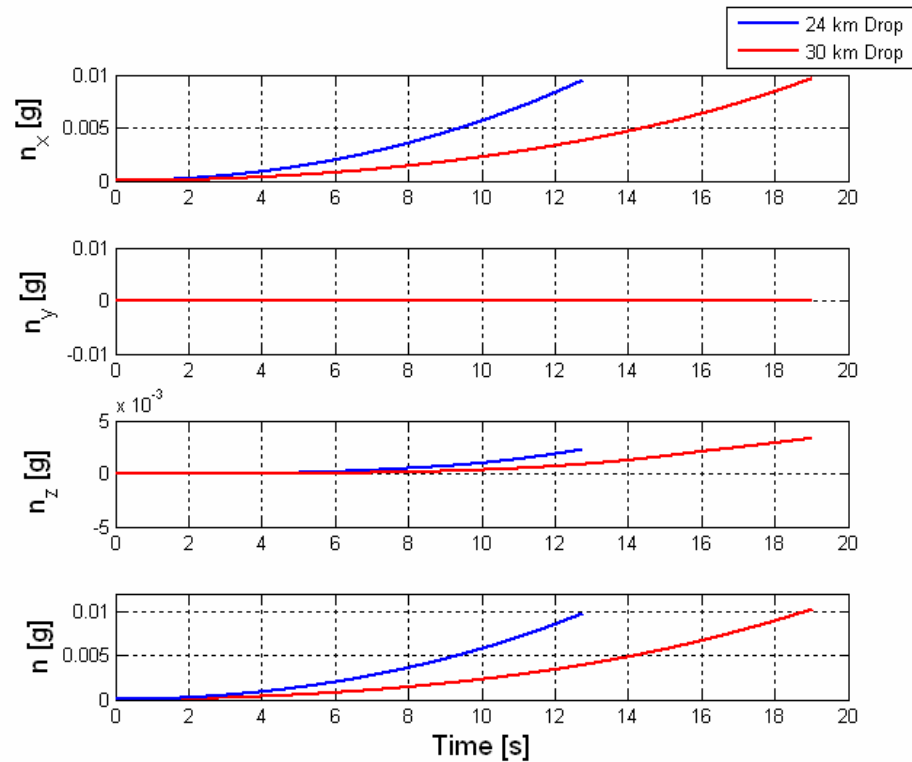
Fig. III - 32 – Load Factors for different Drop Altitudes

A relevant consideration that can be done is that the future missions planned in the USV program are already intended to be characterised by a drop altitude higher than the actual 20 km, so it can be assumed by now that they will be such to offer longer low-gravity intervals than the actual one.

III.4.b Specific Flight Control System Development

In order to improve the performance offered by FTB_1 as microgravity facility, a strategy that could be promising is based on the development of a proper Flight Control System Architecture. As stated in Chap. 1, in fact, the actually foreseen missions do not include microgravity objectives, and so the FCS now installed on board is deputed primarily to the stabilisation of the vehicle (that, as seen in Chap. 2 may be source of concern) and then to the realisation of the planned mission objectives, that basically consist in a tracking of the desired angle of attack reference.

The peculiarity that a system architecture should posses to ensure μg conditions can be summarised as follows:

1. Being the low-gravity condition that can be realised in the DTFT-type mission inherently associated wit low-density environment, the system should be equipped with actuators capable to be efficient also in this case, such for example the gas jets of a Reaction Control System.

2. The system should be provided of an Automation Logic capable to decide which actuation system to choose; this logic could

reasonably be based on the aerodynamic controllability properties, i.e. on the reaching of pre-fixed values for dynamic pressure and Mach number.

3. The flight control laws implemented on board could be based on advanced techniques developed to ensure robustness with respect to uncertainties and disturbances (ex H_∞[46]).

4. The experiment dynamics should be isolated from the vehicle ones by means of a proper system, that could be passive or active; in the last case, it could be based on advanced control techniques.

5. A further development in this sense could be the adoption of a "free-floating" methodology, in which the experiment can freely move into its bay, with no physical contact with the aircraft.

6. Being naturally based on a discrete-type logic (bang-off-bang), the Reaction Control System would require a discrete control methodology, such for example the Pulse Width Modulation, or, eventually, a non-linear strategy, based, for example, on the Sliding Mode approach[47]

7. The availability of different actuation systems could be further exploited by means of Control Allocation techniques, capable also of increase the fault-tolerance of the entire system[48].

8. Finally, robustness of the system with respect to the uncertainties could be further expanded giving to it the capability of autonomously generate its reference, always depending on the automation logic decision; this could reduce the effects of uncertainties in the initial state.

The block diagram of a Flight Control System Architecture of this kind is shown in the following Fig. III - 33.
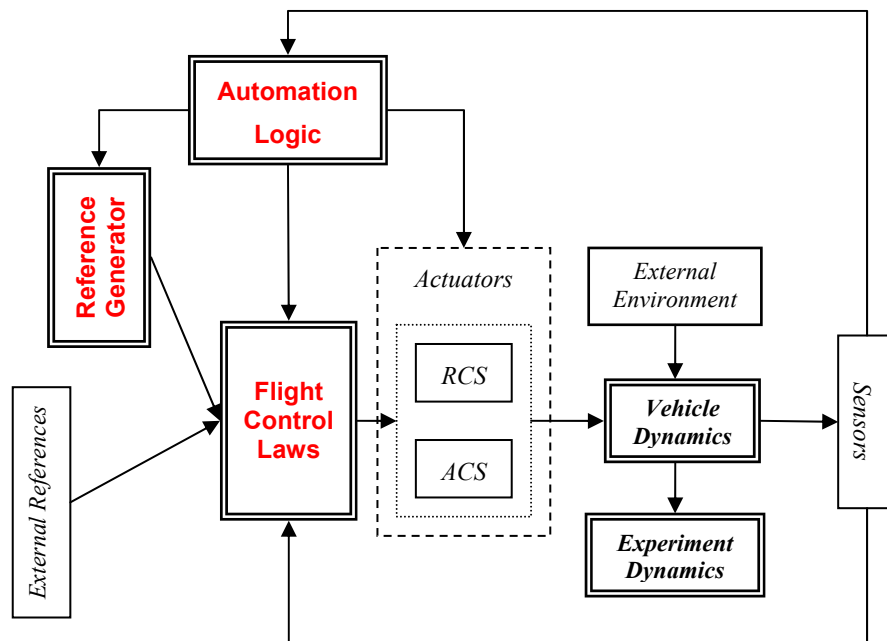
Fig. III - 33 – Example of Possible μg Flight Control System Architecture

III.5 The SRT Mission

In order to show the potentiality of the foreseen missions of the USV program to provide microgravitational flight condition, are here reported some preliminary characteristics of the Sub-Orbital Reentry Test mission.

The Sub-Orbital Reentry Test mission has been foreseen as an intermediate step before the execution of a complete orbital flight; its nominal profile can be summarised as it follows:

► The FTB vehicle is dropped by a stratospheric balloon at a height of about 35 km;

► The FTB vehicle, that in this configuration is rocket-propelled, starts its ascent and it climbs until it reaches an altitude of about 120 km;

► The FTB vehicle starts the re-entry phase of the mission.

An active constraint on the trajectory is the maximization the permanence time at values of the thermal flux > 650 kW/m^2, respecting the limits on the structural loads (< 12 g).

The trajectory available at the moment has been obtained by means of a point-of-mass model as the one of Eq. (II - 1); being neglected the rotational dynamics of the vehicle, it will not be possible to perform an analysis in points different from the centre of mass. In this kind of model, in fact, the rotational rates are supposed identically zero, and so all the corrective terms on the accelerations (i.e. the centripetal and the Coriolis contribute) are nil.

In the following figures are shown the angle of attack profile, the altitude vs. Mach trajectory, and the load factors profile along the nominal trajectory, that also in this case is supposed to be constrained in a longitudinal plane of motion.
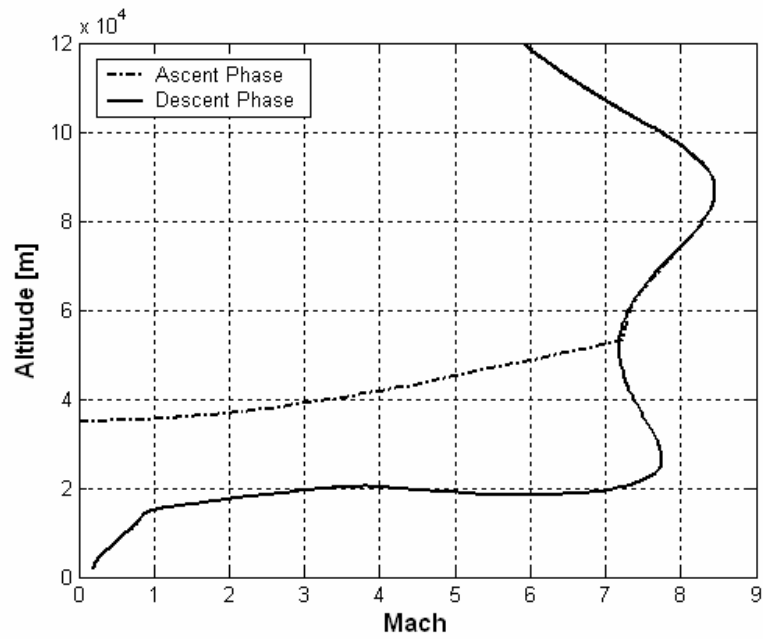
Fig. III - 34 – SRT Mission Altitude vs. Mach Diagram
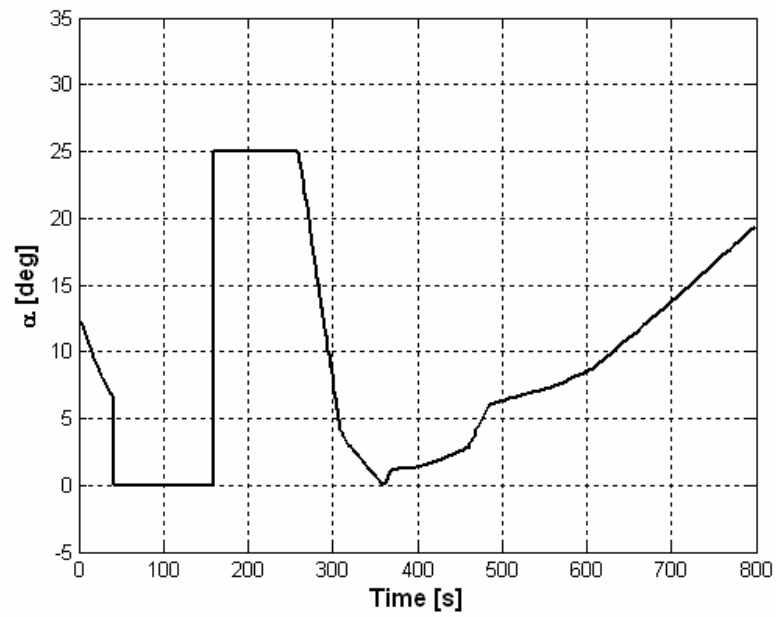
Fig. III - 35 – SRT Mission Amgle of Attack Profile
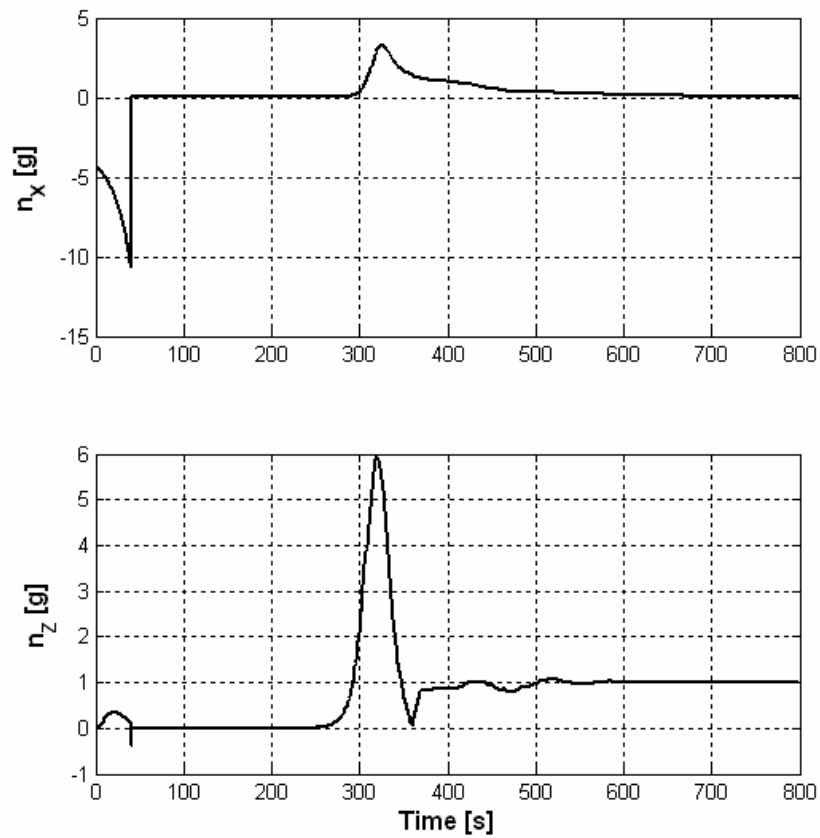
Fig. III - 36 – SRT Mission Load Factors Profiles

As it be seen from Fig. III - 36, the values of the load factors
characterising the mission are very high, especially n_X, as a consequence
of the presence of a propelled phase. Nevertheless, it is possible to notice,
in the same figure, the presence of a wide time interval in which the load
factors are near zero; this happens in correspondence of the coasting
phase of the trajectory, after the burning out of the rocket motor, when

the vehicle flies following a parabola, in approximately free-flight conditions, being the air density at the considered altitudes so low to nullify the aerodynamic forces. The situation is depicted in the following figures.
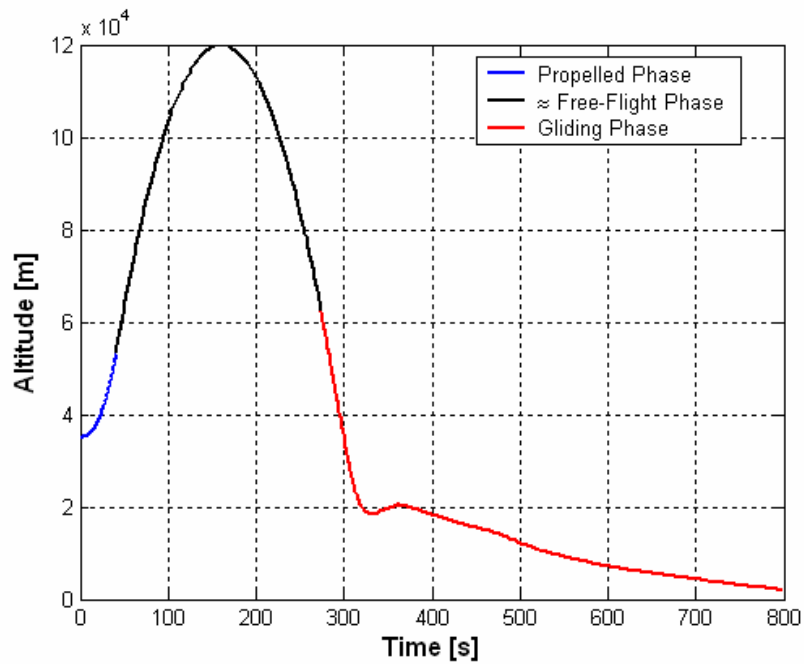
Fig. III - 37 – SRT Mission Altitude Profile – Various Phases Shown
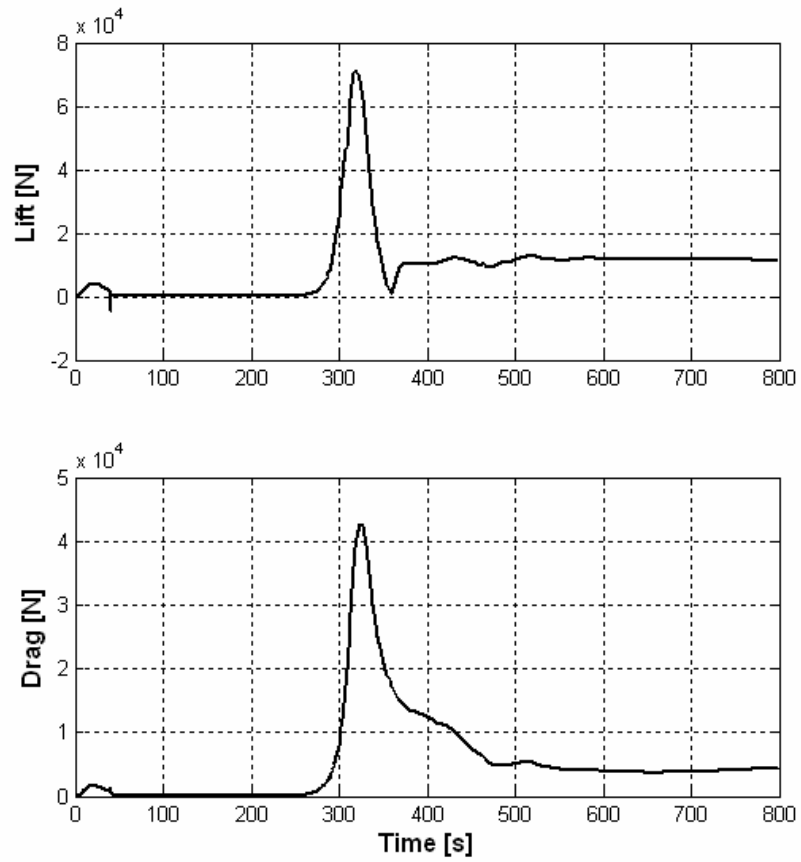
Fig. III - 38 – SRT Mission Aerodynamic Forces Profile

Focusing only on the ≈ free flight phase, we have:
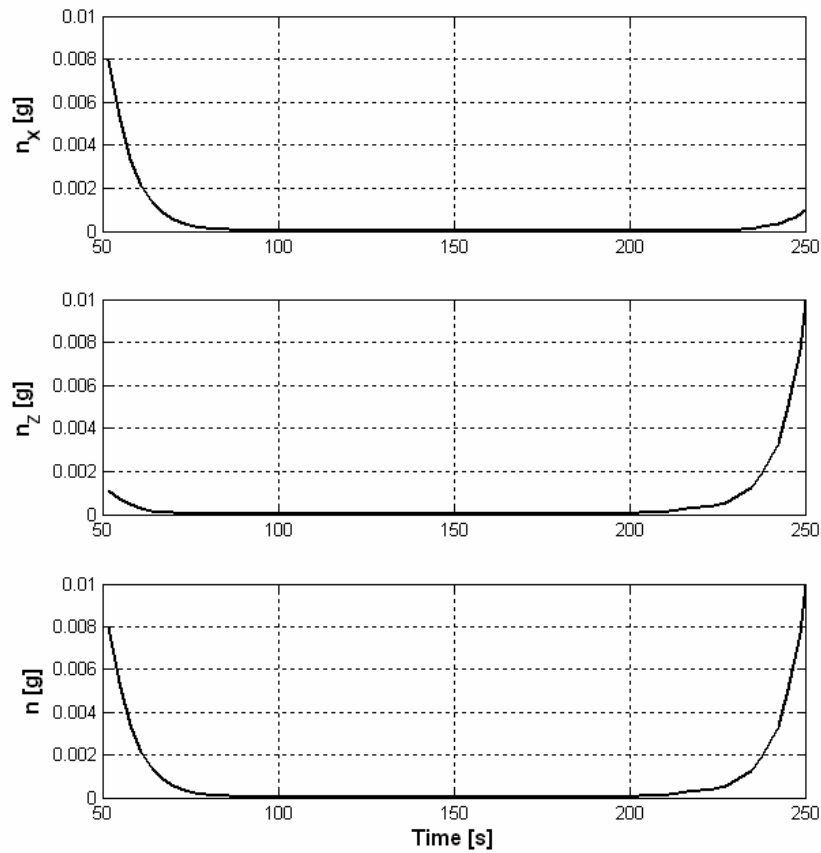
Fig. III - 39 – SRT Mission Load Factors Profiles – Free Flight Phase

In Fig. III - 39 $n = \sqrt{n_X^2 + n_Z^2}$.

As it can be seen, there is an interval of about 100 s when the load
factors are well below the mg level, this despite the fact that the SRT
mission, as the DTFT mission, has not been planned to be a
microgravitational flight.

III.6 Conclusions

The analyses of the nominal trajectory to be flown by the USV FTB_1 vehicle in order to perform its first DTFT mission, demonstrate that, although objectives of realisation of microgravity conditions are not foreseen, it exists a phase of about 10 s at the beginning of the trajectory where the load factors remain below 10^{-2} g, realising conditions that can be compared with the ones of a drop facility (see Table I - 1). However, the study of the effect of the possible disturbances, conducted by means of a Monte Carlo analysis, shows that in order to maintain this performance level, in hypotheses of high dispersion, i.e. considering as possible any turbulence level or wind intensity, operative modifications are needed. It appears as reasonable to suppose that, limiting the possibility of dispersion of the external environment, that means imposing more severe constraints on the launch conditions, and/or developing a flight control system capable to be efficient also in the initial acceleration phase, better performance can be achieved.

It should be remarked that this potentially useful mission phase is located at the beginning of the trajectory, and due to the fact that, after the drop from the balloon the aerodynamic actions are negligible, and so the vehicle is actually free-falling. It is so possible to drawn the

conclusion that every mission foreseen in the first part of the program, in which it is always planned the use of stratospheric balloons as carriers, will present the same kind of characteristic.

A brief view at the future possibility of the USV program has shown an interesting scenario in which, once considered the SRT mission, a low-gravity period of about 100 s and $n < 10^{-3}$ g seems to be achievable.

Finally, it is interesting to note that situations like the ones here considered, in which in the same mission are reached both low and high load factors, far from being a source of concern, has been identified as advantageous by the studies conducted by means of parabolic flights[26], because it allows to investigate phenomena related with the associated transition phase.

Conclusions

The objective of this thesis was the investigation of the dynamical environment, in terms of levels of acceleration reached, characterising the USV FTB_1 vehicle while executing its first DTFT mission, so to verify its exploitability as microgravity facility.

Firstly, it has been remarkably underlined that a complete knowledge of the microgravity environment in which an experiment takes place is fundamental for the correct interpretation of its results.

Then, an analysis of the characteristics of the FTB_1 vehicle has been performed.

It has been conducted using several instruments; first of all, an investigation of the trimmability and stability properties of the vehicle has been executed, considering a properly chosen flight envelope. It has pointed out that longitudinal stability could be a source of concern, so leading to the conclusion that a flight control system is strictly necessary for the execution of any kind of mission. A subsequent evaluation of the effect of aerodynamic uncertainties, carried out using a tailored

procedure, has not modified this result, but has evidenced the possibility of occurrence also of lateral-directional instabilities.

Finally, an analysis of the influence of a wide variety of disturbance has been performed, using a classical Monte Carlo procedure.

Once defined the possibility and potentiality of the available Flying Test Bed, an evaluation of the gravity level that it can ensure for the execution of microgravity experiments has been conducted.

It has shown that, although the DTFT mission has not been planned considering among its objectives the possibility to realise low-gravity conditions, in the initial "Acceleration Phase" of about 10 seconds it nominally could offer an acceleration level limited below $10^{-2}g$, that means that the microgravity capabilities of the Test Bed are similar to the ones of a drop tower. With respect to a drop facility, the USV present the peculiarity to offer high levels of gravity immediately after the low-gravity interval, and this characteristics has been identified as significant for different kind of research[26]. These results appear even more interesting considering that the "Acceleration Phase" of the trajectory is common to all the missions foreseen in the program for which a drop from balloon is planned, so there is the possibility to exploit the potentiality of the vehicle in the next future.

Considering the data from the Monte Carlo analysis, it can be concluded that these capabilities can be seriously affected by uncertainties like atmospheric disturbances or aerodynamic indeterminacies; so, in order to utilise the low-gravity interval, a focused mission strategy and an oriented flight control system are necessary.

Finally, the analysis of the kind of missions that could be foreseen in the future for the completion of the USV program has shown a promising widening of the possibility of the system, both in terms of gravity level and duration.

After the study conducted, it can be finally concluded that, the USV vehicle offers an interesting set of possibilities for the microgravity experimentation, that could be further expanded in the future by the development of focused mission strategies or research lines, like:

► Tailored trajectory optimisation: the microgravity phase could benefit, for example, from an higher drop altitude, that implies lower density. Preliminary evaluations have shown a low-gravity interval duration of about 13 s for a drop from 24 km, and about 20 s for a drop from 30 km;

► Analysis of the possibility to develop a peculiar flight control systems to be used in the low-gravity phase, and capable to

reject atmospheric disturbances. It has to be noted that, being the "Acceleration Phase" inherently characterised by the fact that the aerodynamic actions are negligible, a control system of this kind should be based on different actuation methodologies, such for example gas jets;

► Realisation of a proper isolation system; the load factor levels evidenced in this thesis, in fact, are characterising of the vehicle; it could result interesting to find a way to not transmit them to the passenger experiment. In this direction several possibility could be analysed, from the development of an active isolation system, using advanced control techniques, to the use of a "free falling" methodology, in which the experiment is free to fly inside the payload bay, with no physical contact with the aircraft.

Appendix 1

Reference Frames

In this Appendix are defined the main reference frames used in this thesis; further detail can be found in [49].

The **North-East-Down** (NED) **Reference Frame**, has the origin placed on the surface of the Earth, an axis directed as the local vertical, and the other two placed in the plane locally parallel to the Earth geoid, oriented along the South-North and West-East directions. For an aircraft, this reference frame can be considered an **Inertial Reference Frame** (IRF) when the characteristics of the mission performed are such to let the effects of the curvature of the planet and of its rotation to be neglected (for example, when the duration and/or extension of the flight is small). This approximation of "flat, non-moving earth" is considered valid for the DTFT mission.

The **Body Reference Frame** (BRF) X_B, Y_B, Z_B, is a right-handed triad, fixed with the vehicle, with the origin in its centre of mass. The longitudinal axis X_B is placed in the vehicle plane of symmetry, with its positive direction toward the nose, the Z_B axis is normal to X_B, placed in the same plane of symmetry, and direct positively downward, and the Y_B axis completes the triad, resulting positively oriented toward the right side.

The BRF and the IRF are shown in Fig. A.1 - 1. In the same figure are also indicated the components u, v, w of the velocity $\underline{V}$ of the vehicle, and p, q, r of the angular velocity $\underline{\omega}$, both with respect to the NED reference frame, and expressed in the body frame.
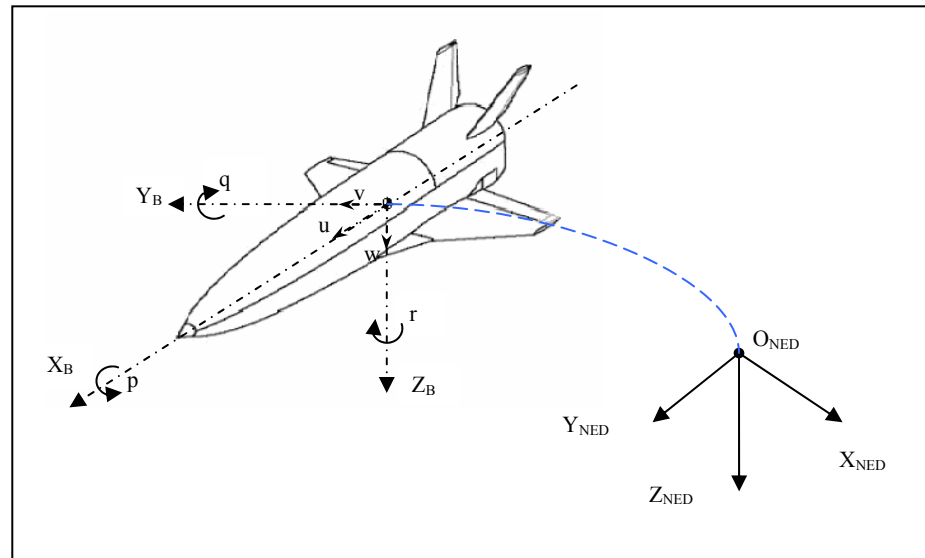
Fig. A.1 - 1 – Body Reference Frame and NED (Inertial) Reference Frame

The **Layout Reference Frame** (LRF) is the one in which the coordinates of every point of the vehicle are expressed (Fig. A.1 - 2).

For it:

► The origin O_{ly} is situated in the Nose of the vehicle

► The X_{ly} axis is perpendicular to the plane of base of the vehicle and oriented from the Nose towards such plan

► The Z_{ly} axis lies in the plan of symmetry of the vehicle and is directed towards upside (from the wings towards the vertical tail units)

► The Y_{ly} axis completes the triad in right-handed way
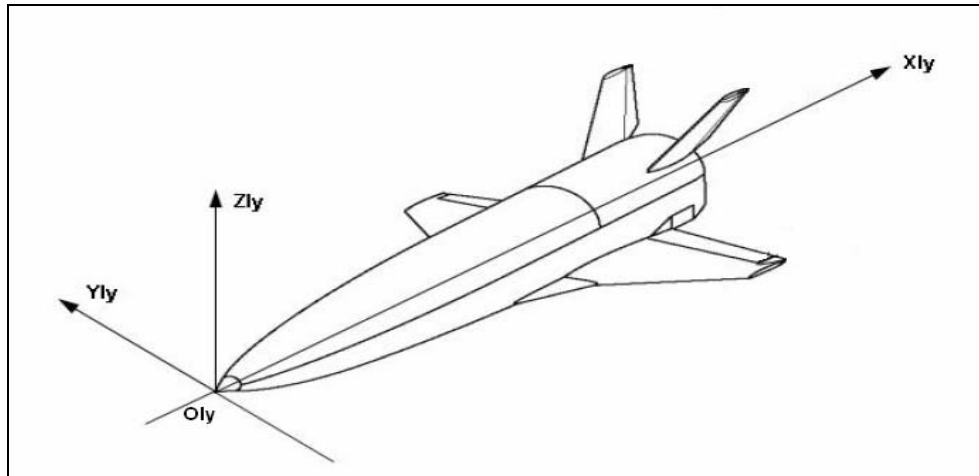
Fig. A.1 - 2 – Layut Reference Frame (LRF)

The attitude of the vehicle with respect to the NED reference frame is defined by the three **Euler Angles** ψ (yaw angle), θ (pitch angle) and Φ (roll angle). These angles define a rotation sequence that makes the NED reference frame coincident with the body one. The Euler angles are defined in Fig. A.1 - 3.
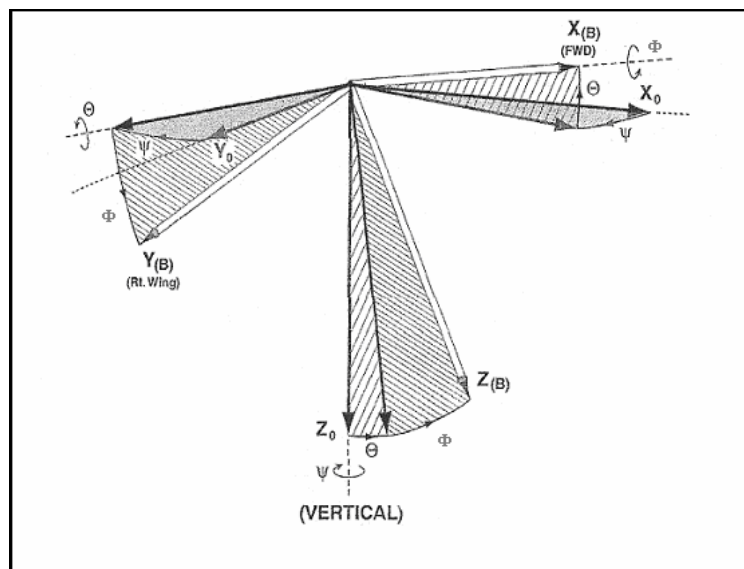
Fig. A.1 - 3 – Euler Angles

The **Angle of Attack** of the vehicle, α, is defined (Fig. A.1 - 4) as the angle between the projection of the direction of the free-stream velocity on the XZ plane of the body frame, and the X_B axis itself. It is defined as positive when the vehicle noses-up. The **Angle of Sideslip** β is defined (Fig. A.1 - 4) as the angle between the free-stream velocity and the XZ plane of the body frame. The sideslip angle is considered positive when the wind comes from the right side of the pilot.
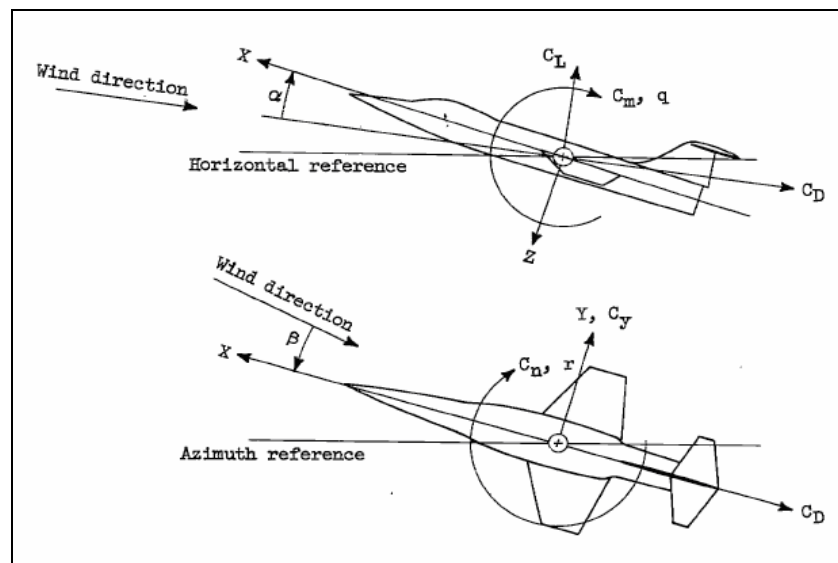
Fig. A.1 - 4 – Aerodynamic Angles of Incidence

Finally, once defined the body frame, and introduced the angles of incidence and of sideslip, it is possible to define the following reference frames (Fig. A.1 - 5):

► **Stability Reference Frame**, obtained from the body frame with a rotation of α around the Y_B axis;

► **Wind Reference Frame**, with the X_W axis directed oppositely to the free-stream velocity, the Z_W axis coincident with the Z_S axis, and the Y_W axis completing the triad in a right-handed way.
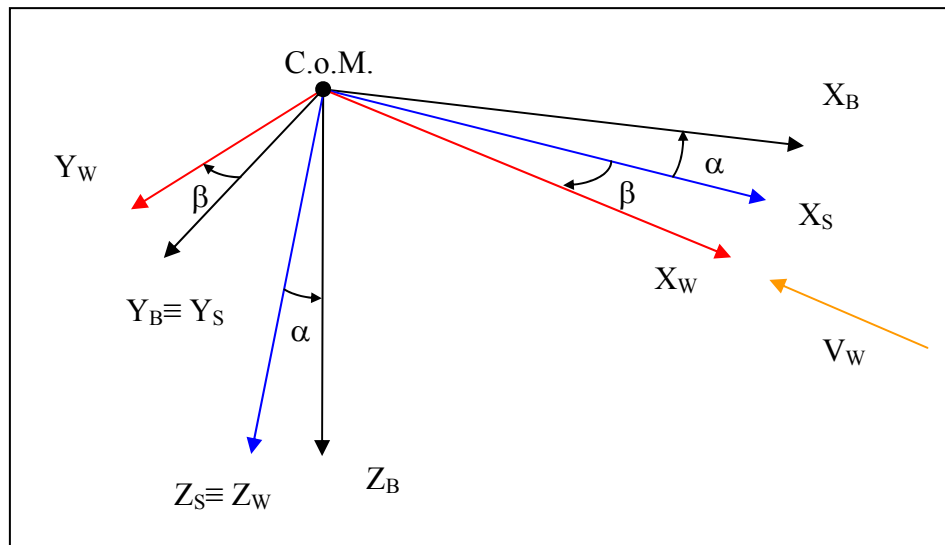
Fig. A.1 - 5 – Stability Reference Frame and Wind Reference Frame

In Fig. A.1 - 5, V_W indicates the direction of the free-stream velocity.

The last reference frames are important because:

► The longitudinal aerodynamic actions (Lift L, Drag D and pitching moment m) are defined in the stability reference frame, with L and D directed oppositely to the X_S and Z_S axes, respectively, while m is directed like the Y_S axis

► The lateral-directional aerodynamic action (Side force Y, rolling moment l and yawing moment n) are defined in the body reference frame, all directed like the body axis.

In every case the reduction pole for the calculus of the moments is the centre of mass of the vehicle.

Appendix 2

Equations of Motion

In this Appendix there will be indicated the equations of motion used for the description of the dynamics of the USV FTB_1 vehicle, both non-linear and linearised; further details can be found in [50].

A2.1 Non Linear Equations of Motion

The complete set of differential equations that describes the full, 6 D.o.F. dynamics of a flying vehicle is the following[51]:

$$\dot{x} = V \left[\begin{array}{c} \cos\alpha\cos\beta\cos\psi\cos\theta + \sin\beta\left(\cos\psi\sin\theta\sin\Phi - \sin\psi\cos\Phi\right) + \\ \sin\alpha\cos\beta\left(\cos\psi\sin\theta\cos\Phi + \sin\psi\sin\Phi\right) \end{array} \right] \tag{A.2 - 1}$$

$$\dot{y} = V \left[\begin{array}{c} \cos\alpha\cos\beta\sin\psi\cos\theta + \sin\beta\left(\sin\psi\sin\theta\sin\Phi + \cos\psi\cos\Phi\right) + \\ + \sin\alpha\cos\beta\left(\sin\psi\sin\theta\sin\Phi - \cos\psi\sin\Phi\right) \end{array} \right] \tag{A.2 - 2}$$

$$\dot{z} = -V\left(\cos\alpha\cos\beta\sin\theta - \sin\beta\cos\theta\sin\Phi - \sin\alpha\cos\beta\cos\theta\cos\Phi\right) \tag{A.2 - 3}$$

$$\dot{V} = -\frac{D_W}{m} + g \cdot \left(\begin{array}{c} \cos\Phi\cdot\cos\theta\cdot\sin\alpha\cdot\cos\beta + \sin\Phi\cdot\cos\theta\cdot\sin\beta - \\ -\sin\theta\cdot\cos\alpha\cdot\cos\beta \end{array} \right) \tag{A.2 - 4}$$

$$\dot{\alpha} = -\frac{L}{mV\cdot\cos\beta} + q - \tan\beta\cdot\left(p\cdot\cos\alpha + r\cdot\sin\alpha\right) +$$

$$+ \frac{g}{V\cos\beta}\cdot\left(\cos\Phi\cdot\cos\theta\cdot\cos\alpha + \sin\theta\cdot\sin\alpha\right) \tag{A.2 - 5}$$

$$\dot{\beta} = \frac{Y_W}{mV} + p \cdot \sin\alpha - r \cdot \cos\alpha + \frac{g}{V} \cdot \cos\beta \cdot \sin\Phi \cdot \cos\theta + \tag{A.2 - 6}$$

$$+ \frac{g \cdot \sin\beta}{V} \cdot (\cos\alpha \cdot \sin\theta - \sin\alpha \cdot \cos\Phi \cdot \cos\theta)$$

$$\dot{p} \cdot I_{xx} - \dot{q} \cdot I_{xy} - \dot{r} \cdot I_{xz} = 1 + qr \cdot (I_{yy} - I_{zz}) + (q^2 - r^2)I_{yz} + pq \cdot I_{xz} - \\ - rp \cdot I_{xy} \tag{A.2 - 7}$$

$$-\dot{p} \cdot I_{xy} + \dot{q} \cdot I_{yy} - \dot{r} \cdot I_{yz} = m + rp \cdot (I_{zz} - I_{xx}) + (r^2 - p^2)I_{xz} + qr \cdot I_{xy} - \\ - pq \cdot I_{yz} \tag{A.2 - 8}$$

$$-\dot{p} \cdot I_{xz} - \dot{q} \cdot I_{yz} + \dot{r} \cdot I_{zz} = n + pq \cdot (I_{xx} - I_{yy}) + (p^2 - q^2)I_{xy} + rp \cdot I_{yz} - \\ - qr \cdot I_{xz} \tag{A.2 - 9}$$

$$\dot{\Phi} = p + q \cdot \tan\theta \cdot \sin\Phi + r \cdot \tan\theta \cdot \cos\Phi \tag{A.2 - 10}$$

$$\dot{\theta} = q \cdot \cos\Phi - r \cdot \sin\Phi \tag{A.2 - 11}$$

$$\dot{\psi} = (q \cdot \sin\Phi + r \cdot \cos\Phi) \cdot \sec\theta \tag{A.2 - 12}$$

The aerodynamic actions are defined as:

► Lift: $\qquad L = \frac{1}{2}\rho V^2 C_L S$

► Drag: $\qquad D = \frac{1}{2}\rho V^2 C_D S$

► Side Force: $\qquad Y = \frac{1}{2}\rho V^2 C_Y S$

► Rolling Moment $\qquad l = \frac{1}{2}\rho V^2 C_l S b$

► Pitching Moment: $\qquad m = \frac{1}{2}\rho V^2 C_m S c$

► Yawing Moment: $\qquad n = \frac{1}{2}\rho V^2 C_n S b$

where:

$$C_L = f_1(M, Re, \alpha, \beta, \delta_{e\_right}, \delta_{e\_left}, \delta_{r\_right}, \delta_{r\_left}, \dot{\alpha}, q, X_{COM}, Y_{COM}, Z_{COM})$$
$$C_D = f_2(M, Re, \alpha, \beta, \delta_{e\_right}, \delta_{e\_left}, \delta_{r\_right}, \delta_{r\_left}, \dot{\alpha}, q, X_{COM}, Y_{COM}, Z_{COM})$$
$$C_m = f_3(M, Re, \alpha, \beta, \delta_{e\_right}, \delta_{e\_left}, \delta_{r\_right}, \delta_{r\_left}, \dot{\alpha}, q, X_{COM}, Y_{COM}, Z_{COM})$$

$$C_Y = f_4(M, Re, \alpha, \beta, \delta_{e\_right}, \delta_{e\_left}, \delta_{r\_right}, \delta_{r\_left}, p, r, X_{COM}, Y_{COM}, Z_{COM})$$
$$C_l = f_5(M, Re, \alpha, \beta, \delta_{e\_right}, \delta_{e\_left}, \delta_{r\_right}, \delta_{r\_left}, p, r, X_{COM}, Y_{COM}, Z_{COM})$$
$$C_n = f_6(M, Re, \alpha, \beta, \delta_{e\_right}, \delta_{e\_left}, \delta_{r\_right}, \delta_{r\_left}, p, r, X_{COM}, Y_{COM}, Z_{COM})$$

In the equations (A.2 - 1)… (A.2 - 12) there are twelve state variables:

$$\mathbf{x} = \begin{bmatrix} x & y & z & V & \alpha & \beta & p & q & r & \Phi & \theta & \psi \end{bmatrix}^T$$

and four controls:

$$\mathbf{u} = \begin{bmatrix} \delta_{e\_left} & \delta_{e\_right} & \delta_{r\_left} & \delta_{r\_right} \end{bmatrix}^T$$

Equations (A.2 - 1)… (A.2 - 12) are written considering as verified the hypotheses:

    a.   Flat, non-moving Earth;

    b.   Rigid vehicle, with constant mass properties;

    c.   Stationary atmosphere (no wind);

    d.   Absence of thrust;

    e.   Constant gravity acceleration;

    f.   Absence of gyroscopic effects due to rotating mass.

The equations can be divided in four groups:

• Eq. (A.2 - 1) … (A.2 - 3)	Spatial position equations; they give the position of the centre of mass of the vehicle, with respect to a NED (North-East-Down) reference frame, considered inertial

- Eq. (A.2 - 4) … (A.2 - 6)

  Velocity equations; they describe the translational dynamics of the vehicle, and are written with respect to a body reference frame, and expressed in spherical form

- Eq. (A.2 - 7) … (A.2 - 9)

  Angular velocity equations; they describe the rotational dynamics of the vehicle, and are written with respect to a body reference frame

- Eq. (A.2 - 10) … (A.2 - 12)

  Kinematical auxiliary equations

In Eq. (A.2 - 4) and (A.2 - 6)

are defined:

$\blacktriangleright$ $D_W \equiv$ Drag in wind axis $\qquad \rightarrow D_W = D\cos\beta$ - $Y\sin\beta$

$\blacktriangleright$ $Y_W \equiv$ Side Force in wind axes $\qquad \rightarrow Y_W = Y\cos\beta + D\sin\beta$

A2.2 Linearised Equations of Motion

In the linearization process, the non-linear equations describing the complete dynamics of the vehicle are substituted with the first term of their Taylor expansion:

$$f(x,u) = f(x_0,u_0) + \frac{\partial f}{\partial x}\bigg|_0 (x - x_0) + \frac{\partial f}{\partial u}\bigg|_0 (u - u_0) + HOT$$

$$\Downarrow$$

$$f(x,u) - f(x_0,u_0) = \Delta f = +\frac{\partial f}{\partial x}\bigg|_0 (x - x_0) + \frac{\partial f}{\partial u}\bigg|_0 (u - u_0) + HOT$$

the meaning of this expression is that, in proximity of the linearisation point (x_0,u_0) (i.e. in the hypothesis of small perturbations), the linear model approximates Δf, the variations of f with respect to the value assumed in the linearisation point itself.

The model chosen for the aerodynamic coefficients is a linaerisation of the one presented in § A2.1 :

$$C_L = C_{L0} + C_{L\alpha}\alpha + C_{L\beta}\beta + C_{L\dot{\alpha}}\frac{\dot{\alpha}\cdot c}{2\cdot V} + C_{Lq}\frac{q\cdot c}{2\cdot V} + C_{LV}V + C_{L\delta_e}\delta_e \qquad \textbf{(A.2 - 13)}$$

$$C_D = C_{D0} + C_{D\alpha}\alpha + C_{D\beta}\beta + C_{DV}V + C_{D\delta_e}\delta_e + C_{D\delta_r}\delta_r \qquad \textbf{(A.2 - 14)}$$

$$C_Y = C_{Y\alpha}\alpha + C_{Y\beta}\beta + C_{Yp}\frac{p\cdot b}{2\cdot V} + C_{Yr}\frac{r\cdot b}{2\cdot V} + C_{YV}V + C_{Y\delta_a}\delta_a + C_{Y\delta_r}\delta_r \qquad \textbf{(A.2 - 15)}$$

$$C_l = C_{l\alpha}\alpha + C_{l\beta}\beta + C_{lp}\frac{p\cdot b}{2\cdot V} + C_{lr}\frac{r\cdot b}{2\cdot V} + C_{lV}V + C_{l\delta_a}\delta_a + C_{l\delta_r}\delta_r \qquad \textbf{(A.2 - 16)}$$

$$C_m = C_{m0} + C_{m\alpha}\alpha + C_{m\beta}\beta + C_{m\dot{\alpha}}\frac{\dot{\alpha}\cdot c}{2\cdot V} + C_{mq}\frac{q\cdot c}{2\cdot V} + C_{mV}V + C_{m\delta_e}\delta_e$$
$$+ C_{m\delta_r}\delta_r \qquad \textbf{(A.2 - 17)}$$

$$C_n = C_{n\alpha}\alpha + C_{n\beta}\beta + C_{np}\frac{p\cdot b}{2\cdot V} + C_{nr}\frac{r\cdot b}{2\cdot V} + C_{nV}V + C_{n\delta_a}\delta_a + C_{n\delta_r}\delta_r \qquad \textbf{(A.2 - 18)}$$

All the terms that are not expressed in Eq. (A.2 - 13)… (A.2 - 18) are considered negligible with respect to the others.

It is worth noting that in the definition of the aerodynamic coefficients for the 6 D.o.F. model, in the previous paragraph, there have been used the deflection of the control surfaces, considered individually (δ_{e_left}, δ_{e_right} ecc.); from these parameters it is possible to reconstruct a symmetrical elevon deflection and an antisymmetrical aileron deflection (used in the linearisation) as:

$$\delta_e = \frac{\delta_{e\_left} + \delta_{e\_right}}{2}$$

$$\delta_a = \frac{\delta_{e\_left} - \delta_{e\_right}}{2}$$

with the convention that an aileron deflection is considered as positive when it produces positive rolling moment.

About the rudders, in this model they are supposed to work only in symmetrical way, i.e:

$$\delta_{r\_left} = \delta_{r\_right} = \delta_r$$

Now, the non linear model to be linearised will be obtained from a linearisation process executed on modified version of the set of equations (A.2 - 1) … (A.2 - 12), i.e. :

$$\dot{V} = -\frac{D_W}{m} + g \cdot \left(\begin{array}{l} \cos\Phi \cdot \cos\theta \cdot \sin\alpha \cdot \cos\beta + \sin\Phi \cdot \cos\theta \cdot \sin\beta - \\ - \sin\theta \cdot \cos\alpha \cdot \cos\beta \end{array} \right) \qquad \text{(A.2 - 19)}$$

$$\dot{\alpha} = -\frac{L}{mV \cdot \cos\beta} + q - \tan\beta \cdot (p \cdot \cos\alpha + r \cdot \sin\alpha) +$$

$$+ \frac{g}{V\cos\beta} \cdot (\cos\Phi \cdot \cos\theta \cdot \cos\alpha + \sin\theta \cdot \sin\alpha) \qquad \text{(A.2 - 20)}$$

$$\dot{\beta} = \frac{Y_W}{mV} + p \cdot \sin\alpha - r \cdot \cos\alpha + \frac{g}{V} \cdot \cos\beta \cdot \sin\Phi \cdot \cos\theta +$$

$$+ \frac{g \cdot \sin\beta}{V} \cdot (\cos\alpha \cdot \sin\theta - \sin\alpha \cdot \cos\Phi \cdot \cos\theta) \qquad \text{(A.2 - 21)}$$

$$\dot{p} \cdot I_{xx} - \dot{r} \cdot I_{xz} = 1 + qr \cdot (I_{yy} - I_{zz}) + pq \cdot I_{xz} \qquad \text{(A.2 - 22)}$$

$$\dot{q} \cdot I_{yy} = m + rp \cdot (I_{zz} - I_{xx}) + (r^2 - p^2) \cdot I_{xz} \qquad \text{(A.2 - 23)}$$

$$-\dot{p} \cdot I_{xz} + \dot{r} \cdot I_{zz} = n + pq \cdot (I_{xx} - I_{yy}) - qr \cdot I_{xz} \qquad \text{(A.2 - 24)}$$

$$\dot{\Phi} = p + q \cdot \tan\theta \cdot \sin\Phi + r \cdot \tan\theta \cdot \cos\Phi \qquad \text{(A.2 - 25)}$$

$$\dot{\theta} = q \cdot \cos\Phi - r \cdot \sin\Phi \qquad \text{(A.2 - 26)}$$

Here, we have neglected the navigation equations, i.e. the spatial position and the ψ equations, furthermore, we have considered as valid the following hypothesis:

g. Negligibility of the I_{xy} and I_{yz} products of inertia, considered in a body reference frame.

These equations can be further modified by:

► Regrouping separately the longitudinal and lateral-directional variables;

► Decoupling the equations in $\dot{p}$ and $\dot{r}$;

► Isolating the $\dot{\alpha}$ terms related to L and m; this is made possible by writing the lift and moment coefficients in the form:

$$C_L = \overline{C}_L + \hat{C}_{L\dot{\alpha}}\dot{\alpha}, \quad \text{with} \quad \hat{C}_{L\dot{\alpha}} = C_{L\dot{\alpha}}\frac{c}{2V}, \quad \Rightarrow \quad \overline{L} = q_\infty \overline{C}_L S$$

$$C_m = \overline{C}_m + \hat{C}_{m\dot{\alpha}}\dot{\alpha}, \quad \text{with} \quad \hat{C}_{m\dot{\alpha}} = C_{m\dot{\alpha}}\frac{c}{2V}, \quad \Rightarrow \quad \overline{m} = q_\infty \overline{C}_m Sc$$

It is so possible to obtain the following set of equations:

$$\dot{V} = -\frac{D_W}{m} + g \cdot \begin{pmatrix} \cos\Phi \cdot \cos\theta \cdot \sin\alpha \cdot \cos\beta + \sin\Phi \cdot \cos\theta \cdot \sin\beta - \\ -\sin\theta \cdot \cos\alpha \cdot \cos\beta \end{pmatrix} \qquad \textbf{(A.2 - 27)}$$

$$\dot{\alpha}\left(V + \frac{q_\infty S\hat{C}_{L\dot{\alpha}}}{m\cos\beta}\right) = -\frac{\overline{L}}{m \cdot \cos\beta} + qV - V \cdot \tan\beta \cdot (p \cdot \cos\alpha + r \cdot \sin\alpha) + \qquad \textbf{(A.2 - 28)}$$

$$\frac{g}{\cos\beta} \cdot (\cos\Phi \cdot \cos\theta \cdot \cos\alpha + \sin\theta \cdot \sin\alpha)$$

$$\dot{q} - \frac{q_\infty Sc\hat{C}_{m\dot{\alpha}}\dot{\alpha}}{I_{yy}} = \frac{\overline{m}}{I_{yy}} + rp \cdot \left(\frac{I_{zz} - I_{xx}}{I_{yy}}\right) + \left(r^2 - p^2\right) \cdot \frac{I_{xz}}{I_{yy}} \qquad \textbf{(A.2 - 29)}$$

$$\dot{\theta} = q \cdot \cos\Phi - r \cdot \sin\Phi \qquad \textbf{(A.2 - 30)}$$

$$V\dot{\beta} = \frac{Y_W}{m} + pV \cdot \sin\alpha - rV \cdot \cos\alpha + g \cdot \cos\beta \cdot \sin\Phi \cdot \cos\theta +$$
$$g \cdot \sin\beta \cdot (\cos\alpha \cdot \sin\theta - \sin\alpha \cdot \cos\Phi \cdot \cos\theta)$$

(A.2 - 31)

$$\dot{p} = (c_1 r + c_2 p)q + c_3 l + c_4 n$$

(A.2 - 32)

$$\dot{r} = (c_5 p - c_2 r)q + c_4 l + c_6 n$$

(A.2 - 33)

$$\dot{\Phi} = p + q \cdot \tan\theta \cdot \sin\Phi + r \cdot \tan\theta \cdot \cos\Phi$$

(A.2 - 34)

where there have been introduced the following coefficients[52]:

$$\Gamma c_1 = (I_{yy} - I_{zz}) \cdot I_{zz} - I_{xz}^2$$
$$\Gamma c_2 = (I_{xx} - I_{yy} + I_{zz}) \cdot I_{xz}$$
$$\Gamma c_3 = I_{zz}$$
$$\Gamma c_4 = I_{xz}$$
$$\Gamma c_5 = I_{xx}(I_{xx} - I_{yy}) + I_{xz}^2$$
$$\Gamma c_6 = I_{xx}$$
$$\Gamma = I_{xx} I_{zz} - I_{xz}^2$$

In these equations there are eight state variables:

$$\mathbf{x} = \begin{bmatrix} V & \alpha & q & \theta & \beta & p & r & \Phi \end{bmatrix}^T$$

and three controls:

$$\mathbf{u} = \begin{bmatrix} \delta_e & \delta_a & \delta_r \end{bmatrix}^T$$

Eq. (A.2 - 27) ... (A.2 - 34) are going to be linearised. It is possible to identify more than one condition in which the linearization process can be executed[50]; here are reported only the results of the case when:

$$V = V_e \neq 0, \ \alpha = \alpha_e \neq 0, \ \theta = \theta_e \neq 0$$
$$\beta_e = 0, \ \Phi_e = 0$$
$$p_e = q_e = r_e = 0$$

and for the command surfaces we have:

$$\delta e_e = \delta e_{TRIM}, \ \delta a_e = 0, \ \delta r_e = 0$$

In practice, is it here considered the case in witch the motion of the vehicle is constrained in its longitudinal plane of symmetry; in this conditions, the following hypothesis can be made:

► The derivatives of the actions lying out of the symmetry plane of the aircraft (Y, l, n) with respect to symmetrical variables (V, α, q, θ, δ_e) are equal to zero.

► The derivatives of the actions lying in the symmetry plane of the aircraft (L, D, m) with respect to non-symmetrical variables (β, p, r, Φ, δ_a, δ_r) are equal to zero.

The linearised model is in the form:

$$\mathbf{E\dot{x} = Ax + Bu} \qquad \text{(A.2 - 35)}$$

With:

$$\mathbf{x} = \begin{bmatrix} V & \alpha & q & \theta & \beta & p & r & \Phi \end{bmatrix}^{T} \ ; \ \mathbf{u} = \begin{bmatrix} \delta_e & \delta_a & \delta_r \end{bmatrix}^{T}$$

As a consequence of the characteristics of the considered linearization point, such to present equal to 0 all the non-symmetrical variables, it will be obtained a decoupling between the longitudinal and lateral-directional dynamics.

It is so possible to identify a longitudinal and lateral-directional linearised model.

Longitudinal Linearised Model

$$E_{LON} = \begin{bmatrix} 1 & 0 & 0 & 0 \\ 0 & V_e + \dfrac{q_\infty S}{m}\hat{C}_{L\dot{\alpha}} & 0 & 0 \\ 0 & -\dfrac{q_\infty Sc\hat{C}_{m\dot{\alpha}}}{I_{yy}} & 1 & 0 \\ 0 & 0 & 0 & 1 \end{bmatrix}$$

(A.2 - 36)

$$A_{LON} = \begin{bmatrix} -\dfrac{q_\infty S}{mV_e}\left(\hat{C}_{DV} + 2\cdot C_{D_e}\right) & -\dfrac{q_\infty S}{m}C_{D\alpha} + g\cos\gamma_e & 0 & -g\cos\gamma_e \\ -\dfrac{q_\infty S}{mV_e}\left(\hat{C}_{LV} + 2\cdot C_{L_e}\right) & -\dfrac{q_\infty S}{m}C_{L\alpha} + g\sin\gamma_e & V - \dfrac{q_\infty S}{m}\hat{C}_{Lq} & -g\sin\gamma_e \\ \dfrac{q_\infty Sc}{I_{yy}}C_{mV} & \dfrac{q_\infty Sc}{I_{yy}}C_{m\alpha} & \dfrac{q_\infty Sc}{I_{yy}}\hat{C}_{mq} & 0 \\ 0 & 0 & 1 & 0 \end{bmatrix}$$

(A.2 - 37)

$$B_{LON} = \begin{bmatrix} -\dfrac{q_\infty S}{m}C_{D\delta_e} \\ -\dfrac{q_\infty S}{m}C_{L\delta_e} \\ \dfrac{q_\infty Sc}{I_{yy}}C_{m\delta_e} \\ 0 \end{bmatrix}$$

(A.2 - 38)

Lateral-Directional Linearised Model

$$E_{LAT} = I_{4x4}$$

$$\text{(A.2 - 39)}$$

$$A_{LAT} = \begin{bmatrix} \dfrac{q_\infty S}{mV_e}\left(C_{De} + C_{Y\beta}\right) + \dfrac{g}{V_e}\sin\gamma_e & \dfrac{q_\infty S}{mV_e}\hat{C}_{Yp} + \sin\alpha_e & \dfrac{q_\infty S}{mV_e}\hat{C}_{Yr} - \cos\alpha_e & \dfrac{g}{V_e}\cos\theta_e \\ q_\infty Sb\left(c_3 C_{l\beta} + c_4 C_{n\beta}\right) & q_\infty Sb\left(c_3 \widehat{C}_{lp} + c_4 \hat{C}_{np}\right) & q_\infty Sb\left(c_3 \widehat{C}_{lr} + c_4 \hat{C}_{nr}\right) & 0 \\ q_\infty Sb\left(c_4 C_{l\beta} + c_6 C_{n\beta}\right) & q_\infty Sb\left(c_4 \widehat{C}_{lp} + c_6 \hat{C}_{np}\right) & q_\infty Sb\left(c_4 \widehat{C}_{lr} + c_6 \hat{C}_{nr}\right) & 0 \\ 0 & 1 & \tan\theta_e & 0 \end{bmatrix}$$

$$\text{(A.2 - 40)}$$

$$B_{LAT} = \begin{bmatrix} \dfrac{q_\infty S}{mV_e}C_{Y\delta_a} & \dfrac{q_\infty S}{mV_e}C_{Y\delta_r} \\ q_\infty Sb\left(c_3 C_{l\delta_a} + c_4 C_{n\delta_a}\right) & q_\infty Sb\left(c_3 C_{l\delta_r} + c_4 C_{n\delta_r}\right) \\ q_\infty Sb\left(c_4 C_{l\delta_a} + c_6 C_{n\delta_a}\right) & q_\infty Sb\left(c_4 C_{l\delta_r} + c_6 C_{n\delta_r}\right) \\ 0 & 0 \end{bmatrix}$$

$$\text{(A.2 - 41)}$$

Appendix 3

USV FTB_1 Aerodynamic Uncertainties Tables

		Mach								
		0.1	0.5	0.7	0.8	0.9	0.94	1	1.13	1.4
C_{L0}	(-)	0.034	0.034	0.0255	0.0255	0.034	0.034	0.034	0.0425	0.0425
$C_{L\alpha}(+)$	(1/deg)	0.0017				0.00255		0.0034	0.0034	0.0034
$C_{L\alpha}(-)$	(1/deg)	0.0017				0.00255		0.00255	0.00255	0.00255
$C_{L\delta e}$	(1/deg)	0.0017								
$C_{L\alpha dot}$	%	80							N.A.	N.A.
C_{Lq}	%	80							N.A.	N.A.
$C_{D0}(+)$	(-)	0.01045	0.01045	0.009405	0.0120175	0.01596	0.01596	0.01596	0.0171	0.01824
$C_{D0}(-)$	(-)	0.0171	0.0171	0.01596	0.020995	0.0247	0.0266	0.0266	0.02793	0.02926
$C_{D\alpha2}$	$(1/deg^2)$	0.00007125	0.00007125	0.0000475	0.0000475	0.0000475	0.000057	0.000057	0.000057	0.000057
$C_{D\delta e}$	(1/deg)	0.000285								
$C_{D\delta r}$	(1/deg)	0.000095							N.A.	N.A.
C_{m0}	(-)	0.036	0.036	0.027	0.027	0.0405	0.0405	0.0405	0.045	0.045
$C_{m\alpha}(+)$	(1/deg)	0.00189	0.00189	0.001476	0.001476	0.00189	0.002322	0.002322	0.00243	0.00243
$C_{m\alpha}(-)$	(1/deg)	0.00189	0.00189	0.001476	0.001476	0.00189	0.002322	0.003222	0.00333	0.00333
$C_{m\delta e}(+)$	(1/deg)	0.00225								
$C_{m\delta e}(-)$	(1/deg)	0.00315								
$C_{m\delta r}$	(1/deg)	0.00036							N.A.	N.A.
$C_{m\alpha dot}$	%	80							N.A.	N.A.
C_{mq}	%	80							N.A.	N.A.
$C_{Y\beta}$	(1/deg)	0.0041	0.0041	0.0051	0.0061	0.0061	0.0061	0.0061	N.A.	N.A.
$C_{Y\delta a}$	(1/deg)	0.0008	0.0008	0.0008	0.0011	0.0013	0.0015	0.0015	N.A.	N.A.
$C_{Y\delta r}$	(1/deg)	0.001	0.001	0.001	0.0013	0.0016	0.0016	0.0016	N.A.	N.A.
C_{Yp}	%	80							N.A.	N.A.
C_{Yr}	%	80							N.A.	N.A.
$C_{n\beta}(+)$	(1/deg)	0.0021	0.0021	0.0016	0.0016	0.0016	0.0016	0.0016	N.A.	N.A.
$C_{n\beta}(-)$	(1/deg)	0.0021	0.0021	0.0011	0.0011	0.0011	0.0011	0.0016	N.A.	N.A.
$C_{n\delta a}$	(1/deg)	0.0004	0.0004	0.0004	0.0005	0.0005	0.00055	0.00055	N.A.	N.A.
$C_{n\delta r}$	(1/deg)	0.0006							N.A.	N.A.
C_{np}	%	80							N.A.	N.A.
C_{nr}	%	80							N.A.	N.A.
$C_{l\beta}$	(1/deg)	0.00126							N.A.	N.A.
$C_{l\delta a}$	(1/deg)	0.0006	0.0006	0.0006	0.00075	0.0009	0.0009	0.0009	N.A.	N.A.
$C_{l\delta r}$	(1/deg)	0.0002	0.0002	0.0002	0.00025	0.0003	0.0003	0.0003	N.A.	N.A.
C_{lp}	%	80							N.A.	N.A.
C_{lr}	%	80							N.A.	N.A.

Table A.3 - 1 – USV FTB_1 Aerodynamic Uncertainties

		Mach								
		0.1	0.5	0.7	0.8	0.9	0.94	1	1.13	1.4
C_{L0}	(-)	0.04	0.04	0.03	0.03	0.04	0.04	0.04	0.05	0.05
$C_{L\alpha}$ (+)	(1/deg)	0.002				0.003		0.004	0.004	0.004
$C_{L\alpha}$ (-)	(1/deg)	0.002				0.003		0.003	0.003	0.003
$C_{L\delta e}$	(1/deg)	0.002								.
$C_{L\alpha dot}$	%	80							N.A.	N.A.
C_{Lq}	%	80							N.A.	N.A.
C_{D0} (+)	(-)	0.011	0.011	0.0099	0.01265	0.0168	0.0168	0.0168	0.018	0.0192
C_{D0} (-)	(-)	0.018	0.018	0.0168	0.0221	0.026	0.028	0.028	0.029	0.031
$C_{D\alpha2}$	(1/deg²)	0.000075	0.000075	0.00005	0.00005	0.00005	0.00006	0.00006	0.00006	0.00006
$C_{D\delta e}$	(1/deg)	0.0003								
$C_{D\delta r}$	(1/deg)	0.0001							N.A.	N.A.
C_{m0}	(-)	0.04	0.04	0.03	0.03	0.045	0.045	0.045	0.05	0.05
$C_{m\alpha}$ (+)	(1/deg)	0.0021	0.0021	0.00164	0.00164	0.0021	0.00258	0.00258	0.0027	0.0027
$C_{m\alpha}$ (-)	(1/deg)	0.0021	0.0021	0.00164	0.00164	0.0021	0.00258	0.00358	0.0037	0.0037
$C_{m\delta e}$ (+)	(1/deg)	0.0025								
$C_{m\delta e}$ (-)	(1/deg)	0.0035								
$C_{m\delta r}$	(1/deg)	0.0004							N.A.	N.A.
$C_{m\alpha dot}$	%	80							N.A.	N.A.
C_{mq}	%	80							N.A.	N.A.
$C_{Y\beta}$	(1/deg)	0.0041	0.0041	0.0051	0.0061	0.0061	0.0061	0.0061	N.A.	N.A.
$C_{Y\delta a}$	(1/deg)	0.0008	0.0008	0.0008	0.0011	0.0013	0.0015	0.0015	N.A.	N.A.
$C_{Y\delta r}$	(1/deg)	0.001	0.001	0.001	0.0013	0.0016	0.0016	0.0016	N.A.	N.A.
C_{Yp}	%	80							N.A.	N.A.
C_{Yr}	%	80							N.A.	N.A.
$C_{n\beta}$ (+)	(1/deg)	0.0021	0.0021	0.0016	0.0016	0.0016	0.0016	0.0016	N.A.	N.A.
$C_{n\beta}$ (−)	(1/deg)	0.0021	0.0021	0.0011	0.0011	0.0011	0.0011	0.0016	N.A.	N.A.
$C_{n\delta a}$	(1/deg)	0.0004	0.0004	0.0004	0.0005	0.0005	0.00055	0.00055	N.A.	N.A.
$C_{n\delta r}$	(1/deg)	0.0006							N.A.	N.A.
C_{np}	%	80							N.A.	N.A.
C_{nr}	%	80							N.A.	N.A.
$C_{l\beta}$	(1/deg)	0.00126							N.A.	N.A.
$C_{l\delta a}$	(1/deg)	0.0006	0.0006	0.0006	0.00075	0.0009	0.0009	0.0009	N.A.	N.A.
$C_{l\delta r}$	(1/deg)	0.0002	0.0002	0.0002	0.00025	0.0003	0.0003	0.0003	N.A.	N.A.
C_{lp}	%	80							N.A.	N.A.
C_{lr}	%	80							N.A.	N.A.

Table A.3 - 2 – USV FTB_1 Aerodynamic Uncertainties – Isolated Case

The values indicated in the tables have to be intended as 2-σ conditions.

As it can be noticed, the uncertainties are supplied in two different versions: one, indicated in Table A.3 - 1, that have to be used when it is necessary to perform the build up process to obtain the aerodynamic coefficients (see § II.2.c.3), and one, indicated in Table A.3 - 2 that have to be used when the aerodynamic coefficients are considered one by one.

Moreover, as it can be seen, the lateral-directional uncertainty dataset is limited below M = 1. This is true also for the nominal aerodatabase; the values of the coefficients above M = 1 are obtained performing linear extrapolation.

References

[1]. Thomas, V.A., Prasad, N.S., et alii; **Microgravity Research Platforms: a Study**; *Current Science*, Vol. 79, N° 3, August 2000, pp. 336-340.

[2]. Uri, J.J., Cooley, V.; **International Space Station – A Unique Place for Research**; IEEE Aerospace Conference, 2003.

[3]. King, M.K., Ross, H.D.; **Overview of NASA Microgravity Combustion Program**; *AIAA Journal*, Vol. 36 N°8, 1998, pp. 1337-1345.

[4]. Mukasyan, A., Lau, C., et alii; **Influence of Gravity on Combustion Synthesis of Advanced Materials**; *AIAA Journal*, Vol. 43, N° 2, February 2005, pp. 225-245.

[5]. Documentation of the Microgravity Advanced Research and Support Centre (MARS), available on-line at www.marscenter.it.

[6]. Zhang, H.; Kamotani, Y. and Ostrach, S.; **Zeolite Crystallization Process Modeling and Comparison with Microgravity Flight Results**; *AIAA Journal of Spacecraft and Rockets*, Vol. 32, N° 1, 1995, pp. 110-116.

[7]. Glicksmann, M.E., Lupulescu, A., Koss, M.B.; **Melting in Microgravity;** *AIAA Journal of Thermophisics and Heat Transfer*, Vol. 17, N° 1, 2003, pp. 69-76.

[8]. Amato, F., Ambrosino, G., Mattei, M. et alii; **Design and Robustness of Gain-Scheduled Control System for Parabolic Flights**; *AIAA Journal of Guidance, Control and Dynamics*, Vol. 19, N° 2, 1996, pp. 430-437.

[9]. Mesland, D., Paris, D., et alii; **Ballistocraft: A Novel Facility for Microgravity Research**; *ESA Bulletin*, N° 82, May 1995, pp. 74-81.

[10]. Mora-Camino, F., Achaibou, A.K.; **Zero-Gravity Atmospheric Fliht by Robust Nonlinear Inverse Dynamics**; *AIAA Journal of Guidance, Control and Dynamics*, Vol. 16, N° 3, 1993, pp. 604-607.

[11]. Amato, F., Ambrosino, G., Garofalo, F. et alii; **A Flight control Systems for Microgravity Experiments**; First IEEE Conference on Control Applications, 1992.

[12]. Kraeger, A.M., Paassen, M.M.; **Micro- and Partial Gravity Atmospheric Flight**; AIAA Congress, Monterey, 2002.

[13]. Accardo, D., Rufino, G. Russo, M. and Moccia, A.; **Aerospace GNC Laboratory at the University of Naples**; Aerotecnica, Missili e Spazio, Vol. 82 N° 1, Jan-Mar 2003, pp. 6-13.

[14]. Accardo, D., Esposito, F., Moccia, A. and Russo, M.; **Performance Evaluation of Different Sensor Configurations for Autonomous Navigation of Unmanned Aerial Vehicles**; 10th St. Petersburg International Conference on Integrated Navigation Systems, St. Petersburg, 2003.

[15]. Hampton, R.D., Knospe, C.R. and Grodsinsky, C.M.; **Microgravity Isolation System Design: a Modern Control Analysis Framework**; *AIAA Journal of Spacecraft and Rockets*, Vol. 33, N° 1, 1996, pp. 110-119.

[16]. Grodsinsky, C.M. and Whorton, M.S.; **Survey of Active Vibration Isolation Systems for Microgravity applications**; *AIAA Journal of Spacecraft and Rockets*, Vol. 37, N° 5, 200, pp. 586-596.

[17]. Whorton, M.; **Robust Control for Microgravity Vibration Isolation**; *AIAA Journal of Spacecraft and Rockets*, Vol. 42, N° 1, 2005, pp. 152-160.

[18]. Hakimzadeh, R., Hrovat, K. et alii; **Summary Report of Mission Acceleration Measurements for STS-78**; NASA TM 107401, Jan. 1997.

[19]. Rice, J.E., Fox, J.C., et alii; **Microgravity Acceleration Measurement System for the International Space Station**; IEEE Instrumentation and Measurement Technology Conference, 1999.

[20]. DeLombard, R., Nelson, E.S. and Jules, K.; **Quasi-Steady Acceleration Direction Indicator in Three Dimensions**; NASA/TM-2000-209931, May 2000.

[21]. Newman, D.J., Amir, A.R., Beck, S.M.; **Astronaut-Induced Disturbances to the Microgravity Environment of the Mir Space Station**; *AIAA Journal of Spacecraft and Rockets*, Vol. 38, N° 4, 2001, pp.578-583.

[22]. Savino, R., Paterna, D. and Nota, F.; **Linear and Pendular Acceleration Effects in Fluid Dynamic Experiments under Low Gravity**; *AIAA Journal of Spacecraft and Rockets*, Vol. 41, N° 6, 2004, pp. 964-972.

[23]. Savino, R., Lappa, M.; **Assessment of Thermovibrational Theory: Application to *G*-Jitter on the Space Station**; *AIAA Journal of Spacecraft and Rockets*, Vol. 40, N° 2, 2003, pp. 201-210.

[24]. Monti, R., Savino, R.; **Microgravity Experiment Acceleration Tolerability on Space Orbiting Laboratories**; *AIAA Journal of Spacecraft and Rockets*, Vol. 33, N° 5, 1996, pp.707-716.

[25]. Bahr, D.E, Schultz, R.D.; **Acceleration Forces Aboard NASA KC-135 Aircraft During Microgravity Maneuvers**; *AIAA Journal of Aircraft*, Vol. 26 N° 7, 1989, pp.687-688.

[26]. Pletser, V.; **Microgravity Research During Aircraft Parabolic Flights: the 20 ESA Campaigns**; *ESA Bulletin*, N° 82, May 1995, pp. 57-68.

[27]. Pastena, M., Didonato, M.P., et alii; **PRORA USV1: the 1st Italian Experimental Vehicle to the Aerospace Plane**; 13th AIAA/CIRA International Space Planes and Hypersonic System and Technology Conference, Capua 2005.

[28]. Crisconio, M.; **PRORA-USV FTB_1 System Specification**, CIRA-CF-04-0551, 2004.

[29]. Russo, M.; **Flyability Analysis for the version VF0.0 of the Nominal Aerostructural Dataset of the FTB_1 Vehicle**; CIRA-CF-05-0110, 2005.

[30]. Corraro, F., Filippone, E., Russo, M. et alii; **Flight Dynamic Characterisation of the USV Flying Test Bed Vehicle**; 13th AIAA/CIRA International Space Planes and Hypersonic System and Technology Conference, Capua 2005.

[31]. Filippone, E.; **PRORA-USV - Reference Trajectory Analysis and Optimisation**; CIRA-CF-05-0216, 2005.

[32]. Etkin, B., and Reid, L.D.; ***Dynamics of Flight: Stability and Control***; 3rd ed., John Wiley and Sons, Inc, New York, 1996.

[33]. Lutze, F.H., Durham, W.C., et alii; **Unified development of lateral-directional departure criteria**; *AIAA Journal of Guidance, Control, and Dynamics*, Vol.19, No.2 1996, pp. 489-493.

[34]. Lee, H.P., Chang, M., et alii; **Flight Dynamics and Stability and Control Characteristics of the X-33 Vehicle**; AIAA Paper 98-4410, 1998.

[35]. Ashwani, C., Nguyen, V., et alii; **Dynamics and Stability and Control Characteristics of the X-37**; AIAA Paper 2001-4383, 2001.

[36]. McLean, D., *Automatic Flight Control Systems*, Prentice Hall, NJ, 1990.

[37]. Wallner, E.M., and Well, K.H.; **Nonlinear Adaptive Flight Control for the X-38 Vehicle**; Proceedings of the 18th International Symposium on Space Flight Dynamics, Munich, Germany, 2004.

[38]. **Flying Qualities of Piloted Aircraft**; MIL-HDBK 1797, US Dept. of Defence Handbook, Dec 1997.

[39]. Russo, M; **PRORA-USV – Monte Carlo Analysis for the FTB_1 Vehicle – Splashdown Results**; CIRA Internal Memo, 2005.

[40]. Ninomiya, T., Suzuki, H. et alii; **Evaluation of Guidance and Control System of High Speed Flight Demonstrator Phase II**; 13th AIAA/CIRA International Space Planes and Hypersonic System and Technology Conference, Capua 2005.

[41]. Starnone, D., Pastena, M., et alii; **Dropped Transonic Flight Test of the USV Program: Trajectory Optimisation and Monte Carlo Analysis**; 55th International Astronautical Congress 2004, Vancouver, Canada.

[42]. Desai, M.P., Braun, R.D.; **Six Degree-of-Freedom Entry Dispersion Analysis for the METEOR Recovery Module**; AIAA Paper 96-0903, 1996.

[43]. Cuciniello, G.; **FTB1 GN&C Detailed Design Document (GCLA1)**; CIRA-CF-05-0387, 2005.

[44]. Nebula, F.; **FTB1 GN&C Prototype Test Facility Description Document**; CIRA Internal Report, in Emission.

[45]. Russo, M.; **Atmospheric and Environmental Disturbances Models for the Flight Mechanics Activities**; CIRA-CF-05-0772, 2005.

[46]. Zhou, K.; *Essential of Robust Control*; Prentice Hall, 1997.

[47]. Russo, M.; **Programma USV – Piano tecnologico: Sviluppo di un Sistema GN&C Avanzato**; CIRA-SOW-04-257, 2004.

[48]. Bodson, M.; **Evaluation of Optimization Methods for Control Allocation**; *AIAA Journal of Guidance, Control and Dynamics*, Vol. 25 N°. 4, 2002, pp. 703-711.

[49]. Russo, M.; **PRORA-USV - Parametric aero-Structural models for the Flight Mechanics Activities**, CIRA-CF-04-0590, 2004.

[50]. Russo, M.; **PRORA-USV – Dynamic Non-Linear and Linear Analytical Models for flight mechanics activities**; CIRA-CF-04-0591, 2004.

[51]. Maine R.R & Iliff, K.W.; **Application Of Parameter Estimation To Aircraft Stability And Control: The Output-Error Approach**; NASA-RP-1168, 1986.

[52]. Stevens, B.L. & Lewis; F.L.; *Aircraft Control and Simulation*; John Wiley & Sons, 1992.